



36th Annual VFS Student Design Competition

Extreme Altitude Mountain Rescue Vehicle

Sponsored by Airbus Helicopters



*Alfred Gessow Rotorcraft Center
Department of Aerospace Engineering
University of Maryland
College Park, MD 20742 U.S.A.*



Alfred Gessow Rotorcraft Center
Department of Aerospace Engineering
University of Maryland
College Park, MD 20742 U.S.A.

Seyhan Gul
Graduate Student (Team Captain)
sgul@umd.edu

Ravi Lumba
Graduate Student
rlumba@umd.edu

Abhishek Shastry
Graduate Student
shastry@umd.edu

Mrinalgouda Patil
Graduate Student
mpatil@umd.edu

Shashank Maurya
Graduate Student
skmaurya@umd.edu

Amy Morin
Graduate Student
amorin1@umd.edu

Nishant Nemani
Graduate Student
nnemani@umd.edu

Dr. Anubhav Datta
Faculty Advisor
datta@umd.edu

Dr. Vengalattore Nagaraj
Faculty Advisor
vnagaraj@umd.edu

Dr. Inderjit Chopra
Faculty Advisor
chopra@umd.edu

The students listed above will receive credit for the course ENAE634: Helicopter Design.



Alfred Gessow Rotorcraft Center
Department of Aerospace Engineering
University of Maryland
College Park, MD 20742 U.S.A.

To Vertical Flight Society:

The members of the University of Maryland Graduate Student Design Team hereby grant VFS full permission to distribute the enclosed Executive Summary and Final Proposal for the 36th Annual Design Competition as they see fit.

The UMD Graduate Design Team

ACKNOWLEDGEMENTS

The design team wishes to acknowledge the following people for their invaluable discussion, guidance, and support throughout the course of this project.

Industry Professionals, High Altitude Mountain Rescuers, Helicopter Rescue Units

Didier Delsalle – Experimental Test Pilot, Airbus Helicopters, Marignane, France; only pilot to land on Mount Everest, world record set on May 14th, 2005

Samuel Summermatter – Search and Rescue Pilot at Air Zermatt, Switzerland; only rescue service operating on the Matterhorn

Baltimore County Police Aviation Unit

Maryland State Police Aviation Command - Frederick Section

John K. Tritschler – Director of Research, U.S. Naval Test Pilot School (USNTPS)

Christian Polyak, PMP – Lieutenant Commander, USCG Aviation Logistics Center

Charley Kilmain – Manager, Mechanical Systems - H1 Program, Bell

Jillian Alfred-Terry – IPT Supervisor, Handling Qualities, Bell

Dr. Ashish Bagai – Principal, buGi Aero, LLC

Carlos de Lima – HyperWorks Solver Task Force Manager

University of Maryland Faculty

Dr. Roberto Celi – Professor, Department of Aerospace Engineering, University of Maryland, College Park

Dr. Anya Jones – Associate Professor, Department of Aerospace Engineering, University of Maryland, College Park

Dr. William Fourney – Keystone Professor, Professor Emeritus, Department of Mechanical Engineering, Department of Aerospace Engineering, University of Maryland, College Park

Alfred Gessow Rotorcraft Center Graduate Students

Daniel Escobar

Dylan Jude

Cheng Chi

James Sutherland-Foggio

Brandyn Phillips

Katie Krohmaly

Contents

Acknowledgements	4
List of Figures	v
List of Tables	viii
1 Introduction	1
2 Concept of Operations	4
3 Configuration Selection	6
3.1 Voice of the Customer	7
3.1.1 Design Drivers	7
3.1.2 Analytical Hierarchy Process (AHP)	8
3.2 Configurations Considered	9
3.3 Pugh Matrix	12
4 Preliminary Vehicle Sizing	13
4.1 Description of Algorithm	14
4.2 Mission Approach	15
4.3 Design Drivers	16
4.4 Blade Loading and Disk Loading	16
4.5 Trade Studies	16
4.5.1 Number of Blades	17
4.5.2 Aspect Ratio	19
4.5.3 Tip Speed	20
4.5.4 Cruise Speed	21
4.6 Vehicle Specifications	21
5 Blade Aerodynamic Design	22
5.1 Design Goals	22
5.2 Design Methodology	23
5.3 Airfoil Selection	24
5.4 Blade Tip Design	26
5.5 Trade-Study on Blade Geometry	27

5.6	Final Blade Design	27
6	Hub Design	29
6.1	Hub Selection	29
6.2	Hub Design	30
6.2.1	Flexbeam	31
6.2.2	Torque Tube	31
6.2.3	Elastomeric Lag Damper	32
6.2.4	Pitch Horn and Pitch Link	32
6.3	Swashplate Design	32
7	Blade Structural Design	34
7.1	Structural Design	34
7.2	Internal Blade Structure	35
7.3	Blade Manufacturing	36
7.4	Blade Sectional Properties	36
7.5	Aeroelastic Stability Analysis	38
7.6	Ground and Air Resonance	38
7.7	Stress Assessment	40
8	Tail Rotor	42
8.1	Sizing	42
8.1.1	Diameter	42
8.1.2	Number of Blades	43
8.1.3	Solidity	43
8.1.4	Tip Speed	44
8.1.5	Location, Configuration, and Direction of Rotation	44
8.2	Aerodynamic Design	45
8.2.1	Airfoil Selection	45
8.2.2	Blade Geometry	46
8.3	Structural Design	47
8.3.1	Hub Design	47
8.3.2	Blade Design	48
9	Empennage Design	48
9.1	Vertical Tail	48
9.2	Horizontal Tail	50
10	Flight Mechanics and Controls	52
10.1	Flight Dynamics	53
10.2	Vehicle Control	53
10.3	Control System Design	53
10.4	Stability Derivatives	55
10.5	Gust Rejection	57
10.6	Effect of Underslung Load	57

11	Transmission Design	58
11.1	Drive System Configuration	58
11.1.1	Weight Minimization	58
11.1.2	Choice of configuration	60
11.2	Design Methodology	60
11.3	Gearbox setup	60
11.4	Notable Features of the Drive System	60
11.5	Housing	61
11.6	Tail Rotor Transmission	62
11.7	Oil System	62
11.8	Shaft Sizing	63
11.9	Weight Estimation	64
11.10	Load Paths	64
12	Powerplant System	64
12.1	Turboshaft Engine	65
12.2	Diesel Engine	66
12.3	Engine Selection	66
12.4	Tail Rotor Power	66
12.4.1	Weight Calculations	67
12.4.2	Performance Analysis	68
13	Airframe and Landing Gear Design	68
13.1	Airframe Design	68
13.2	Windshield	70
13.3	Landing Gear Design	70
13.3.1	Crashworthiness	71
14	Avionics and Search & Rescue Equipment	72
14.1	Automatic Flight Control System	72
14.2	Search Equipment and Hoist System	73
14.3	Deicing and Anti-Icing Systems	74
14.4	Weather Radar	75
14.5	Air Conditioning System	75
14.6	Communications	75
14.7	Navigation	75
14.8	Radar Altimeter	75
14.9	IFR Requirements	76
15	Health and Usage Monitoring System	76
15.1	Main rotor	76
15.2	Engine	80
15.3	Drive System	80
15.4	Structure	80
15.5	Advantages	80

16 Weight Breakdown and C.G. Analysis	81
16.1 Weight Breakdown	81
16.2 C.G. Analysis	82
17 Acoustics	82
18 Vehicle Performance	83
18.1 Drag Estimation	83
18.2 Hover Performance	84
18.3 Forward Flight Performance	85
18.4 Range and Endurance	87
18.5 Rotor Capability	88
18.6 Autorotation Performance	89
19 Life-Cycle Cost Analysis	91
19.1 Purchase Price	91
19.2 Maintenance Cost	91
19.3 Direct Operating Cost	92
20 High Altitude Remarks	92
20.1 Vehicle Design	92
20.1.1 Sizing	92
20.1.2 Tail Rotor Design	92
20.2 Rotor Aerodynamics	93
20.3 Cabin Pressurization	93
20.3.1 Solution Concepts	94
21 Multi-Mission Capabilities	95
21.1 Disaster Relief in Severe Weather	95
21.2 Aerial Fire-fighting	97
21.3 Rapid Air Medical Transport	97
21.4 Off-shore Oil-rigs and Wind Farms	98
21.5 Maritime High-Seas Rescue	98
21.6 Geophysical Surveys and High Altitude Surveillance	99
22 Summary	99

List of Figures

1.1	<i>Caladrius</i> performing a rescue operation	1
1.2	UMD Graduate Design Team members with Didier Delsalle and Samuel Summermatter. Left to right in the photograph on the left (and right to left in the photograph on the right): Ravi Lumba, Amy Morin, Didier Delsalle/Samuel Summermatter, Seyhan Gul	2
2.1	Route followed by Didier Delsalle for the summit	5
3.1	Non-dimensionalized weights and ranking of configuration selection drivers	9
3.2	Configurations considered	11
4.1	Mission profile	13
4.2	Flowchart for the vehicle sizing procedure	14
4.3	Trade studies with number of blades for $C_T/\sigma = 0.12$	17
4.4	Carpet plot for design GTOW vs. DL for variations in N_b and AR	18
4.5	Trade studies with aspect ratio	19
4.6	Trade studies with tip speed	20
4.7	RPM reduction ratio vs. tip speed	20
4.8	Altitude vs. torque	21
5.1	Schematic outline of the process for blade aerodynamic design	23
5.2	Reynold's and Mach number on rotor disk	24
5.3	Maximum C_l/C_d of different airfoils	25
5.4	$C_{l_{max}}$ of different airfoils	26
5.5	Drag polar of different airfoils	26
5.6	Tip sweep to maintain a maximum normal mach number on leading edge of 0.83	26
5.7	High Blade vortex interaction in the absence of anhedral tip	27
5.8	Anhedral tip reduces Blade Vortex interaction in hover	27
5.9	Pareto plot for main rotor blade	28
5.10	Effect of main rotor aerodynamic design on vehicle sizing	28
5.11	Geometry of <i>Caladrius's</i> blade	28
5.12	Stall limit of <i>Caladrius's</i> rotor in vertical gusts at 8870 m	29
6.1	Main rotor hub components	31
6.2	Flexbeam	31
6.3	Swashplate assembly	33
6.4	Cross-sectional view of the swashplate	33

6.5	Original swashplate	33
6.6	Refined swashplate	33
7.1	Primary sections of the main rotor	34
7.2	Internal structure of the blade	35
7.3	Main rotor sectional properties	37
7.4	Fan plot showing main rotor frequencies as a function of rotor speed	37
7.5	Divergence and flutter analysis	38
7.6	Stability analysis of ground resonance for <i>Caladrius</i>	39
7.7	Damping ratio of the modes in ground and air resonance	39
7.8	Strain analysis for main rotor blade using X3D	40
8.1	Ratio of tail rotor power to main rotor power (%) vs. blade diameter	43
8.2	Aspect ratio at different C_T/σ	44
8.3	Tail rotor power variation with tip speed at hover	44
8.4	Tail rotor vertical positioning	45
8.5	Tail rotor airfoil selection	45
8.6	Power required by tail rotor as a function of twist	46
8.7	Angle of attack of different tail rotor blade sections at 40 knots steady side wind	46
8.8	Tail rotor hub components	47
8.9	Fan plot showing tail rotor frequencies vs. rotor speed	48
9.1	Thrust and power sharing between anti-torque devices vs cruise speed	50
9.2	Horizontal tail positioning	51
9.3	Effect of horizontal tail on dynamic stability	51
9.4	Main rotor wake for $\mu = 0.4$, $C_T/\sigma = 0.073$ and $\alpha_s = 5.1^\circ$	52
10.1	Generic model following concept	54
10.2	Model following control law implementation: Pitch attitude channel	54
10.3	Transfer functions for command model and corresponding handling qualities	55
10.4	Stability roots with feedback on and off	56
10.5	Body rates response to step lateral wind	57
10.6	Vehicle response to cosine gust from 45 deg azimuth in hover	57
12.1	Turboshaft engine efficiency and weight trends	65
12.2	PT6C-67A engine	66
12.3	Powerplant system comparison	68
13.1	Airframe stress analysis results (all the stresses are in units of Pascals)	69
13.2	Stress analysis of tail boom (all the stresses are in units of Pascals)	69
13.3	Bird strike impact on windshield and bubble window	70
13.4	Comparison of elliptic and circular cross tubes for landing gear	71
14.1	<i>Caladrius's</i> Glass Cockpit	73
14.2	Some of the search equipment	73
14.3	Recco detector for avalanche	74
14.4	Honeywell weather radar system	75

15.1 Health and Usage Monitoring System flowchart	80
16.1 Longitudinal C.G. with respect to hub and weight change with mission time . . .	82
17.1 Noise distribution(SPL in dB) 150m below the vehicle in hover	82
17.2 Noise distribution(SPL in dB) 150m below the vehicle in cruise	82
18.1 CFD results using Altair Virtual Wind Tunnel	83
18.2 Variation of HOGE power required at design gross take-off weight (3500 kg) and power available with altitude	84
18.3 Hover performance charts	85
18.4 Power required vs airspeed for design GTOW (3500 kg) at 3780 m, ISA + 20° .	85
18.5 Power required vs. airspeed for different altitudes, ISA + 20°	86
18.6 V_{BR} , V_{BE} , and V_{MAX} with altitude, ISA + 20°	86
18.7 Rate of climb vs. airspeed for different altitudes, ISA+ 20°	87
18.8 Maximum rate of climb vs. altitude	87
18.9 Payload vs. Endurance at hover and cruise	87
18.10 Payload vs. Range diagrams	88
18.11 Payload vs. Range for H145 and Caladrius (4500 kg) at sea level, ISA	89
18.12 Comparison of autorotative index for various helicopters	89
20.1 Hover power with altitude	93
20.2 Cruise power with altitude	93
20.3 Mountain High EDS	94
21.1 Mission profile for disaster relief missions	95
21.2 Mission profile for fire-fighting missions	97
21.3 Mission profile for medical transportation at high altitude locations	97
21.4 Mission profile for off-shore transprtation	98
21.5 Mission profile for high-seas rescue	98

List of Tables

1.1	Overview of <i>Caladrius</i>	3
3.1	AHP matrix	9
3.2	Pugh matrix	12
4.1	Comparison of vehicles for refueling and no-refueling cases	15
4.2	Comparison of two configurations designed with different aspect ratios ($N_b = 5$, $V_{tip} = 231.6$ m/s (760 ft/s), $C_T/\sigma = 0.12$)	19
4.3	Summary of vehicle specifications	22
5.1	List of selected airfoils	25
6.1	Hub selection matrix	30
7.1	First six blade frequencies at hover and cruise rotor speeds	37
7.2	Damping requirements for different terrains	39
8.1	Maximum steady side wind in hover to avoid VRS	43
8.2	Tail rotor properties	45
8.3	First four blade frequencies at hover and cruise rotor speeds	48
9.1	Vertical tail properties	49
9.2	Horizontal tail location comparison	50
9.3	Horizontal tail area for the three cases	51
9.4	Horizontal tail properties	51
10.1	Range of control angles	53
10.2	Gains for stabilization loop	55
10.3	Key stability derivatives in hover (leg 2) and cruise (leg 1)	56
11.1	Reduction ratios for transmission system	60
11.2	Design parameters for the first stage bevel gears	61
11.3	Design parameters for second stage planetary gear system	62
11.4	Design parameters for the tail rotor drive system	63
11.5	Sizes of transmission shafts	63
11.6	Drive system weight	64
13.1	Sizing results for landing gear configurations	70

List of Tables

14.1 Avionics list	77
16.1 Weight breakdown	81
18.1 Component breakdown of flat plate area	83
18.2 Performance summary and comparisons	90
20.1 Comparison of vehicles for high and low altitude cases	92
20.2 Comparison of tail rotor design for high altitude and low altitude missions . . .	93

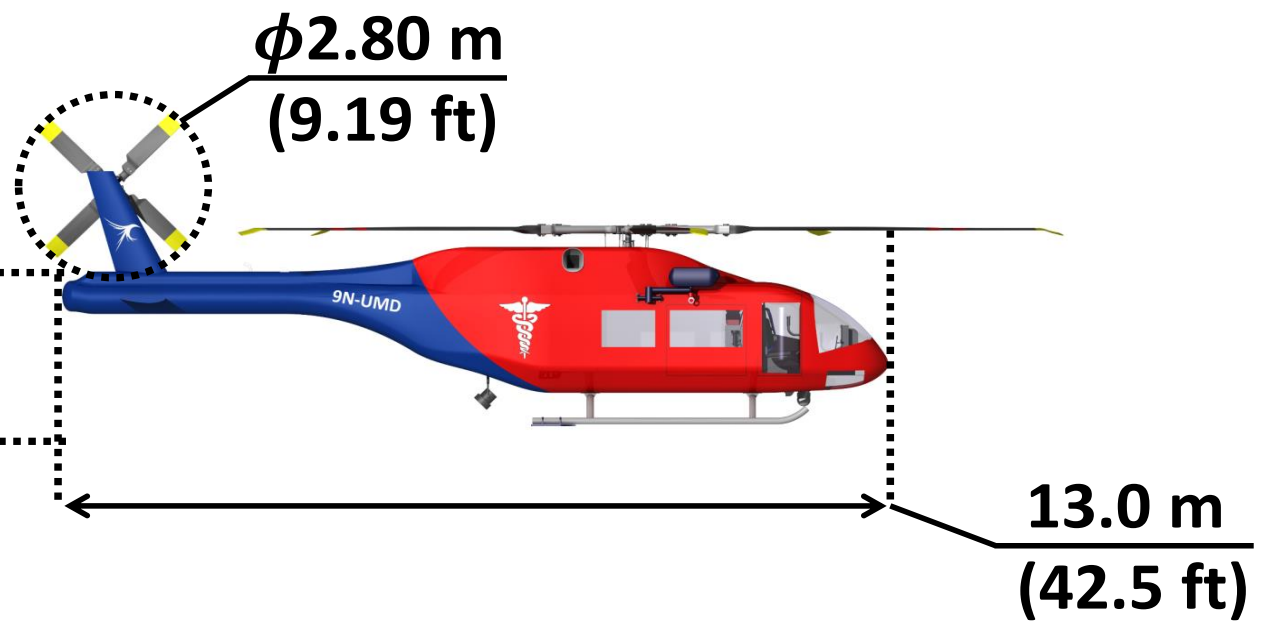
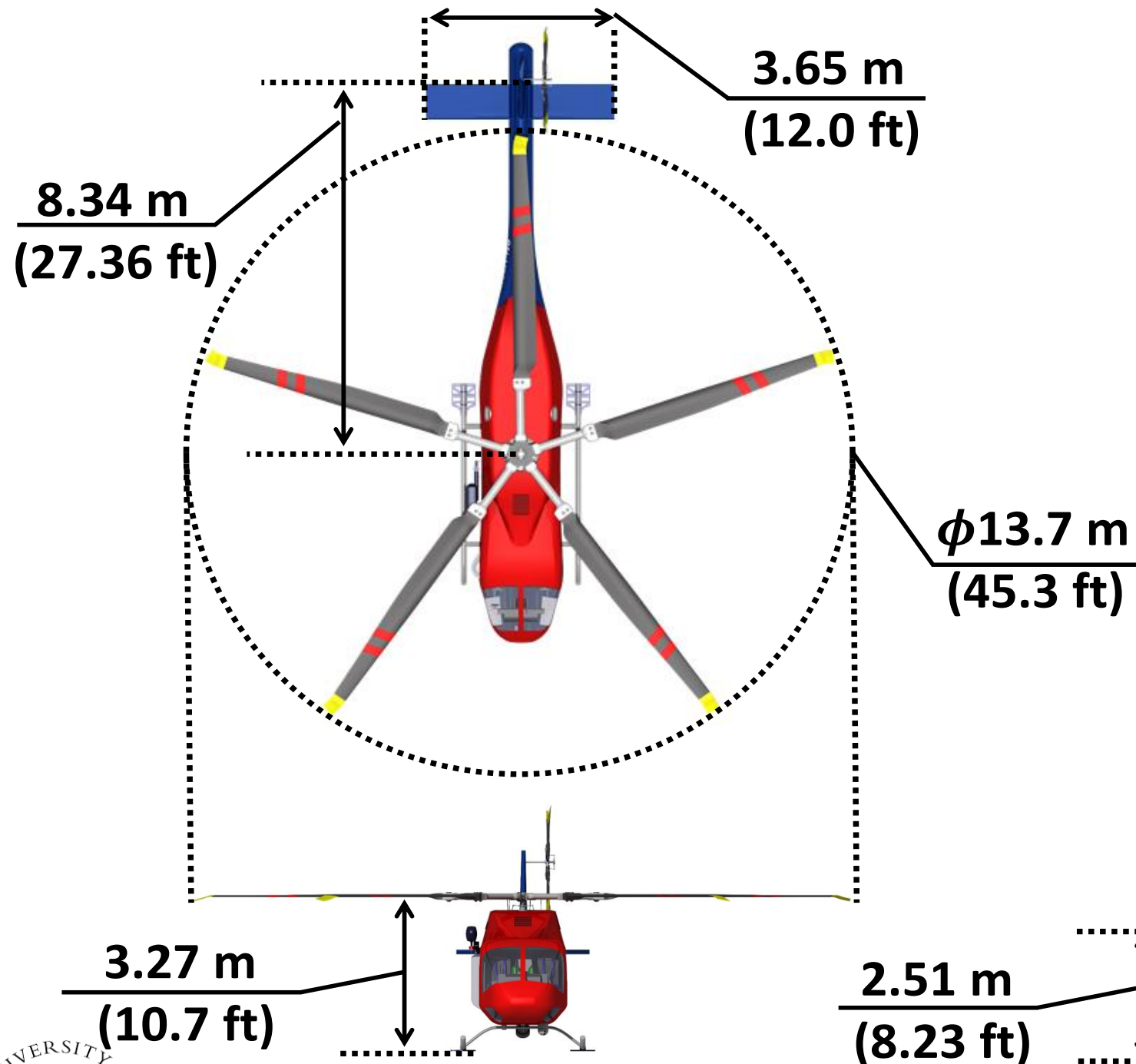
Caladrius RFP Requirements and Compliance

RFP Requirement	Solution	Chapter
The rotorcraft should be able to hover at 8870 m (29100 ft) for 30 minutes.	<i>Caladrius</i> was sized for 30 minutes extreme altitude hover.	4
The rotorcraft should complete the specified mission in less than three hours.	<i>Caladrius</i> was designed for a high cruise speed of 296 km/h (160 knots) and can complete the mission in 175 minutes.	4.5.4, 5, 8
The rotorcraft must include a hoist system rated for a 300 kg (661 lb) load.	A translating drum type hoist was included in <i>Caladrius's</i> design.	14.2
The rotorcraft must be well-controllable in any foreseeable flight condition.	<i>Caladrius's</i> flight control system and rotors were designed for extreme flight conditions.	5, 8, 10
The control system must be capable of maintaining heading in hover with wind from any azimuth up to 74 km/h (40 knots).	<i>Caladrius's</i> flight control system and rotors were designed for extreme wind and gust conditions that are observed at Mount Everest.	5, 8, 10
The rotorcraft must be configured with an avionics suit that meets minimum FAA requirements for single pilot day and night IFR operations and all navigation and communication means deemed relevant to safely perform the mission. Appropriate weight allocation should be made for all components.	Necessary avionics and indicators with their corresponding power and weight requirements were included in <i>Caladrius's</i> design. In addition, the flight control system is designed taking into consideration CS 29 IFR requirements.	14
A cruise speed above 259 km/h (140 knots) for leg 1 should be considered.	<i>Caladrius</i> was designed for a high cruise speed of 296 km/h (160 knots).	4.5.4, 5, 8

Documentation Requirements and Compliance

Documentation Requirement	Chapter
Trade studies for competing vehicle configurations	3
Rotating system optimization studies	5, 6, 7, 8
Engine optimization studies based on existing engine technologies	12
Performance analysis	18
Weight breakdown	16.1
Center of gravity analysis throughout the mission	16.2
Transmission architecture	11
Technological studies for the key components	5 - 13
Cost considerations	19
Additional Graduate Team Tasks:	
Stress assessment of rotors	7.7
Stress assessment of major airframe components	13
Aeroelastic stability boundaries	7.5, 7.6
Handling qualities assessment covering equilibrium, static and dynamic stability	8, 9, 10
Concepts to improve flight under degraded visual conditions and in known icing conditions	14

Three View



1 Introduction

Increased ease of access to information, advancements in material science, engineering, and medicine all helped outdoor sports become more widespread and popular than before. This occurred to such a level that a new category called “extreme sports” emerged in the 1990s [1]. Mountain biking, wind surfing, snowboarding, extreme skiing, and mountain climbing are only a few of many such extreme sports. As the number of people practicing outdoor sports increased, injuries and fatalities also rose. This made the effective means of search and rescue crucial. Rotorcraft are the best suited vehicle to perform such rescue operations because of the mountainous, inaccessible terrain. Today, rotorcraft carry out rescues all around the world; however, there are a few exceptions such as inaccessible and high altitude locations. One of the highest profile locations where rotorcraft cannot yet operate is Mount Everest which has a summit altitude of 8848 m (29029 ft).

Mount Everest, located in the Himalayas, is the highest mountain on Earth. It attracts many climbers, some of them highly experienced mountaineers. Mount Everest presents significant dangers such as altitude sickness, cold weather, high winds, as well as significant hazards from avalanches and the Khumbu Icefall. Due to fast moving jet streams, Everest is often considered the windiest place on Earth. The Himalayan Database reports that there have been more than 8000 summits to Everest [2]. Nearly 300 people have died, many of whose bodies remain on the mountain. The major causes of deaths were from avalanches, falls, altitude sickness, and cold weather exposure. In addition, recent fatalities on Mount Everest were attributed to traffic of mountaineers at the summit [3]. Therefore, designing a rotorcraft to save the lives of numerous climbers is a critical need of the hour.

Most rotorcraft are not specifically designed for search and rescue missions, especially at extreme altitudes; they are often multi-purpose vehicles that can also perform such operations inefficiently. *Caladrius*, named after a snow-white bird from Roman mythology that has healing abilities, is a single main rotor helicopter designed by the University of Maryland Graduate Design Team specifically for rescue missions at an unprecedented altitude. To obtain insights on search and rescue operations, the team contacted and interviewed many experienced pilots: Baltimore County Police Aviation Unit, Maryland State



FIGURE 1.1: *Caladrius* performing a rescue operation

Police Aviation Command, John Tritschler (Director of Research at U.S. Naval Test Pilot School), Christian Polyak (USCG Pilot), Samuel Summermatter (Search and Rescue Pilot at Air Zermatt, Switzerland), and Didier Delsalle (Experimental Test Pilot at Airbus Helicopters, Marignane, France, who is the only pilot to have landed a helicopter on the summit of Mount Everest [4]) (Figure 1.2). The insights provided by these experienced pilots helped focus the engineering efforts on designing a true “Pilot’s Helicopter”. Concept of operations, rotor hub and flight control system designs, avionics suite and search and rescue equipment selection, tail rotor, front windshield, side bubble window, and floor window designs were all influenced by the

valuable inputs obtained from these pilots. High flight safety and low pilot workload emerged as main design objectives.

The challenging mission requirements of 30 minutes hover out of ground effect at high altitude and high cruise speed resulted in a unique aerodynamically optimized main rotor that can provide perfect balance of superior performance between the two flight requirements. Robust bearingless main and tail rotor hub designs eliminate the use of hinges and bearings which make *Caladrius* capable of flying safely in gusty environments. Because of extreme cold weather environment, certification requirements, and experiences by pilots Jean Boulet and Didier Delsalle [4, 5], deicing and anti-icing systems are included for windshield, side and floor windows, engine inlet, main and tail rotor blades, horizontal and vertical tail, and the pitot tube.

Achieving low pilot workload and high level of safety were key factors for the design of *Caladrius*. These led to a twin engine design with a carefully selected avionics package for single pilot day and night IFR operations. The search and rescue equipment included in the design not only decrease the pilot workload, but also significantly increase *Caladrius's* mission effectiveness. The team opted for low downwash which increases hover efficiency, safety on the ground, and convenience of ground operation. *Caladrius* is also free from any aeroelastic instabilities, air/ground resonance; these presented design challenges due to low air density and ensuing high thrust coefficient at high altitude and possible snow landing. Flight control system design focused on decreasing the pilot workload and increasing the safety with model following architecture that increases both gust tolerance and control power. High wind drafts and gusts that are observed on Mount Everest presented another major design challenge. The tail rotor was specially designed to be able to maintain heading at high wind conditions on the mountain while also minimizing its power consumption. A large bubble side window, floor windows, and a front windshield that provide pilots a wide field of view are especially designed to withstand bird strike. Because mountain rescue pilots are trained for the effects of high altitude such as hypoxia, and due to the weight increase, a pressurization system is not included in the design. In general, a light and compact rotorcraft design was developed based on the input from the pilots. An overview of *Caladrius's* features is given in Table 1.1. Modern high-fidelity/in-house analyses were brought to bear on the detailed design.



(a) Meeting with Didier Delsalle, Marignane, France
April 22, 2019



(b) Meeting with Samuel Summermatter, Switzerland
April 23, 2019

FIGURE 1.2: UMD Graduate Design Team members with Didier Delsalle and Samuel Summermatter. Left to right in the photograph on the left (and right to left in the photograph on the right): Ravi Lumba, Amy Morin, Didier Delsalle/Samuel Summermatter, Seyhan Gul

TABLE 1.1: Overview of *Caladrius*

Features	Summary
Main Rotor Carefully Balanced for Extreme Altitude Hover and High Speed Cruise	Airfoils that provide operation without stall even in high updraft conditions that are observed on Mount Everest were selected for this special mission. Twisted and unconventionally tapered blades with anhedral tip provide optimum high altitude hover and high speed cruise performance.
Low Downwash	Low downwash was aimed to increase the hover efficiency, safety on the ground, and convenience of ground operation (overturning forces and moments).
High Cruise Speed	In order to reach the rescuees swiftly, <i>Caladrius</i> was designed for a cruise speed of 296 km/h (160 knots).
Variable Rotor Speed	Compressibility effects due to high cruise speed is avoided at the blade tips by reducing the rotor speed by 12% during cruise.
Twin Turboshaft Engines	Safety was an important criterion for <i>Caladrius's</i> design; hence, twin engine configuration is used for a possible engine failure.
Bearingless Hub Designed for Rescue Operations in Gusty Environments	Robust bearingless hub designed for both main and tail rotors result in low hub drag and low part count. The flexbeam was tailored to achieve the balance between high control authority and high gust tolerance.
Advanced Flight Control System	Model following control system design ensures high gust tolerance and high control power. A four-axis autopilot with different flight modes decreases the pilot workload and increases <i>Caladrius's</i> effectiveness.
Equipment Specific for Search and Rescue	High quality communication equipment, powerful external searchlight, electro-optical system with thermal imaging capability, night vision goggles, weather radar, detector for avalanche, translating drum type rescue hoist that satisfies the requirements, and rescue camera are included in <i>Caladrius's</i> design to reduce crew's workload and increase mission effectiveness.
Double Hook System	The redundant double hook system in addition to the rescue hoist allows high weight external load carrying without any lateral center of gravity shift which is useful for both rescue operations and other missions such as firefighting <i>Caladrius</i> is capable of performing.
Single Pilot Day and Night IFR Capability	A sensitive radar altimeter, required flight indicators, and safety systems required by CS 29 are included in the avionics package for IFR operations. In addition, the flight control system is also designed to satisfy CS 29 IFR requirements.
Tail Rotor Designed for High Wind/Gust Conditions	Tail rotor was designed for low power consumption and high side winds at high altitude. It is free of stall and vortex ring state in extreme environmental conditions and is capable of maintaining heading with wind up to 81 km/h (44 knots) at 8870 m (29100 ft).
Large, Bird Strike Proof Windshield and Windows for High Visibility	In order to provide the pilot a wide field of view that is important especially for the rescue operation, heated large windshield, side bubble window, and floor windows are provided taking into consideration that safety is not compromised in case of a bird strike.



2 Concept of Operations

For many climbers, to stand at the pinnacle of Earth is one of life's most rewarding experiences. The mystique of scaling the legendary peak of Mount Everest is considered the ultimate mountaineering adventure. There are three faces on Everest: the Southwest Face from Nepal, the East Face (Kangshung Face) from Tibet, and the North Face also from Tibet. A set of climbing routes has been established over several decades for expeditions attempting to summit. The two standard climbing routes are: the one approaching from the Southeast in Nepal (known as the "South Col") and the other from the North in Tibet (known as the "North Col"). Other non-standard routes have seen far fewer attempts. The Nepal side is more popular with more than 5,000 summit ascents compared to around 3,000 from the Tibet side [2]. Most of these ascents occur in the months of May and September. These standard routes do not appear to pose insurmountable technical challenges; yet significant dangers lurk, such as altitude sickness, extreme weather, and wind, as well as significant hazards from avalanches and the Khumbu Icefall (an icefall located southwest of the summit). The peak of Mount Everest extends into the upper troposphere and penetrates the stratosphere, which exposes it to the fast and freezing winds of the jet stream. The average wind-speeds on Everest range from 30 to 40 knots during the climbing season. Above 8,000 m (26,246 ft) is known as the "death zone." These inclement weather conditions make climbing Mount Everest an adventurous expedition.

Even though there were many earlier attempts to climb Mount Everest, its first known ascent occurred in 1953 [6]. Thereafter, interest in climbing the peak has exploded. In 1970, an expedition group suffered eight deaths and failed to reach the summit. The death toll increased to fifteen in 1996 due to a high altitude blizzard. Notably, in 2015, an avalanche and an earthquake hit Mount Everest, engulfing the base camp and killing many people. The quakes trapped hundreds of climbers above the Khumbu Icefall, but many were successfully evacuated by helicopter. Bad weather made helicopter evacuation quite difficult. Recently, in May 2019, it has been reported that more than eleven climbers have died due to massive crowding on the mountain. Each of these deaths could have been prevented if medical care was administered within an appropriate time, yet this was not possible with today's technology. Even though high altitude rescues are possible, the current limited capabilities of helicopters presents a high level of risk. At altitudes greater than 6,400 m (21,000 ft), victims must be rescued one at a time, doubling or even tripling the number of flights required. This puts the pilots, the aircraft, and the victims at even greater risk. A solution to all the above problems is *Caladrius*, which provides a low cost, safe, swift, and efficient rescue from the planet's highest point.

The Request for Proposal (RFP) provides a detailed problem statement for the search and rescue mission at the highest altitude of the planet. *Caladrius's* rescue mission adheres to the RFP requirements and an overview of the mission follows. *Caladrius* will be stationed at the Tribhuvan International Airport, in the city of Kathmandu. The base will be staffed 24/7 and each crew will work a 8-hour shift. Upon receiving a call, the crew will be ready to depart immediately within five minutes during the day, and twenty minutes at night. The crew will be made up of three highly-trained personnel, one rescue pilot, one hoist operator, who is also a rescue pilot and crew chief, and an emergency medical services (EMS) specialist. *Caladrius* will fly to a smaller airport (Syangboche Airport) and stop there for a refuel. After 20 minutes of refueling, it will climb to the summit of Mount Everest. The crew will then work to search for the climbers to be rescued, and use the hoist system to rescue them. Loaded with the passengers, *Caladrius* will then return to Syangboche Airport, where the aircraft will refuel again. Finally,



the aircraft will return to Kathmandu, reaching the trauma center in less than three hours from the time the call was received.

The mission involves three important segments, with hover at 8870 m (29100 ft) being the most crucial. The weather and conditions change rapidly around the mountain tops, getting relevant information for mission preparation and possible in-flight adjustments are of high importance, as they can drastically impact aircraft performance and mission success, thereby making the concept of operations (ConOps) a vital aspect of the mission. The ConOps involved in each of the segments of the mission are described below.

Pre-flight: Upon arrival to the base, each crew member will have certain responsibilities. The pilot will check the current weather conditions and identify at least three viable routes to the summit. These routes are updated every three hours if necessary based on the weather conditions. An example route followed by Didier Delsalle is shown in Figure 2.1. The EMS specialist will prepare the medical equipment for a variety of injuries ranging from shock trauma to high altitude sickness. The crew chief will conduct a full inspection of the helicopter and all mission crucial components, such as the hoist, camera turret, and searchlight.

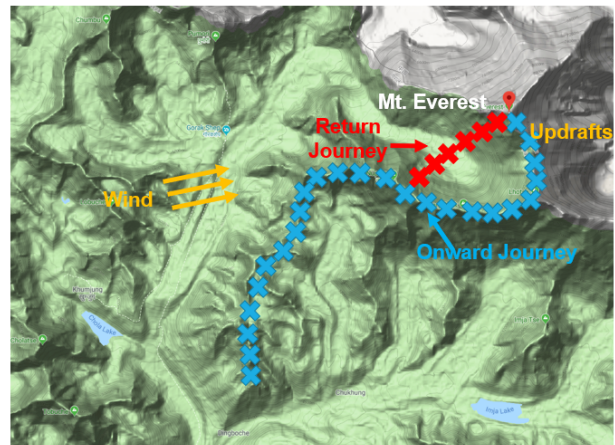


FIGURE 2.1: Route followed by Didier Delsalle for the summit

Upon receiving the call, the pilot and crew chief will roll the helicopter out of the hangar and begin the pre-flight checklist. The EMS specialist will load the relevant medical supplies based on the rescuees' medical condition. From the time of call, the aircraft will be ready to take-off in less than five minutes during the day and 20 minutes at night.

Cruise Segment: The aircraft will first ascend from 1,402 m (4,600 ft) to 3,780 m (12,400 ft) and will carry out steady level cruise at a speed of 160 knots. In emergency medical services, Golden Hour is the one hour period of time following a traumatic injury, during which there is the highest likelihood that prompt medical treatment will prevent death [7]. A higher cruise speed increases the chances of medical staff reaching the rescuees during the Golden Hour, which is crucial for a successful mission. The weather between the two airports can be cloudy with a high risk of icing, so the advanced on board weather radar will aid the pilots in avoiding these clouds. During this segment, the co-pilot will look at the current weather conditions on the mountain using an iPad (present in the cockpit) and perhaps update the route(s) to the summit.

Refueling Stopover: During the 20 minutes for refueling, the pilot and co-pilot (crew chief) revise the route(s) to the summit. Because of the unpredictable and rapidly changing weather on the mountain, there is no guarantee the helicopter will be able to take a predefined route up the mountain. According to Didier Delsalle, getting to the summit could take two or three different attempts, and it is always better to have multiple proposed paths planned as back up plans. To reduce the possibility of altitude sickness, before take-off for ascent to the summit, the crew members will breathe pure oxygen for two minutes. Once the refueling is complete, the aircraft will take-off with only one pilot in the cockpit, and both the co-pilot and the EMS specialist in the cabin.

Search and Rescue segment: The pilot will attempt the primary route to the summit, then all the secondary routes if necessary. After reaching the summit, the crew will work to locate the victim(s). Depending on the time of day and information available, the crew could utilize several features on board the helicopter like the large searchlight, infrared camera turret, and Recco locator for the search process. After locating the rescuees, the pilot will hover close to them for a short period of time to evaluate the local wind conditions and visibility of the area. At this time, the three crew members will come to a decision on whether to conduct the rescue, with the pilot ultimately making the decision.

A dynamic hoisting maneuver will be used to lower the EMS specialist with medical equipment down to the summit. Dynamic hoisting is a procedure where the hoist is raised/lowered while the helicopter has a low forward speed (20-30 knots) to provide aerodynamic damping that stabilizes the slung load. After reaching the ground, the EMS specialist will assess the situation and update the pilot. Next, in order of severity, the specialist will try to stabilize the rescuees, and prepare them for hoisting. In the meantime, the helicopter is conducting traffic circles with clear line of sight to the EMS specialist. Although the helicopter is sized to hover for 30 minutes, conducting traffic circles helps reduce fuel consumption and eliminates having the downwash directly on the rescuees. Once the rescuees are prepared, they are hoisted into the helicopter one by one which can be achieved through one of two techniques: (1) the use of a backboard enclosed in a rescue bag in the case of spinal/head injury, and (2) the use of a harness for minor injuries. In both cases, the EMS specialist ascends with the rescuee. This is useful for stability and comfort of the rescuee. This phase of the operation will not take more than 30 minutes.

Return Segment: With everyone on board, the aircraft descends back to the smaller airport. Any medical operations that is possible will be performed by the EMS specialist on flight and during the stopover. In case of extreme medical condition, the rescuee(s) will be transported to the nearby hospital (The Mountain Medical Institute). Once the aircraft is refueled, it will begin its journey to Kathmandu. The aircraft will either land at the international airport (as per the mission) or at a hospital in Kathmandu for medical treatment of rescuees. Finally, after reaching the base, the crew debriefs the completed mission, performs any post-flight checks and prepares for the next call.

3 Configuration Selection

The RFP requires a rotorcraft “specifically designed to perform emergency medical services up to the highest peaks of the planet”. Therefore, major focus was on designing a vehicle that would perform this key mission while being able to perform other missions as well.

Based on the mission requirements, design drivers for configuration selection have been identified and the Analytical Hierarchy Process (AHP) [8] was used to determine the importance of each driver. In this method, the design drivers were scored against each other and weight factors were obtained as explained in Section 3.1.2 and shown in Table 3.1. Each member of the team individually constructed an AHP matrix, then the mean values for the weights were calculated while taking into consideration that the standard deviation is low.

After the AHP matrix, a Pugh matrix [9] was constructed with the selected configurations. In this matrix, each configuration was given a score for a specific design driver as explained in Section 3.3 and shown in Table 3.2. Multiplying the scores and weights of the design drivers and summing them provided a total value for each configuration. The top three configurations were obtained with this method. The final decision, between these three configurations, was



made after more in-depth deliberation over pros and cons, pilot and industry expert inputs, and detailed analyses.

3.1 Voice of the Customer

3.1.1 Design Drivers

After analyzing the RFP, 14 key design drivers were identified. A list of them is given below:

- **Gust Tolerance (the time required to return to stable equilibrium after a severe gust encounter):** Lifting surfaces and the presence of a tail rotor decreases gust tolerance. The summit of Mount Everest is known particularly for updrafts, downdrafts and high gusts from every direction and these are considered in the configuration selection and design process.
- **Agility in Hover (ability of the rotorcraft to perform quick and precise maneuvers during hover):** Agility in hover is important to have high control authority to position the rotorcraft as required and to keep the slung load stable during the rescue operation, especially in high gust conditions.
- **Hover Efficiency at High Altitude (power consumption in hover):** Hover efficiency at high altitude is crucial for this mission because it has a major impact on the design sizing due to the required long hover duration. Its significance is even higher if an internal combustion engine is used due to the lapse rate (ratio of available power at altitude to that of sea level) at high altitude. High hover efficiency can be achieved with low disk loading and high Figure of Merit.
- **Cruise Performance (maximum cruise speed and the corresponding power consumption):** Although the lapse rate during the cruise phases of the mission (legs 1 and 3) has less impact on the design when compared to leg 2 due to the lower altitudes, low power consumption is still important because of the high flight speeds required to swiftly reach the rescuees and bring them back to safety.
- **Downwash (the hover downwash velocity due to the lifting rotors):** In addition to resulting in low induced power, low downwash velocity is also important for the rescue operation in terms of avalanche, whiteout, and the stability of the rescuees/crew (overturning forces and moments) on the ground under the rotorcraft. Reference [10] states a dynamic pressure greater than 245.15 N/m^2 (5.12 lbf/ft^2) results in a hazardous zone for a 1.83 m (6 ft) civilian crouched over and leaning.
- **Ground Crew Vulnerability (clearance of a person on the ground from any rotating components; especially the tail rotor):** In case of any landing scenario, proximity of the rotating components to the ground is an important source of hazard to ground crew and rescuees. The RFP requires landing at a small airport but possible landing at or near the rescue location has also been considered although the vehicle sizing is performed for 30 minute hover.
- **Agility in Cruise:** Agility in cruise is measured by the maneuverability of the rotorcraft during cruise.



- **Empty Weight to Gross Take-off Weight (GTOW) Ratio:** This ratio is a good index of the lifting capabilities of the rotorcraft and the efficiency of the design. The pilots that the team interviewed stressed on the importance of a light rotorcraft design.
- **Vibrations in Cruise (vibrations transferred to the fuselage by other components such as rotors and wings):** This design driver is included with fatigue life considerations and to ensure that EMS specialist can easily stabilize the condition of the rescues in the fuselage.
- **Technology Maturity:** A configuration with high technology maturity is one that has been in use for long enough that most of its initial faults and inherent problems have been eliminated or reduced by further developments.
- **Life-Cycle Cost:** Life-cycle cost includes development, production, and operation costs. A complex rotorcraft would require more maintenance; hence, mechanical complexity is also considered under this driver. In addition, a low technology maturity requires high development cost.
- **Center of Gravity (C.G.) Range (longitudinal and lateral center of gravity range where the helicopter is stable):** This design driver is considered mostly due to the slung load rescue operation.
- **Compactness (footprint of the rotorcraft when it is hovering):** Compactness is included due to the nature of the operating terrain.
- **Autorotation Capability (rate of descent and controllability of the rotorcraft when one or more engines fail):** Autorotation capability is considered for safety of the crew and the rescues.

3.1.2 Analytical Hierarchy Process (AHP)

Table 3.1 shows the AHP matrix, which was used to determine the weight of each design driver by individually comparing against all other drivers. This method produces weights based on relative importance between design drivers. This is obtained by calculating the average of the team members' scores while making sure the standard deviation is low. Each design driver (horizontal row) was assigned a score against the other design drivers (vertical columns). The scores span from 1/9 (much less important) to 9 (much more important). The results from the AHP are shown in Figure 3.1, which shows the ranking of the design drivers and their corresponding non-dimensionalized weights.

These results show that the most important design driver is hover efficiency because it is expected to have a dramatic effect on the vehicle sizing due to the 30 minute hovering at extreme altitude. The second most important driver is gust tolerance. To be able to effectively extract rescues, this vehicle is expected to perform precise positioning under high gust velocities. Hence, it is important that the rotorcraft is designed accordingly. The third design driver is downwash, which is important for not only low induced power, but also for the safety and stability of the ground crew and rescues. Because the weights of "agility in cruise" and "technological maturity" are much lower than those of the other design drivers, they are not included in the configuration selection process.



TABLE 3.1: AHP matrix

	Hover Efficiency	Cruise Performance	Downwash	Ground Crew Vulnerability	Gust Tolerance	Agility in Hover	Agility in Cruise	Empty Weight to GTOW Ratio	Vibrations in Cruise	Technology Maturity	Life-Cycle Cost	CG Range	Compactness	Autorotation Capability	Normalized Priority
Hover Efficiency	1.00	4.43	2.71	5.86	2.14	3.36	7.29	4.71	4.86	6.71	6.57	4.14	5.29	5.43	0.205
Cruise Performance	0.23	1.00	0.44	3.00	0.28	0.43	4.29	1.36	1.94	4.57	4.43	0.57	2.43	3.00	0.064
Downwash	0.38	2.48	1.00	4.71	0.49	2.29	5.71	3.29	4.00	5.86	5.29	3.14	4.14	4.43	0.125
Ground Crew Vulnerability	0.18	0.35	0.22	1.00	0.21	0.29	3.71	1.14	0.49	3.29	2.71	0.35	1.62	1.30	0.037
Gust Tolerance	0.48	3.72	2.10	4.98	1.00	2.86	6.86	4.14	4.71	6.43	5.86	4.00	5.14	4.71	0.164
Agility in Hover	0.31	2.62	0.56	3.71	0.37	1.00	5.43	2.93	3.29	5.57	4.71	2.86	3.71	3.43	0.102
Agility in Cruise	0.14	0.25	0.18	0.28	0.15	0.19	1.00	0.39	0.26	1.45	0.84	0.27	0.50	0.77	0.018
Empty Weight to GTOW Ratio	0.22	0.93	0.33	1.46	0.25	0.35	3.40	1.00	2.50	4.00	3.29	1.07	2.64	2.46	0.056
Vibrations in Cruise	0.21	0.70	0.26	2.36	0.22	0.34	4.00	0.67	1.00	4.00	3.07	0.48	2.21	2.26	0.048
Technology Maturity	0.15	0.25	0.19	0.40	0.16	0.18	1.79	0.28	0.26	1.00	0.62	0.23	0.49	0.42	0.018
Life-Cycle Cost	0.16	0.24	0.21	0.54	0.18	0.23	3.04	0.33	0.54	2.93	1.00	0.31	1.19	0.38	0.026
CG Range	0.25	2.04	0.33	3.14	0.25	0.37	4.43	2.12	2.14	4.81	3.81	1.00	3.29	2.71	0.071
Compactness	0.21	0.54	0.25	0.93	0.21	0.28	2.71	0.58	0.70	2.62	1.40	0.34	1.00	1.29	0.032
Autorotation Capability	0.19	0.42	0.23	1.07	0.22	0.31	2.65	0.89	0.58	3.00	2.86	0.39	1.17	1.00	0.034

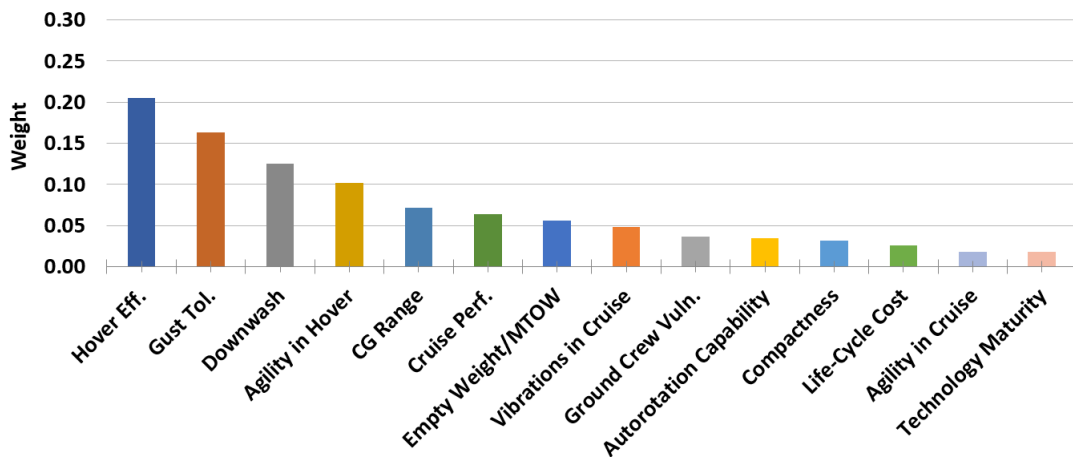


FIGURE 3.1: Non-dimensionalized weights and ranking of configuration selection drivers

3.2 Configurations Considered

Configuration selection was performed by using a Pugh matrix where 16 configurations, some of which are shown in Figure 3.2, were qualitatively evaluated with respect to the previously stated design drivers. Note that all the comparisons between configurations were made at the same disk loading. For example, for a twin rotor aircraft, the area of each rotor is half of that of the main rotor on a single main rotor aircraft.



A brief description for each configuration and some of their advantages and disadvantages with respect to the single main rotor configuration are given below:

- **Single Main Rotor (SMR):** This configuration utilizes a main rotor for lifting and propulsion and a conventional open tail rotor for anti-torque. It is used as the baseline configuration for all comparisons.
- **Single Main Rotor with Fenestron (shrouded tail rotor):** A shroud can decrease the induced power of the tail rotor by up to 30% by restricting the wake contraction, while the disk area is kept constant [11]. However, it comes with a weight penalty, which increases the empty weight of this configuration. In order to take advantage of the shroud, a relatively small tail rotor is required, which would decrease its hover efficiency. In addition, cruise performance is reduced due to flow separation at the leading edge of the shroud in edgewise flight condition [11]. The main advantage is lower ground crew vulnerability because the danger of tail rotor strike is greatly reduced.
- **NOTAR (similar to SMR, but with an anti-torque device that relies on Coandă effect as well as a jet thruster):** This configuration uses a variable pitch fan to generate high volume of low pressure air in the tail boom, some of which is released from Coandă slots. With the help of this flow combined with the main rotor inflow, the tail boom acts as an airfoil, which can provide up to 60% of the anti-torque. The remainder of the anti-torque requirement is covered by a jet thruster at the tip of the tail boom.

This configuration has a similar power consumption to an SMR [12]. The main advantages are low ground crew vulnerability and compactness. A major disadvantage is that a NOTAR would have a lower gust tolerance, which is crucial for this mission, because gust can easily disturb the flow around the tail boom.

- **Coaxial Rotor (two vertically separated counter-rotating rotors for both lift and propulsion):** Two different concepts were considered: closely separated (hingeless) and well separated (articulated) rotors. While closely separated configuration provide higher control authority and result in less hub drag, which constitutes a considerable portion of the total rotorcraft drag, the efficiency in hover is lower and downwash, vibration transmitted to the airframe, and empty weight fraction are higher compared to the separated configuration.

When compared to SMR, both configurations have lower hover efficiency and higher induced flow due to one rotor being in the downwash of the other one and higher empty weight and cost due to the heavy hub and mast structure. On the other hand, they constitute a more compact design and can provide much lower ground crew vulnerability due to the absence of a tail rotor.

- **Inter-Meshing Rotor (similar to coaxial rotor configuration but the rotors are angled sideways):** Compared to SMR, lower hover efficiency, because part of the thrust is lost, and higher induced flow, since the rotors work in each other's downwash, are the main disadvantages of this configuration. In addition, it also has low cruise performance due to hub drag and higher empty weight due to the hub structure. The advantages are higher C.G. travel, less ground crew vulnerability from the absence of a tail rotor, and greater compactness.



- **Twin Rotor (tandem and side-by-side):** These configurations utilize two longitudinally or laterally separated rotors that provide lift, propulsion, and anti-torque. Both overlapping and non-overlapping types were considered.

They provide good gust tolerance and low ground crew vulnerability because there is no tail rotor and high longitudinal or lateral C.G. travel due to the separation of the rotors. However, they have lower cruise performance due to high parasitic drag, high empty weight due to inter-connecting shafts and the supporting structure, high vibrations in cruise, low autorotation capability, low compactness, and high cost. Non-overlapping tandem and side-by-side configurations differ from their overlapping counterparts in terms of higher hover efficiency and lower downwash, since the rotors do not work in the wake of each other in hover, and lower vibrations in cruise but lower cruise performance due to higher parasitic drag, higher empty weight, and lower compactness. Finally, a tandem configuration is considered to be slightly better for this mission than side-by-side since the parasitic drag is expected to be lower even though vibrations in cruise would be higher due to rotor-wake interactions.



FIGURE 3.2: Configurations considered

- **Tiltrotor/Tiltwing/Tilting Ducted Fan (two or more rotors that have the ability to tilt for forward flight during which wings provide lifting and rotors provide propulsion):** Compared to SMR, these configurations all provide greater speed (far more than needed for this sizing mission), higher center of gravity travel, lower vibrations in cruise, and lower ground crew vulnerability. The main disadvantages are low gust tolerance due to wings, high empty weight fraction, and low compactness.
- **Quadcopter (four longitudinally and laterally separated rotors that provide both lift and propulsion):** Although this configuration could be superior in terms of hover efficiency and gust tolerance because there is no tail rotor and they can provide a large C.G. travel, their empty weight and cost are very high, and cruise performance is poor.

- **Lift Compounded and/or Thrust Compounded (SMR or coaxial with wings and/or a pusher propeller):** Three different configurations were considered under this group: lift compounded (SMR with wings), thrust compounded (a coaxial with a pusher propeller), and lift and thrust compounded (an SMR with wings and a pusher propeller). All these configurations have low hover efficiency either due to downwash on the wings, causing blockage effect, or the additional power required for the propeller. In addition, the ones with wings also have low gust tolerance. On the other hand, they have high cruise performance due to wings and/or the pusher propeller and less vibrations in cruise since the rotor is off-loaded.

3.3 Pugh Matrix

Table 3.2 shows the Pugh matrix constructed to rank the configurations based on the selected design drivers. Each configuration was compared against the single main rotor configuration. A grading scale from -4 (much worse) to 4 (much better) with increments of 1 was used. To reiterate, all the qualitative comparisons between the configurations were made by keeping the disk loading same.

TABLE 3.2: Pugh matrix

	Weight	SMR	SMR with Fenestron	NOTAR	Coaxial (Rigid)	Coaxial (Separated)	Tandem (Overlapping)	Tandem (Non-overlapping)	Side-by-Side (Overlapping)	Side-by-Side (Non-overlapping)	Tiltrotor/Tiltwing	Tilting Ducted Fan	Inter-Meshing	Quadcopter	Lift Compounded	Thrust Compounded	Lift and Thrust Compounded
Hover Efficiency	0.205	0	-1	0	-2	-1	0	1	0	1	0	2	-1	1	-1	-2	-2
Gust Tolerance	0.164	0	0	-1	0	0	1	1	1	1	-1	-3	0	1	-1	0	-1
Downwash	0.125	0	0	0	-2	-1	-1	0	-1	0	0	0	-1	0	0	-1	0
CG Range	0.071	0	0	0	1	0	2	2	2	2	2	2	1	4	0	0	0
Agility in Hover	0.102	0	0	0	0	-1	0	0	0	0	0	-1	0	1	-1	-1	-2
Cruise Performance	0.064	0	-1	0	0	-1	-2	-3	-3	-4	1	2	-3	-4	2	1	3
Empty Weight to MTOW Ratio	0.056	0	-1	-1	-2	-1	-2	-4	-2	-4	-4	-4	-1	-4	-2	-3	-4
Vibrations in Cruise	0.048	0	0	0	-1	0	-2	-1	-1	0	1	1	-2	-3	1	2	3
Autorotation Capability	0.034	0	0	0	-3	-2	-2	-1	-2	-1	2	0	-2	-4	1	-2	1
Ground Crew Vulnerability	0.037	0	2	3	3	3	3	3	3	3	3	3	1	2	0	0	-2
Compactness	0.032	0	0	1	1	1	-1	-2	-1	-2	-2	-2	1	-3	0	1	0
Overall Cost	0.026	0	-1	-2	-3	-2	-3	-3	-3	-3	-4	-4	-2	-4	-1	-3	-3
Score	0.000	-0.278	-0.130	-0.788	-0.530	-0.225	-0.021	-0.241	-0.037	-0.124	-0.147	-0.656	-0.135	-0.399	-0.760	-0.783	



The Pugh matrix shows that the highest ranking configurations are SMR, tandem (non-overlapping), and side-by-side (non-overlapping). Although an SMR has slightly lower hover efficiency and gust tolerance due to the tail rotor and lower center of gravity travel compared to the other two configurations, it is superior in terms of access to rugged terrain, cruise performance, empty weight fraction, vibrations in cruise, autorotation capability, smaller footprint due to compactness, and cost. In addition, after further deliberations, it was determined that the Pugh matrix cannot accurately capture the resulting weight and size if a tandem or side-by-side is chosen as the final configuration. The rotorcraft with either one of these configurations is expected to be large and heavy, which is not desirable, as expressed by all pilots during interactions. Hence, it was decided to select single main rotor helicopter as the final configuration.

In summary, 14 design drivers and 16 configurations were qualitatively analyzed and the single main rotor configuration was evaluated as the best choice for this unique mission.

4 Preliminary Vehicle Sizing

Caladrius is designed to be a light weight, gust tolerant, rugged access, search and rescue helicopter, which is capable of performing rescue operations from the highest peak on Earth. It is a twin engine aircraft (discussed in detail in Chapter 12) with low disk loading and remarkably high hover and cruise efficiency.

An in-house sizing code was developed using modified momentum theory to model aerodynamics in hover, forward flight, climb, and descent. While this methodology is fairly general in its applicability, the code modifies a number of standard equations and parameters to provide the flexibility to perform analysis for the mission specified in the RFP. Trade studies have been conducted to examine the merits of varying number of blades (N_b), aspect ratio (AR), tip speed (V_{tip}), and disk loading (DL). A far wider range of design parameters than conventionally used was explored to find the best suited design for such a unique mission. By using the results of these trade studies, a preliminary vehicle design was obtained.

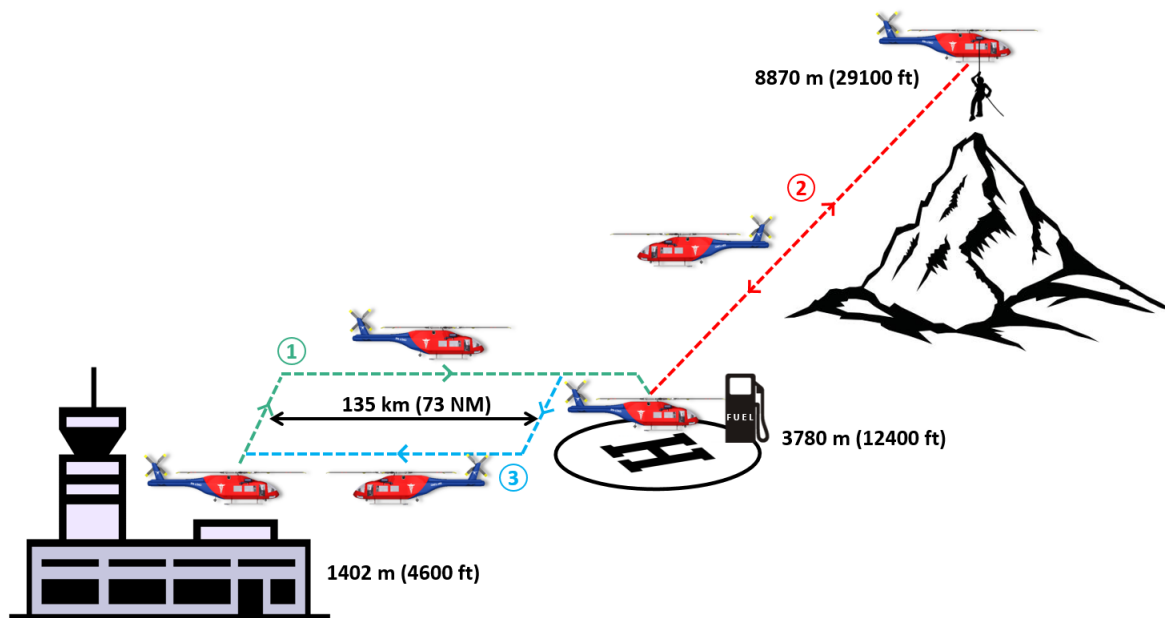


FIGURE 4.1: Mission profile

The mission is comprised of three legs as shown in Figure 4.1. It was determined that Leg 2 would set the sizing, which means that it dictates the vehicle size for the entire mission, because it was the most demanding. Reiterating the mission requirements, the proposed vehicle should be able perform search and rescue operations at the highest point on Earth at an altitude of 8870 m (29100 ft). A time constraint of three hours is imposed for the entire mission, which includes 30 minutes of hover out of ground effect (HOGE) at the summit and a total of 40 minutes of refueling at the stopover locations. Because different segments of the mission are performed at different altitudes, the variation of density and speed of sound with altitude were taken into account for both the aircraft as well as engine. Maximum payload is 575 kg (1268 lb) with 3 crew, 2 passengers, and 150 kg (330.7 lb) EMS equipment and the minimum cruise speed required by the RFP is 259 km/h (140 knots). The helicopter should be designed to provide efficient hover performance, but not at the cost of cruise performance. In order to perform the mission efficiently, emphasis was given to hover efficiency, cruise performance, and minimizing weight. Flying preferences were factored into the design using insights for improvements from two key pilots (Samuel Summermatter and Didier Delsalle) all while keeping cost in consideration.

4.1 Description of Algorithm

The flowchart for the sizing methodology is depicted in Figure 4.2. The sizing code uses an iterative process that begins with the specification of inputs, which includes both mission-specific parameters such as ambient environment, mission profile, required payload, and vehicle-specific information, such as engine performance and rotor geometry.

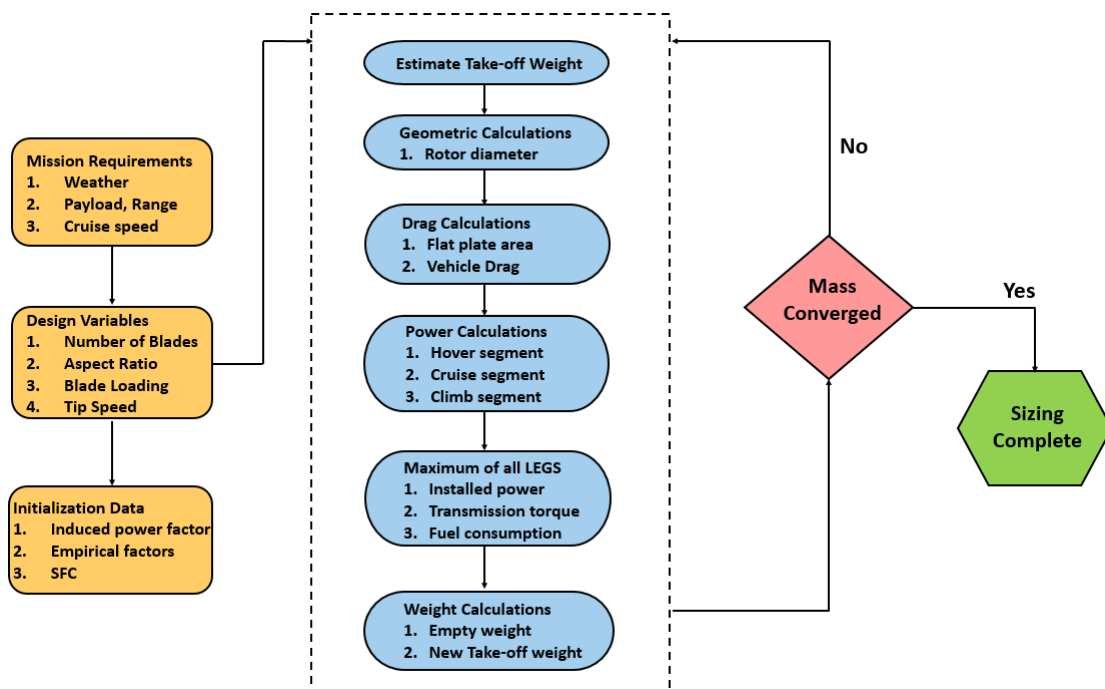


FIGURE 4.2: Flowchart for the vehicle sizing procedure

An initial estimate for the design gross take-off weight (GTOW) for the mission needs to be provided. The next step is a series of performance calculations, which are conducted for each leg separately (since refueling takes place at the end of each leg). These calculations are based on the mission requirements and user inputs (N_b , AR, etc.). The addition of two passengers during the second leg was taken into consideration from the beginning of the 30 min hover segment at



the highest altitude in order to be the most restrictive mission. Even though dynamic hoisting was to be used as a mode of operation during the rescue, the sizing calculations were carried out considering the vehicle to be in hover. These calculations are followed by the component weight calculations using the Aeroflightdynamics Directorate (AFDD00) weight model [13]. If the maximum take-off weight value does not match the initial guess, the calculated empty weight is taken as the updated value and the algorithm runs iteratively until the weight is converged. This entire process is repeated for various combinations of number of blades, aspect ratio, tip speed, and powerplant types (described in detail in Chapter 12). This process allows a direct comparison of various configurations and ultimately, the selection of the best design to meet the mission requirements.

4.2 Mission Approach

The minimum cruise speed of the vehicle in legs 1 and 3 are determined by the total mission time, set by the RFP. The vehicle was designed to complete the mission in 2 hours and 55 minutes so a margin of 5 minutes is included. Because the RFP provides the cruise distance, climb altitude, and hover and refueling times, a minimum average cruise speed of 293 km/h (158 knots) is required to complete the mission when 7.62 m/s (1500 ft/min) is used as the climb speed, which was confirmed by Didier Delsalle as an appropriate speed. With this cruise speed, the time required to reach the rescue location was calculated to be around 70 minutes.

The RFP states that stopovers at the end of legs 1 and 2 are mandatory, but refueling is optional. Hence, a vehicle which has the capability to perform the entire mission without refueling at the first stopover location was also considered to take advantage of reaching the rescuees within the **Golden Hour**. An initial comparison was performed to understand the effects on vehicle sizing and performance with and without refueling. The results are presented in Table 4.2, and were calculated with $N_b = 5$, $AR = 19$, blade loading (C_T/σ) = 0.12, and $V_{tip} = 231.6$ m/s (760 ft/s).

TABLE 4.1: Comparison of vehicles for refueling and no-refueling cases

Parameter	Units	Case 1 (Refueling)	Case 2 (No Refueling)
Design GTOW	kg	3507	3864
	lb	7732	8519
Rotor Diameter	m	13.77	14.45
	ft	45.2	47.43
Installed Power	kW	2503	2646
	HP	3356	3548
Fuel Capacity	lb	232	400
	kg	512	882
Golden Hour		No	Yes

Even though the vehicle sized for no refueling has the capability to reach the rescuees within the golden hour and has a higher fuel tank capacity, it is also heavier; therefore, the team decided the mission with refueling was a more appropriate design. A heavier, less compact and a more costly helicopter (without refueling) would not be a suitable choice for a high altitude rescue mission. Furthermore, Reference [14] states that majority of deaths at the summit occur due to non-traumatic accidents, whereas the golden hour is more applicable for traumatic injuries.



Hence, performing the mission in three separate legs, with refueling at the stopovers, was chosen as the mission approach for the design.

4.3 Design Drivers

The inputs and outputs of the sizing code are a mathematical relationship that provide limited qualitative insight into one aircraft being better or more feasible than another. Restrictions on number of blades, disk loading, and rotor solidity have to be set to acceptable values when performing the sizing analyses. Similarly, because the sizing code does not consider issues such as manufacturability or airfoil stall, such solutions should be filtered out from the outputs.

To arrive at the best design choice, several configurations were considered based on the variation of four critical parameters affecting the main rotor: number of blades, aspect ratio or solidity, disk loading, and hover tip speed. Equation 4.1 provides the relationship between these critical parameters and blade loading.

$$\boxed{\frac{C_T}{\sigma} = \left(\frac{\pi}{\rho}\right) \frac{DL}{N_b} \frac{AR}{V_{tip}^2}} \quad (4.1)$$

4.4 Blade Loading and Disk Loading

Rotor blade loading coefficient is defined as C_T/σ and is a non-dimensional measure of the lift on each blade. Using the McHugh stall boundary [15], the onset of stall for a representative airfoil is defined as $C_T/\sigma = 0.16$ in hover. Since blade loading is a function of density, it is not constant for the entire mission; the maximum blade loading occurs at the lowest density or the highest altitude (leg 2). $C_T/\sigma = 0.12$ was selected for the highest altitude to have sufficient stall margin for maneuvers and control authority during severe gust encounters.

The upper limit for disk loading is set by the downwash velocity because of its impact on the rescues and other nearby climbers during the search and rescue phase of the mission [4]. As mentioned in Chapter 3, a lower downwash will result in lower possibility of causing an avalanche and whiteout. Downwash can also have an important effect on the rescues and crew on the ground in terms of overturning forces and moments. Because of this, a constraint of 24.41 kg/m^2 (5 lb/ft^2) was imposed on the design by using the critical dynamic pressure given in Reference [10]. Even though a low disk loading results in a larger rotor diameter, resulting in a less compact design, low downwash was considered to be vital for this design.

4.5 Trade Studies

The final decisions for sizing of *Caladrius* was made based on an extensive parametric study where different values of number of blades, aspect ratio (defines solidity for a given number of blades) and tip speed were used. In addition, optimum cruise speeds for legs 1 and 3 were chosen based on the sizing of the transmission. Another important design parameter was the choice of the powerplant system. State-of-the-art turboshaft engines and other powerplant options including generators and batteries were considered to achieve low specific fuel consumption and a high power to weight ratio. This study is presented in Chapter 12.



4.5.1 Number of Blades

To understand the effect of number of blades on sizing, disk loading was obtained from Equation 4.2 for different number of blades, while keeping aspect ratio and tip speed constant.

$$DL = \left(\frac{C_T}{\sigma}\right) \left(\frac{\rho}{\pi}\right) \frac{N_b V_{tip}^2}{AR} \quad (4.2)$$

Figure 4.3 shows the effect of number of blades on rotor diameter from Equation 4.2, and then predictions of installed power, engine weight, blade weight, and design GTOW for $AR = 19$ and $V_{tip} = 231.6$ m/s (760 ft/s). An increase in number of blades while keeping thrust per blade area (blade loading) constant means reducing rotor diameter hence blade weight. But it also reduces disk loading for the same thrust, hence increasing power. The increase in power results in increases in fuel, engine, and transmission weights. These results are shown in Figure 4.3.

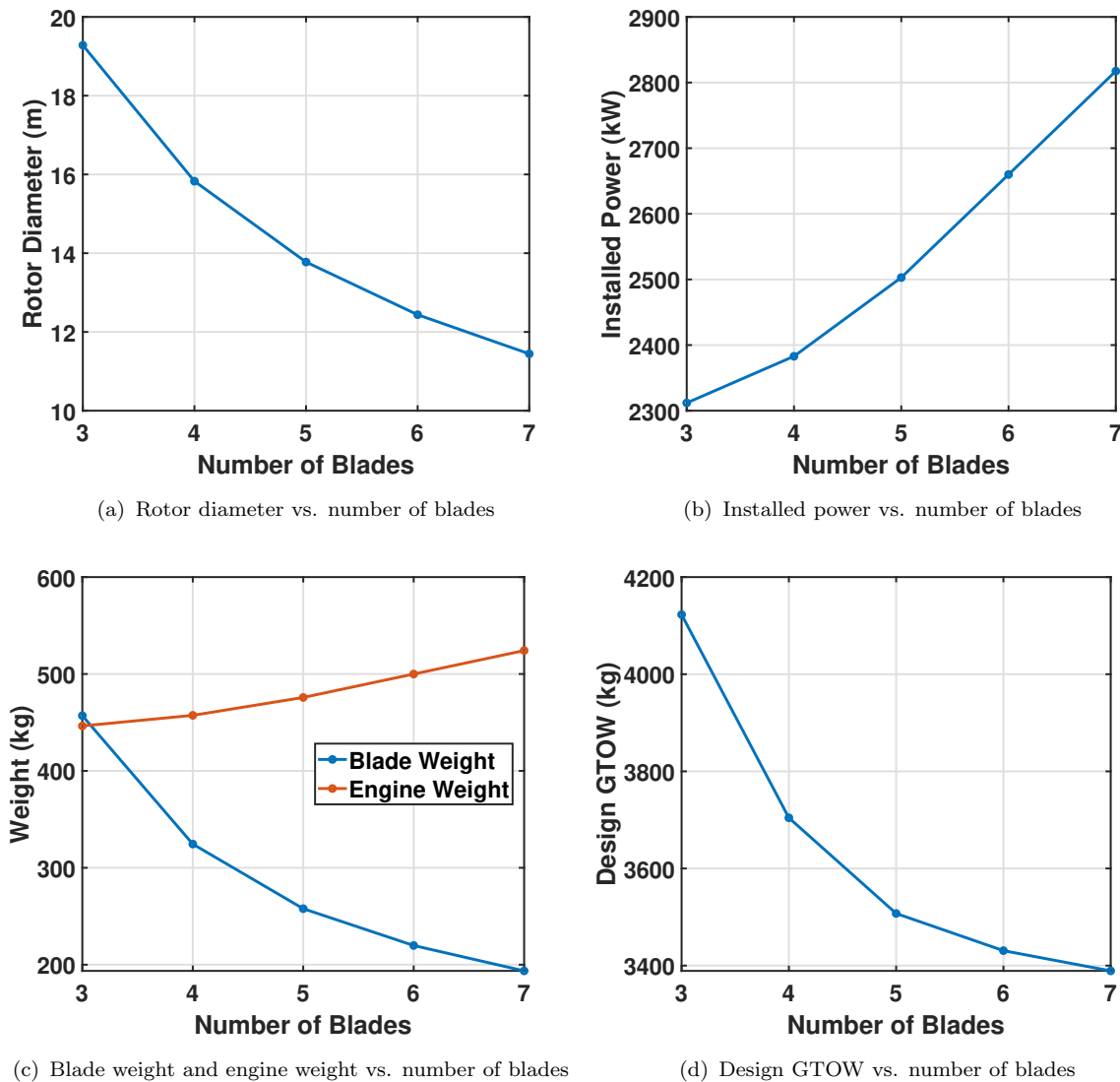


FIGURE 4.3: Trade studies with number of blades for $C_T/\sigma = 0.12$

The installed power, and in turn the engine weight, was determined by the requirement of hover power at 8870 m (29100 ft) by taking into consideration the effects of reduced density and engine lapse rate with both altitude and temperature as required by the RFP. The empty weight, hence



the total weight of the helicopter, is a balance between these two factors. Figure 4.3(c) shows that the blade weight is more sensitive to a change in number of blades than the weight of the engine. The resulting design GTOW for different number of blades is shown in Figure 4.3(d).

Figure 4.4 shows the variation of design GTOW with different number of blades and aspect ratio for $V_{tip} = 231.6$ m/s (760 ft/s). For a fixed aspect ratio, design GTOW is maximum for a 3-bladed rotor and an increase in number of blades generally decreases design GTOW due to the reasons explained before.

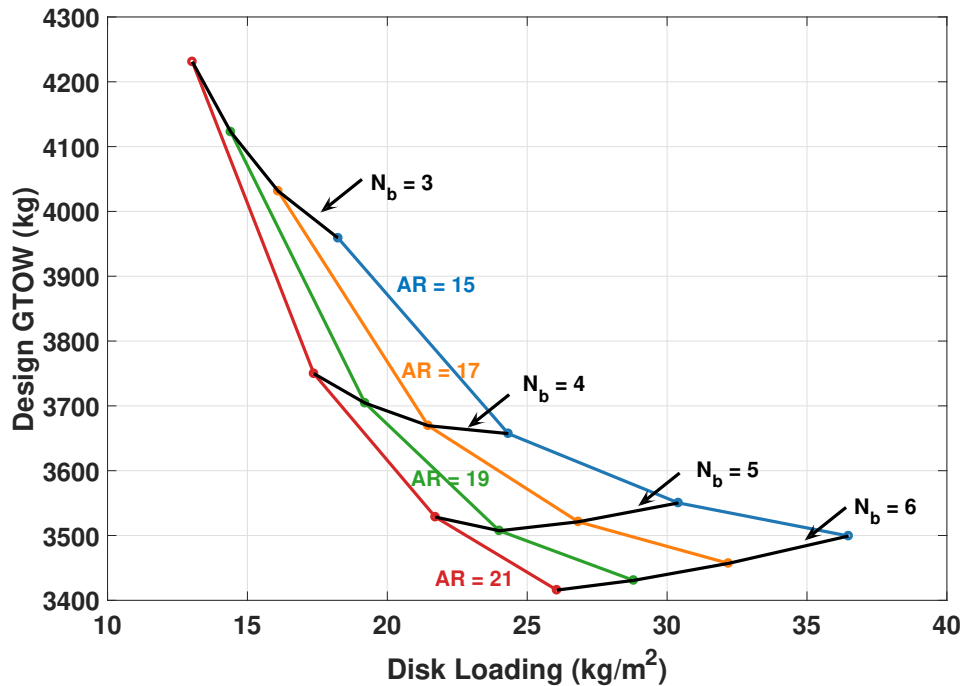


FIGURE 4.4: Carpet plot for design GTOW vs. DL for variations in N_b and AR

On the basis of these results, the following decisions were arrived:

- Configurations with low number of blades (2 and 3) were dropped because of large diameter rotors, higher design GTOW and higher vibrations.
- Configurations with high number of blades (6 or higher) were dropped because of high disk loading (> 24.41 kg/m^2 (5 lb/ft^2)) for some cases) and high installed power.
- The following considerations led to the final selection of a 5-bladed rotor as opposed to a 4-bladed one:
 - A 5-bladed rotor has 12% lower rotor diameter than a 4-bladed one. This results in a compact helicopter which is important for a mountain rescue mission.
 - The design GTOW for the 5-bladed rotor was 6% lower than that of a 4-bladed one whereas the installed power was only 4% higher, a key decision for a mountain rescue mission.
 - 5-bladed rotors have lower vibrations than 4-bladed ones because they filter out frequencies lower than 5/rev and reduce the loading per blade.



4.5.2 Aspect Ratio

With the blade loading and number of blades decided, trade studies were performed to select the aspect ratio and hence the rotor solidity. Analyses were performed at a V_{tip} of 231.6 m/s (760 ft/s). The variation of design GTOW and rotor diameter with respect to aspect ratio is shown in Figure 4.5.

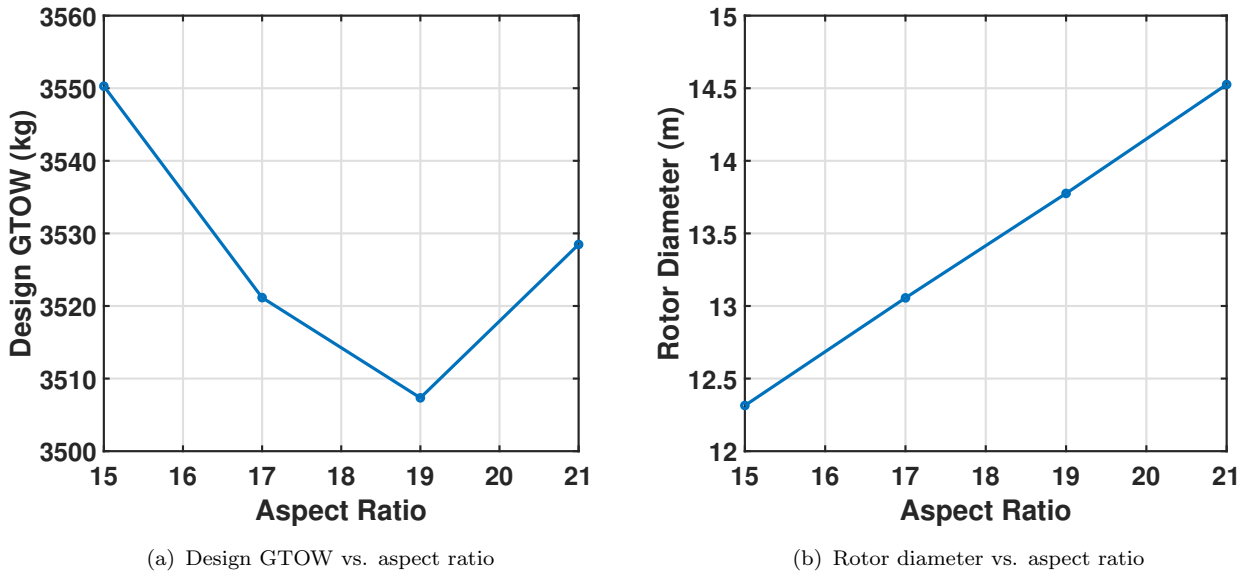


FIGURE 4.5: Trade studies with aspect ratio

Increasing aspect ratio decreases the disk loading, which results in reduced power requirements and hence reduced fuel weight and design GTOW as shown in Figure 4.5(a). However, high aspect ratios also result in larger diameter rotors (shown in Figure 4.5(b)) with shorter chord lengths. Large diameters can increase static droop and can cause problems in gusty wind conditions. Therefore, considering the limitations of very high and low aspect ratios, the extreme values (15 and 21) were eliminated from the selection matrix. Table 4.2 compares two 5-bladed rotor configurations with blade aspect ratios of 17 and 19 at a tip speed of 231.6 m/s (760 ft/s).

TABLE 4.2: Comparison of two configurations designed with different aspect ratios ($N_b = 5$, $V_{\text{tip}} = 231.6$ m/s (760 ft/s), $C_T/\sigma = 0.12$)

Parameter	AR = 17	AR = 19
Solidity	0.0936	0.0838
Diameter	13.06 m (42.83 ft)	13.77 m (45.19 ft)
Engine Installed Power	2640 kW (3540 HP)	2503 kW (3356 HP)
Design GTOW	3521 kg (7763 lb)	3507 kg (7732 lb)
Disk Loading	26.9 kg/m ² (5.49 lb/ft ²)	24.1 kg/m ² (4.91 lb/ft ²)

Keeping all other parameters constant, a lower solidity rotor (high aspect ratio) has lower profile drag and hence a higher Figure of Merit. A significant decrease in installed power and a slight decrease in design GTOW is observed for AR = 19 as compared to AR = 17. There is a 5% increase in rotor diameter, but this drawback is out weighed by the decreases in installed power, design GTOW, and profile drag. In addition, an aspect ratio of 19 provides a disk loading less than 24.41 kg/m² (5 lb/ft²). As a result, an aspect ratio of 19 was chosen for the final rotor design.



4.5.3 Tip Speed

In addition to the usual sizing parameters such as design GTOW, installed power, etc., the tip speed for the design was determined by various factors, namely the effects of compressibility during cruise, retreating blade stall, autorotational flight capabilities, and rotor noise limits. A high rotor tip speed helps decrease the angle of attack on the retreating blade for a given blade area and advance ratio and also provides good autorotational capabilities. However, higher tip speed also increases noise levels and brings significant drag penalties due to compressibility.

A reduction in tip speed at a constant blade loading results in a lower disk loading (Equation 4.1) which decreases the power required, hence a reduction in fuel weight. On the other hand, since a higher tip speed results in a higher disk loading, the rotor diameter and consequently the blade weight and design GTOW decrease. Figures 4.6(a) and 4.6(b) show the variation of design GTOW and installed power with respect to the tip speed for different sized vehicles.

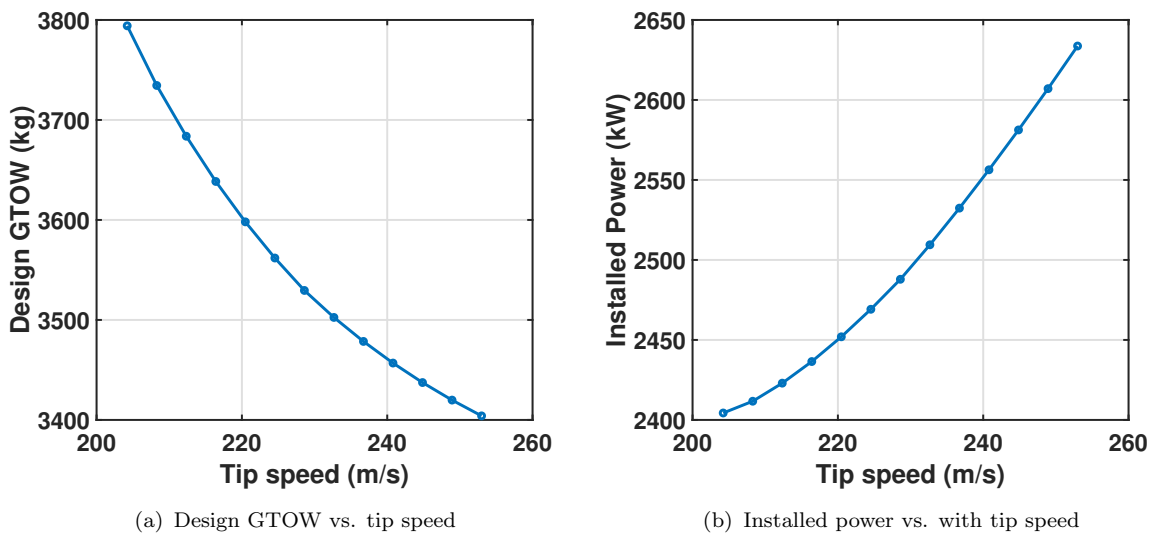


FIGURE 4.6: Trade studies with tip speed

Because the minimum forward speed required to complete the mission within the time specified in the RFP is 293 km/h (158 knots), the reduction of RPM during cruise segments is necessary to avoid compressibility. It was decided to limit the maximum tip Mach number (M) to 0.85. The required RPM reduction was calculated accordingly to follow this limit, which also affects the blade tip design (sweep angle and airfoil). Reduction more than 15% was considered to be impractical due to the loss of efficiency in the turboshaft engine. Figure 4.7 shows the variation of RPM reduction with different tip speeds for a cruise speed of 315 km/h (170 knots) and a tip Mach number of 0.85.

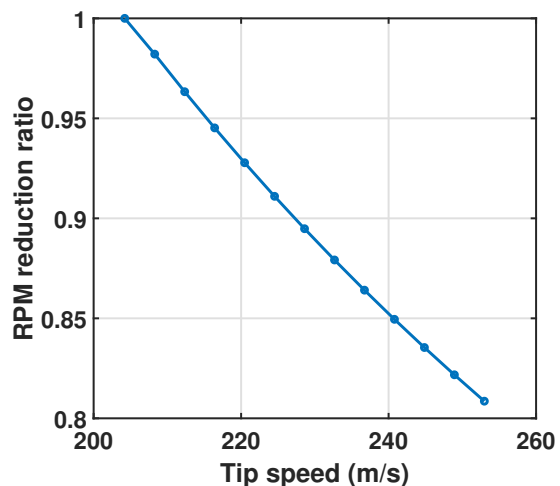


FIGURE 4.7: RPM reduction ratio vs. tip speed

Another advantage of RPM reduction is lower rotor noise in the urban areas. The only disadvantage is increase in the reverse flow region since advance ratio (μ) is greater than 0.4.



On the basis of these results along with some other considerations explained below, the following decisions were made:

- Configurations with low tip speeds (less than 220 m/s (722 ft/s)) were dropped because of large diameter rotors and high design GTOW.
- Configurations with high tip speeds (greater than 235 m/s (771 ft/s)) were dropped because greater than 15% RPM reduction is required during cruise to keep the tip Mach number at 0.85. In addition, high tip speeds result in high installed power.
- Therefore, a suitable choice for tip speed was made between 220 m/s (722 ft/s) and 235 m/s (771 ft/s). The following justifications lead to the final selection of the tip speed as 231.6 m/s (760 ft/s):
 - For $N_b = 5$, $AR = 19$, and $C_T/\sigma = 0.12$, the disk loading is above 24.41 kg/m^2 (5 lb/ft^2) for tip speeds slightly higher than 231.6 m/s (760 ft/s).
 - Reference [15] provides Autorotational Index (AI) of 10 as a safe limit for multi-engine helicopters. Since the critical part of the mission is performed at high altitude (low density), it is beneficial to have higher AI, thereby favoring a higher tip speed (autorotation section in [15]).
 - Compactness was also a factor in choosing this tip speed over the lower ones. A tip speed of 231.6 m/s (760 ft/s) results in a 7% decrease in rotor diameter compared to a tip speed of 220 m/s (722 ft/s).

4.5.4 Cruise Speed

As mentioned before, a minimum cruise speed of 158 knots is required to complete the mission within 175 minutes. However, since leg-2 is the sizing leg, which means that the transmission and the quantity of fuel required are sized by power requirements for the hover segment at the highest altitude, such a design can easily satisfy the requirement of higher cruise speeds in legs 1 and 3. Figure 4.8 show the effect of altitude on torque requirements for specific hover and cruise segments. The transmission torque is determined by the hover segment occurring at the high summit at 8870 m (29,100 ft). However, to equalize the maximum torque requirements at each leg, a speed of 296 km/h (160 knots) is possible for leg 1 which is flown at 3780 m (12400 ft) and 283 km/h (153 knots) for leg 3 flown at 1402 m (4600 ft). The difference in cruise speeds is attributed to different densities at the respective altitudes. With these cruise speeds, *Caladrius* can reach the mission site faster and complete the mission time in 2 hours 55 minutes.

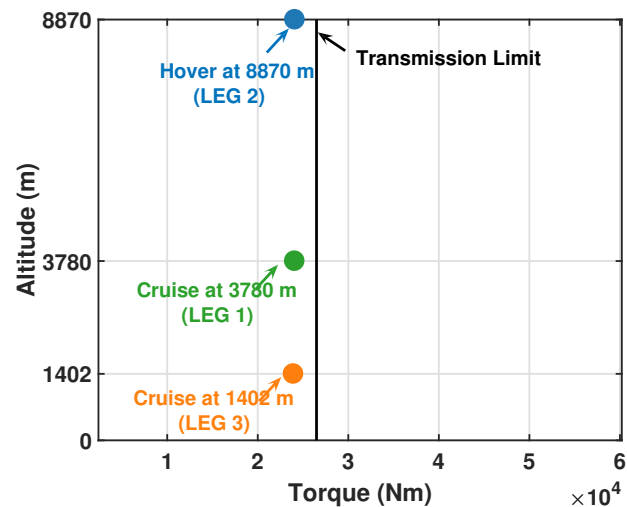


FIGURE 4.8: Altitude vs. torque

4.6 Vehicle Specifications

Caladrius is a 5-bladed single main rotor aircraft designed to rescue people from the highest point on Earth. The final configuration specifications are summarized in Table 4.3. Note that



the design GTOW shown in the table below corresponds to the given high altitude rescue mission.

TABLE 4.3: Summary of vehicle specifications

Parameter	Value (Metric)	Value (English)
Design GTOW	3500 kg	7716 lb
Empty Weight	2667 kg	5879 lb
Fuel Capacity	232 kg	512 lb
Power Required (SL, ISA)	2502 kW	3353 HP
Installed Power (SL, ISA)	2894 kW	3880 HP
Main Rotor Diameter	13.76 m	45.14 ft
Main Rotor Number of Blades	5	5
Main Rotor Aspect Ratio	19	19
Main Rotor Solidity	0.0838	0.0838
Main Rotor Disk Loading	24 kg/m ²	4.82 lb/ft ²
Main Rotor Blade Loading	0.12	0.12
Main Rotor Hover Tip Speed	231.6 m/s	760 ft/s
Rotor Speed in Hover	33.6 rad/s	320.5 RPM
Rotor Speed in Cruise for Leg 1	29.5 rad/s	282 RPM
Cruise Speed for Leg 1	296 km/h	160 knots
Rotor Speed in Cruise for Leg 3	31.3 rad/s	299 RPM
Cruise Speed for Leg 3	283 km/h	153 knots
Cruise Speed for Leg 3	283 km/h	153 knots
Never Exceed Speed, V_{NE}	315 km/h	170 knots
Total Mission Time	2 hours 55 minutes	2 hours 55 minutes

5 Blade Aerodynamic Design

5.1 Design Goals

Caladrius is a single main rotor helicopter designed for rescue missions over Mount Everest. While hover at the high altitude of 8870 m (29100 ft) is critical and one of the most crucial design drivers for the vehicle, efficient and fast operation in legs 1 and 3 are also essential to complete the mission within three hours and transport the rescuees to a nearby hospital as quickly as possible. Hence, the main rotor has to be designed for both efficient hover at high altitude and efficient edgewise flight at the cruise altitudes.

The design of a rotor to achieve these goals presents a significant challenge due to the difference in flow conditions during hover and cruise segments of the mission. A rotor for efficient hover requires high twist and taper in order to make the inflow distribution as close to ideal (uniform) as possible and to ensure that the blade airfoil sections operate near their optimum angles of attack. On the other hand, low twist and taper are favored for efficient cruise. Moreover, due to edgewise flow in cruise, blade tip airfoil sections on the advancing side experience transonic flow while the airfoil sections on the retreating side experience stall and reverse flow. Hence, the final rotor design of *Caladrius* is an intricate trade-off between an optimum hovering rotor and an optimum rotor for high speed forward flight.



5.2 Design Methodology

Rotor design was carried out using in-house developed codes to predict the performance of the rotor in both hover and cruise. Blade element momentum theory (BEMT) analysis was used to study the hover performance (Figure of Merit) of the main rotor blade. Unlike a typical BEMT analysis, no small angle assumptions were made due to the large inflow angles expected in high updrafts. The analysis also included Prandtl's tip loss factor [15] to account for blade number and 3D effects at blade tip. For cruise efficiency calculations (L/D of the vehicle), a full vehicle trim solution was developed. The analysis used a blade with a flap frequency of 1.06/rev and a fuselage with a flat plate area of 1.2 m² (12.92 ft²). Drees's linear inflow [15] was used for forward flight analysis. In addition, airfoil tables containing variation in aerodynamic coefficients (C_l , C_d , and C_m) with Mach number and angle of attack were used in both the analyses. The airfoil tables were extracted using 2D RANS and validated with test data.

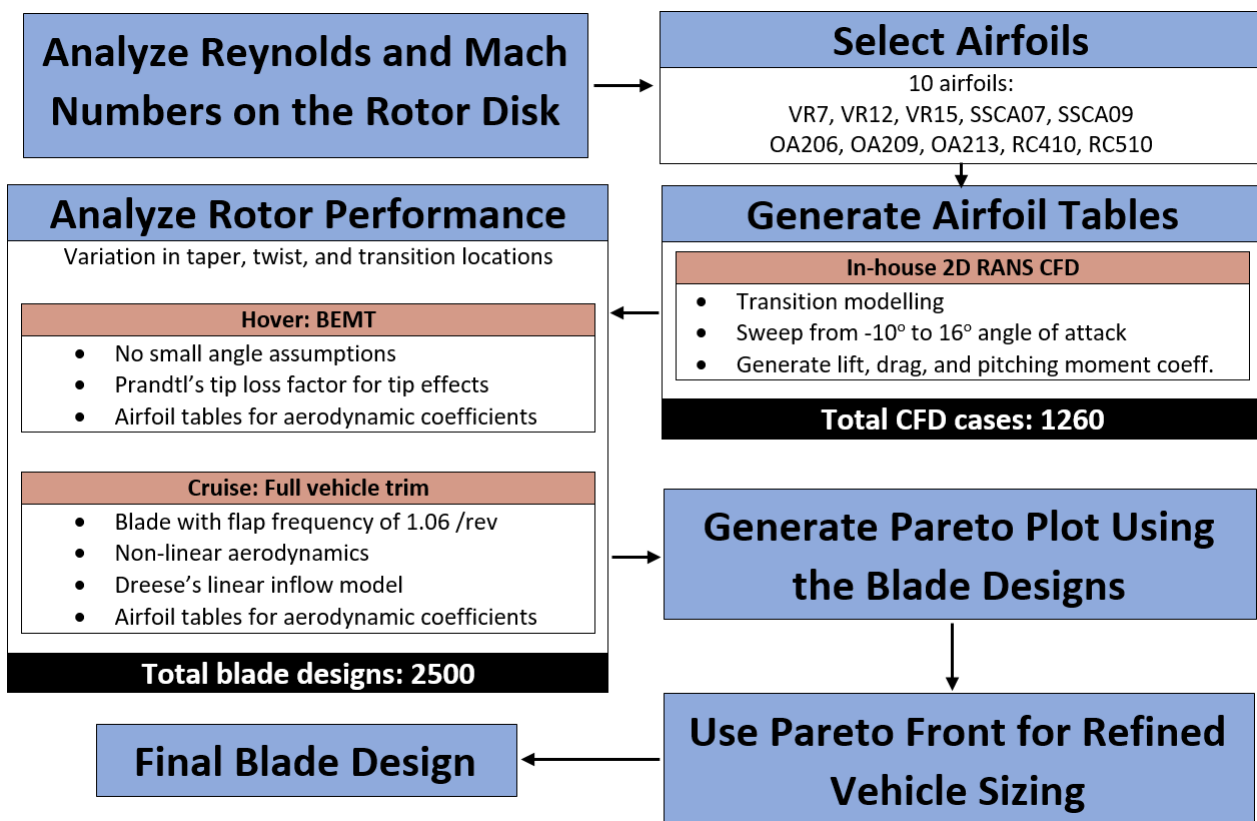


FIGURE 5.1: Schematic outline of the process for blade aerodynamic design

The blade aerodynamic design was carried out in steps shown in Figure 5.1 and outlined below:

1. A study of Reynold's number (Re) and Mach number (M) of the rotor disk during hover and cruise was carried out to understand the different aerodynamic conditions experienced by the blade sections.
2. Based on this study, 10 airfoils were selected for different sections of the blade.
3. An in-house two dimensional Reynolds-Averaged Navier-Stokes solver (2D RANS) [16],[17] was used to analyze the chosen airfoils and calculate their aerodynamic coefficients (C_l , C_d , and C_m) for different angles of attack and Mach numbers.



4. The generated airfoil tables were used to study the max C_l/C_d , $C_{l_{\max}}$ and drag divergence Mach number (M_{dd}) of the airfoils. Based on this study, the final airfoils for different sections of the blade was selected.
5. Using the selected airfoils, Figure of Merit (FM) and vehicle lift over drag (L/D) were calculated for different blade geometries. The geometry variation was obtained by using linear taper, bilinear twist, and twist and airfoil transition locations along the span.
6. A Pareto plot was obtained from these studies. Since both hover and cruise performance are important for this mission due to 30 minute hovering and high cruise speeds, a few points were selected from the Pareto front and were used in the in-house vehicle sizing code to decide on the best blade design.

5.3 Airfoil Selection

Airfoil selection requires the knowledge of Reynold's number and Mach number at which the blade sections will operate. Figure 5.2 shows that Reynold's number over most of the rotor disk is above a million. For $Re > 10^6$, change in lift and drag coefficients with Reynold's number is small; hence, it is not a significant criteria for airfoil selection. On the other hand, the influence of Mach number, is important above $M = 0.3$. It can be seen from Figure 5.2 that a large portion of the rotor disk operates at Mach numbers greater than 0.3. During hover, the Mach number variation on the disk is axisymmetric and reaches $M = 0.73$ as the maximum. This suggests that an airfoil with high C_l/C_d up to that Mach number can be used for the entire blade for good hover performance. However, a rotor designed in this way might have poor cruise performance as Mach number changes significantly and is no longer axisymmetric during edgewise flight. Figure 5.2 shows that the maximum Mach number during cruise (0.85) occurs at the blade tip on the advancing side of the rotor. Hence, transonic effects are also important, especially for airfoils in the tip region of the rotor blade. Another important observation from the figures is that the entire reverse flow and stall region occurs in the section of the rotor disk with a $M \leq 0.3$. This suggests that post-stall performance of airfoils can be analyzed without taking compressibility into account. This insight made the process of airfoil table generation using 2D RANS faster and much easier later on in the design process.

Taking the above factors into consideration, the following airfoils (Table 5.1) were selected to be analyzed further. These are second generation rotorcraft airfoils with C_l/C_d and $C_l^{3/2}/C_d$

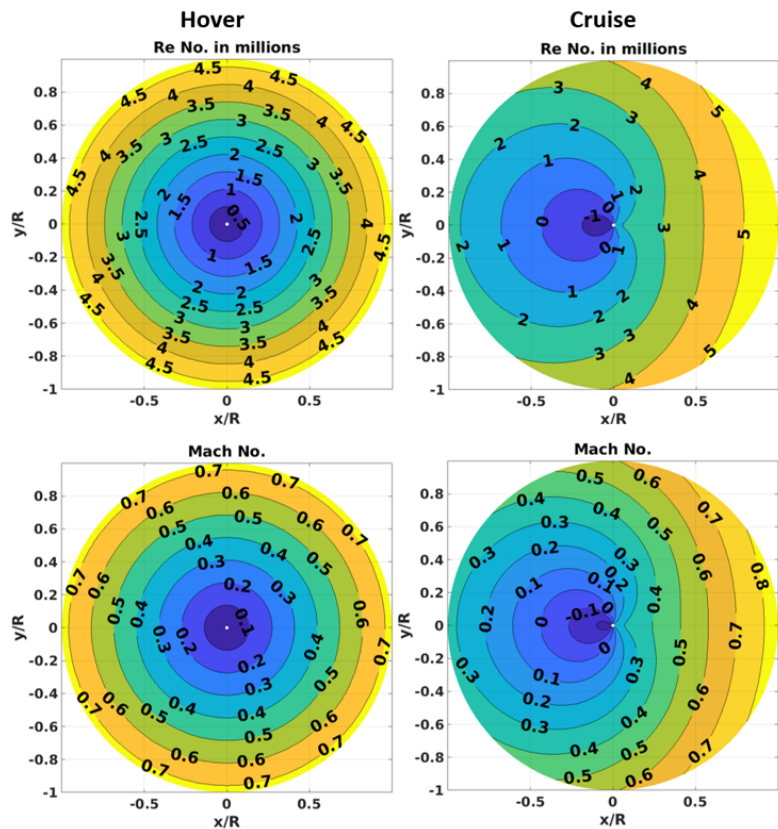


FIGURE 5.2: Reynold's and Mach number on rotor disk



significantly higher than those of the first generation rotorcraft airfoils such as NACA0012 and NACA 230-series [15, 18].

TABLE 5.1: List of selected airfoils

VR7	VR12	VR15	RC410	RC510
SSCA07	SSCA09	OA206	OA209	OA213

Airfoil Selection Criteria:

- Airfoils with high C_l/C_d to optimize performance
- High $C_{l_{\max}}$ for $M < 0.3$
- Airfoils with high M_{dd} for blade tip

Performance data for some of the above mentioned airfoils are not available in public domain. Hence, an in-house two dimensional Reynold's Averaged Navier Stokes solver (2D RANS)[16],[17] was used to analyze and calculate the aerodynamic coefficients for these airfoils and the results are presented in Figures 5.3 to 5.5.

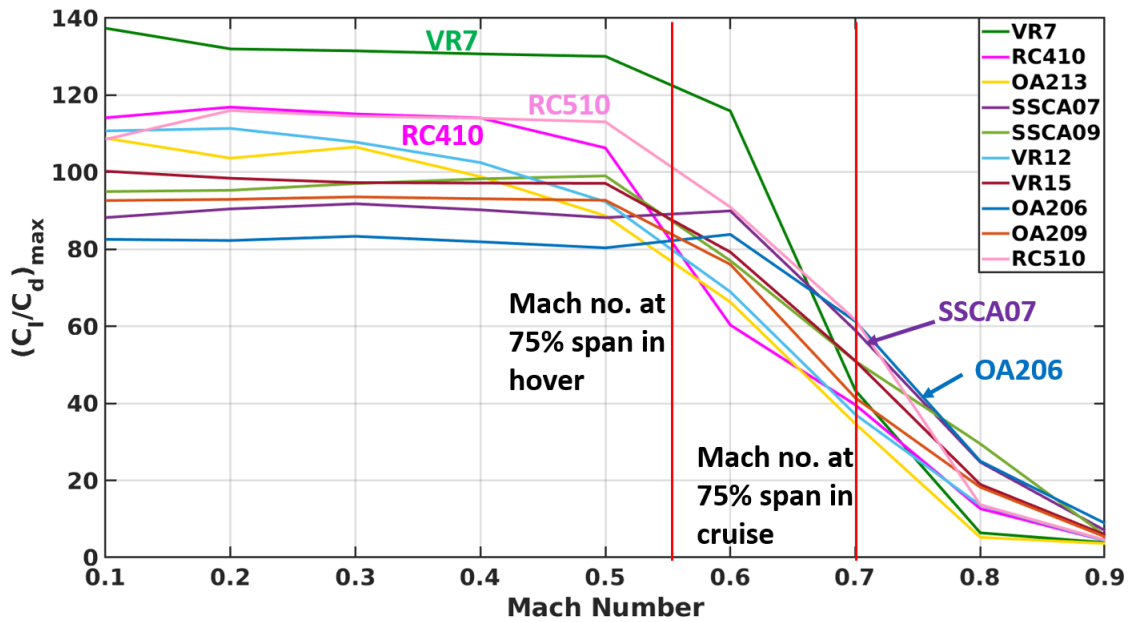
FIGURE 5.3: Maximum C_l/C_d of different airfoils

Figure 5.3 shows that C_l/C_d of VR7 airfoil is much higher than that of other airfoils until a Mach number of 0.65. In addition, it is observed from Figure 5.4 that VR7 also has high $C_{l_{\max}}$. Hence, it is an appropriate airfoil for good hover performance. However, it is not a suitable tip airfoil as it has a low M_{dd} of 0.75 and low C_l/C_d for Mach numbers greater than 0.65. Hence, VR7 was chosen as the airfoil for the inboard and middle sections of the rotor blade. The only disadvantage of using VR7 is its relatively high pitching moments than other rotorcraft airfoils, but this has been addressed in the pitch link design section (6.2.4).

Figure 5.5 shows that both SSCA07 and OA206 are good tip airfoils as they both have high M_{dd} . In addition, from Figure 5.3 it can be seen that the C_l/C_d of these airfoils is relatively better than most other airfoils in the advancing section of the rotor disk. However, OA206 has a lower thickness to chord ratio (6%) than SSCA07 (7%) which might create complications for the structural design; hence, SSCA07 was chosen as the tip airfoil.



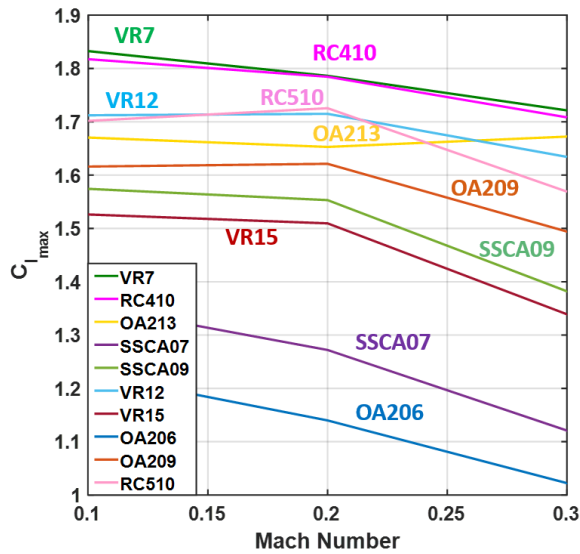
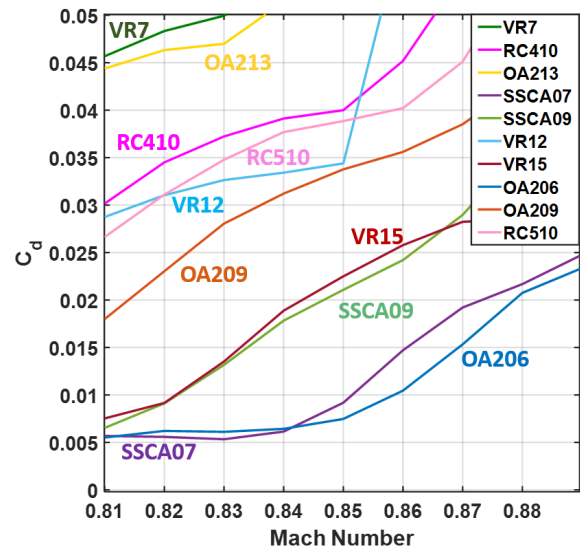
FIGURE 5.4: $C_{l_{\max}}$ of different airfoils

FIGURE 5.5: Drag polar of different airfoils

5.4 Blade Tip Design

The selected tip airfoil (SSCA07) has a drag divergence Mach number of about 0.85 which is incidentally same as the maximum Mach number on the rotor disk during cruise. However, it is always beneficial to have some margin for variations in atmospheric conditions and rotor speed. Hence, it was decided to maintain the maximum normal Mach number of 0.82 at the blade tip. Figure 5.6 shows the amount of blade sweep required at the tip, for different advance ratios. Since *Caladrius* has a cruise advance ratio of 0.4, the corresponding nonlinear sweep variation for the tip was selected from the figure. This leads to sweep starting from 95% of the blade to a maximum sweep of 15° at the tip.

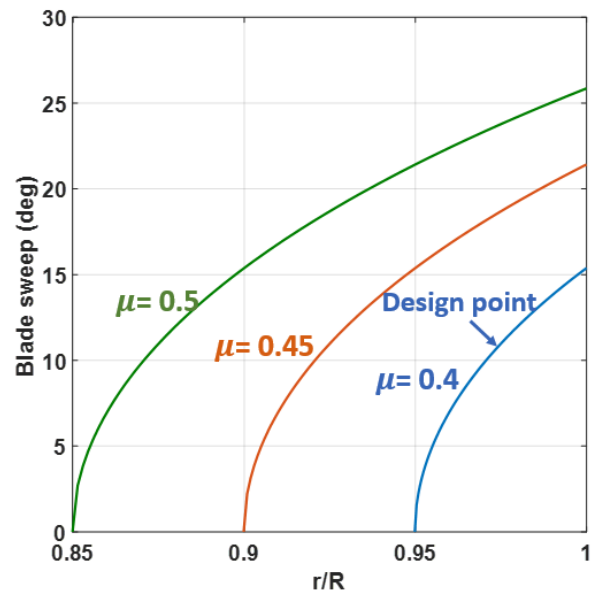


FIGURE 5.6: Tip sweep to maintain a maximum normal mach number on leading edge of 0.83

Anhedral at the blade tip is known to increase hover performance [19], and good hover performance is critical for *Caladrius's* mission at the peak of Mount Everest. Research at ONERA [20] have also shown them to be beneficial for high speed forward flight ($\mu \geq 0.4$) performance. Another important benefit of anhedral is reduction in Blade Vortex Interaction (BVI) by increasing the blade-vortex miss distance. Because of these benefits, an anhedral of 25° was incorporated at the blade tip (95% to 100% radius), which is similar to other advanced helicopters of similar weight class. The effect of anhedral was validated using an in-house 3D RANS solver (GARFIELD) [21, 22] for *Caladrius's* blade. These results for hover are shown in Figures 5.7 and 5.8.



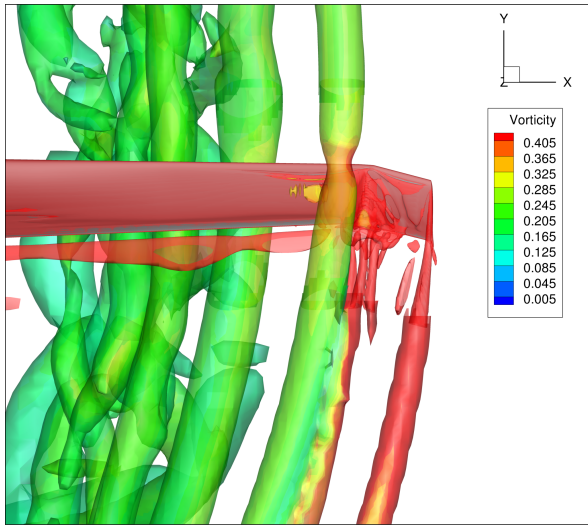


FIGURE 5.7: High Blade vortex interaction in the absence of anhedral tip

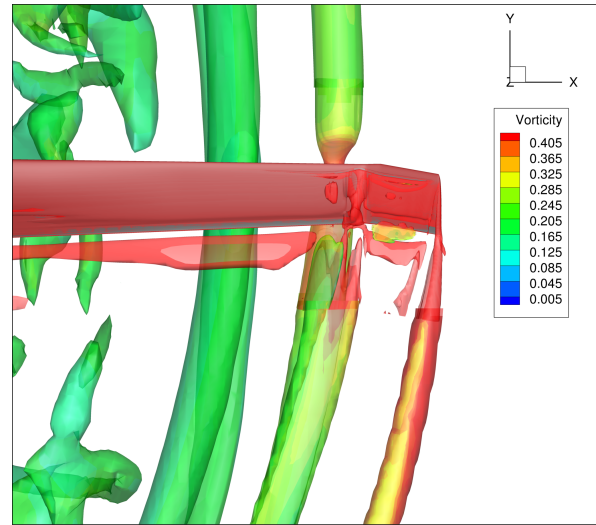


FIGURE 5.8: Anhedral tip reduces Blade Vortex interaction in hover

5.5 Trade-Study on Blade Geometry

Using the selected airfoils and blade tip, a parametric sweep on different blade geometries was performed. These included variations in airfoil transition location, linear twist and taper, and bilinear twist and twist transition location. A total of 2500 blade geometries were investigated. The results are shown in the Pareto plot in Figure 5.9. The plot clearly shows that both efficient hover and efficient cruise cannot be achieved with the same blade design. There is always a trade-off between the two operating conditions of the rotor. In order to choose a proper design point from this plot, a study on the effect of different aerodynamic designs on the entire mission is necessary. The Pareto front from this figure was used in the in-house sizing code to estimate this effect. Interviews with pilots such as Didier Delsalle and Samuel Summermatter showed that they always prefer a lighter helicopter for rescue missions. Hence, it was decided that among the multiple design options available on the Pareto front, the one with minimum vehicle weight will be used. The results of this study are shown in Figure 5.10.

Figure 5.10 shows that two points on the Pareto plot result in a vehicle with minimum weight. One of these points requires a rotor blade with taper ratio of 3.5 which is difficult to manufacture. This favored the selection of the other point, which has a taper ratio of 2.5. Even a taper of 2.5 can have associated high manufacturing complexity and cost. Moreover, Ref. [23] suggests that blades with rectangular inner planform and taper point starting from middle to outboard sections of the blade can have similar performance. Hence, variations of the selected design were further investigated by using rectangular planform (no taper) for the inner 50% the blade. The results confirmed that doing so has little to no effect on blade's aerodynamic performance. Hence, based on manufacturability and cost considerations, the new geometry was selected for the final main rotor blade design which is shown in Figure 5.11.

5.6 Final Blade Design

Figure 5.11 shows the final main rotor blade geometry and airfoils of *Caladrius*. Because the mission is hover dominated, the blade employs both bilinear taper and bilinear twist to achieve a high Figure of Merit of 0.83 at 8870 m (29100 ft) while still achieving a good forward flight L/D of 4.18. High performance VR7 airfoil is used for the inboard sections of the rotor blade while

SSCA07 airfoil is used at the tip because of its high drag divergence Mach number. In addition, the tip is swept to avoid transonic effects, while maintaining a high tip speed in forward flight. The tip also has an anhedral to alleviate the noise and vibrations from potential Blade Vortex Interaction (BVI) and also to improve hover performance.

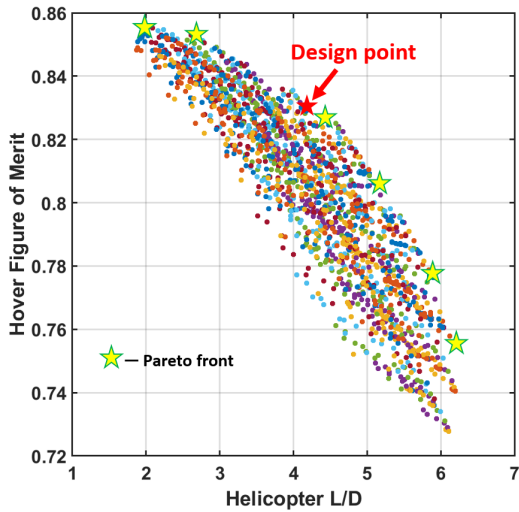


FIGURE 5.9: Pareto plot for main rotor blade

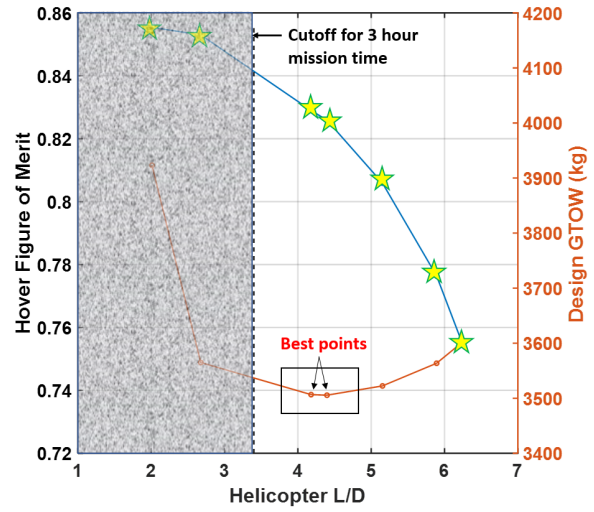


FIGURE 5.10: Effect of main rotor aerodynamic design on vehicle sizing

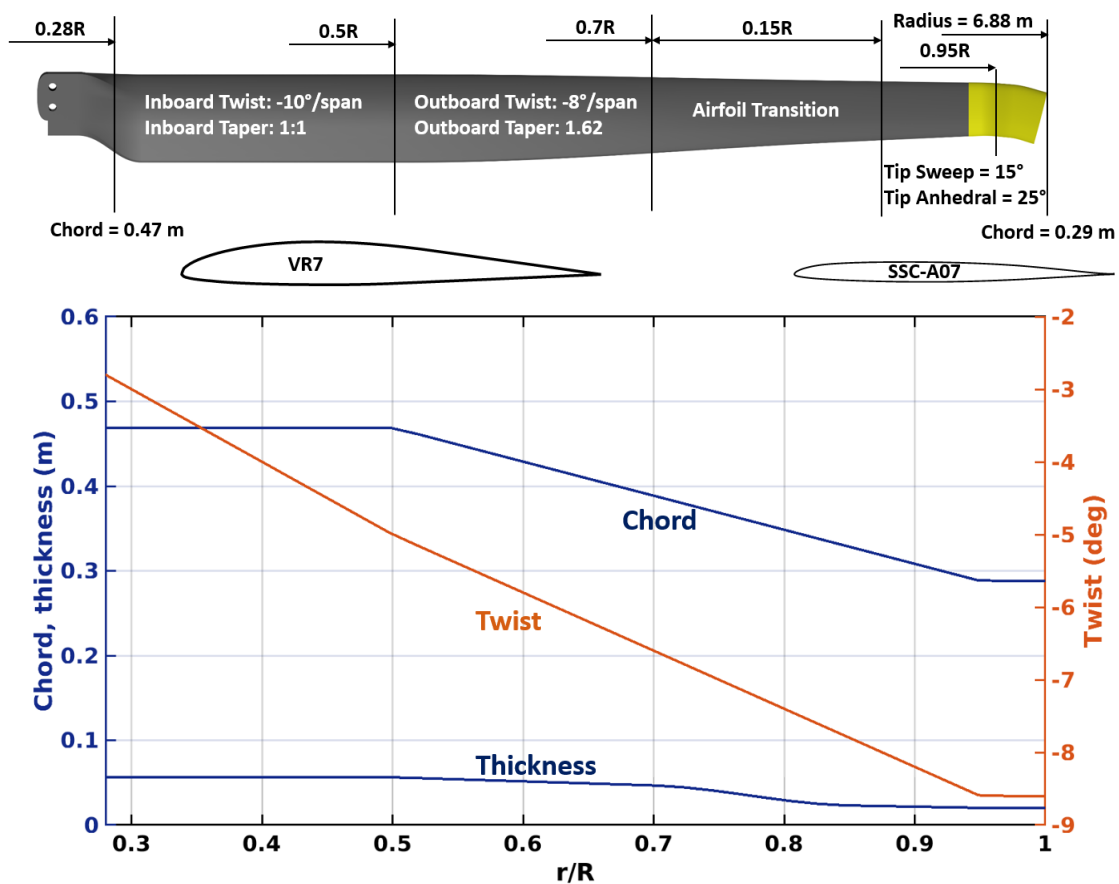


FIGURE 5.11: Geometry of *Caladrius's* blade



Another important feature of this rotor is high stall margin. As shown in Figure 5.12, the main rotor of *Caladrius* can achieve a C_T/σ as high as 0.19, while hovering at an extreme altitude. This is primarily due to the use of VR7 airfoil which has high $C_{l_{max}}$. As a result, the rotor can withstand an updraft up to 22 knots.

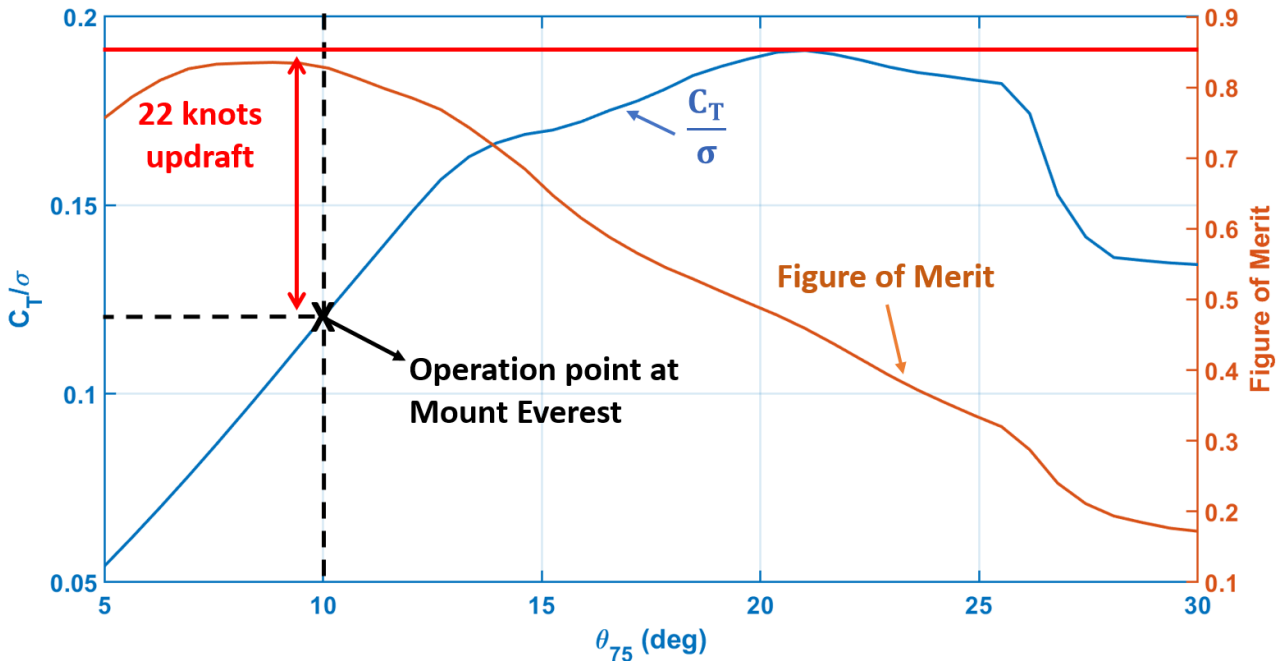


FIGURE 5.12: Stall limit of *Caladrius's* rotor in vertical gusts at 8870 m

6 Hub Design

The rotor hub holds the blades, absorbs the loads, ensures stability and connects the load path to the main shaft. It acts as a filter, transmitting only loads that are integer multiples of N_b/rev . *Caladrius's* hub was designed for both steady and oscillatory hub forces and moments, along with a fatigue life of 5000 hours. Different types of hubs were analyzed to decide the final hub design. A bearingless hub was selected. A detailed assembly of the hub, swashplate and pitch links along with the necessary components is provided in this section.

6.1 Hub Selection

Six selection criteria were considered for the hub design of *Caladrius*. Conditions at the high summit demanded a rotor design that is tolerant to severe gusts, while still providing enough control authority to precisely position the helicopter during the rescue operation. This was a key input received directly from the experienced pilots. In addition, a hub system which leads to lower vibrations and lower drag in cruise would be suitable for the mission which has two important cruise segments. Apart from these, the hub assembly should not be complex (low number of parts) and should be robust, protected from snow environments, thereby increasing the life of the components.

Figure 6.1 shows the hub selection matrix where different hub types were rated for each of the criteria considered in the selection process. A grading scale from + (very good) to - (very bad) with 0 being moderately good and bad was used for rating. For example, Hingeless rotor has more control authority due to hub moments (a + score) compared to an articulated rotor (a - score) with semi-articulated in between (a 0 score).

TABLE 6.1: Hub selection matrix

Type of Hub	Gust Sensitivity	Control Power	Vibrations	Hub Drag	Robustness	Number of Parts	Total
Articulated	+	-	+	-	-	-	-2
Semi-Articulated	0	0	0	0	-	0	-1
Hingeless	-	+	-	+	-	+	0
Bearingless	0	0	0	+	0	+	2

Articulated: Articulated hubs utilize mechanical hinges in flap, lag, and pitch, which makes them mechanically complex with a high number of parts. Due to low hinge offset values (first flap frequency close to 1.02/rev), they do not provide ample control authority and are therefore not well suited for *Caladrius's* high altitude rescue mission.

Semi-Articulated: Semi-articulated hubs use flexures for flap and elastomeric bearings for pitch and lag motions. They are moderately gust tolerant and provide some control authority for the pilot during the rescue operation. However the use of elastomeric bearings and relatively higher number of parts decrease robustness and increase complexity.

Hingeless: Hingeless hubs use a flexure to control both flap and lag motions while still using a bearing to control the pitch motion. They provide good control authority; however, they are also gust sensitive and require elastomerics for damping augmentation, therefore less suited for the extreme weather conditions at the high altitude.

Bearingless: Bearingless hubs use a flexure to control flap and lag motions but also use a torque tube (pitch case) to control pitch motions avoiding a pitch bearing. They offer a simple structure due to the absence of hinges and bearings, which reduces the total weight and the number of parts (about 75% reduction compared to articulated rotors and 15% reduction compared to hingeless rotors [24]). The motion of the pitch case relative to flexure enables the insertion of a lag damper more easily than hingeless rotor, thereby allowing a softer rotor in plane and lower chordwise loads. Manufacturing costs are also reduced while reliability and maintainability are improved. More importantly, the flexbeam can be designed to provide adequate control authority needed during the rescue operation and at the same time providing low sensitivity to gusts. They provide a hub which can withstand the extreme weather conditions of *Caladrius's* mission with minimal maintenance. These hubs have clean aerodynamic profiles with low number of parts and have a long fatigue life, thereby making them a robust design. Based on these considerations, the bearingless hub configuration is selected for *Caladrius*.

6.2 Hub Design

The bearingless hub primarily consists of a flexure (called flexbeam) for pitch, flap, and lag motion, a torque tube, a pitch link to produce the blade pitch motion and an elastomeric damper to provide lead-lag damping. A soft in-plane rotor was planned for low in-plane loads; a lag frequency of around 0.7/rev was targeted. A first flap frequency was aimed at around 1.06/rev in order to strike balance between control authority and gust sensitivity. A higher first torsion frequency was aimed for better aeroelastic stability. Judicious construction of all the hub components shown in Figure 6.1 and the multiple load paths that connect are at the heart of the design. These components are explained in detail in the following subsections.



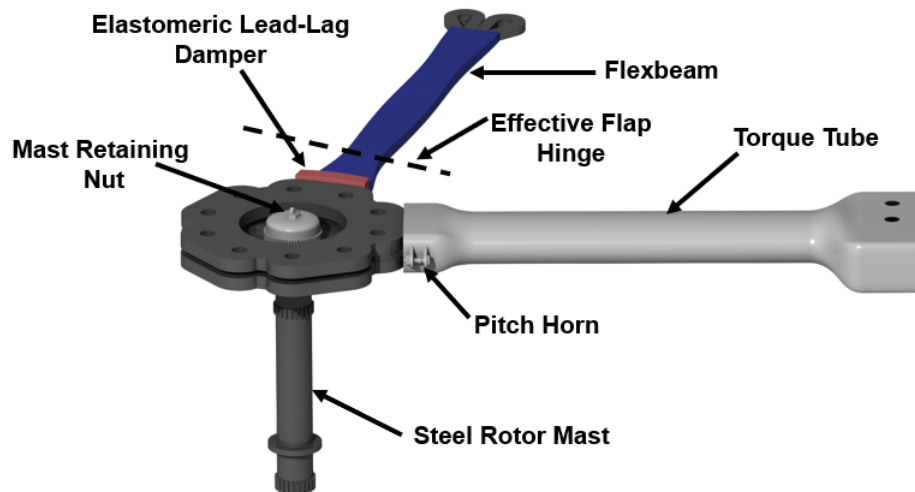


FIGURE 6.1: Main rotor hub components

6.2.1 Flexbeam

The flexbeam carries the centrifugal force, torsion, flapping, and lead-lag moments of the blade. The blade flap, lag, and pitch motions are achieved via the flexbeam with a rectangular cross-section. Rectangular cross-section was selected for the flexbeam because manufacturing procedure is simpler compared to that of hollow ribbed sections. The chord and thickness vary nonlinearly along the length of the flexbeam and are optimized to achieve the desired stiffness properties and location of the virtual flap and lag hinges. Figure 6.2 shows the planform of the optimized flexbeam.

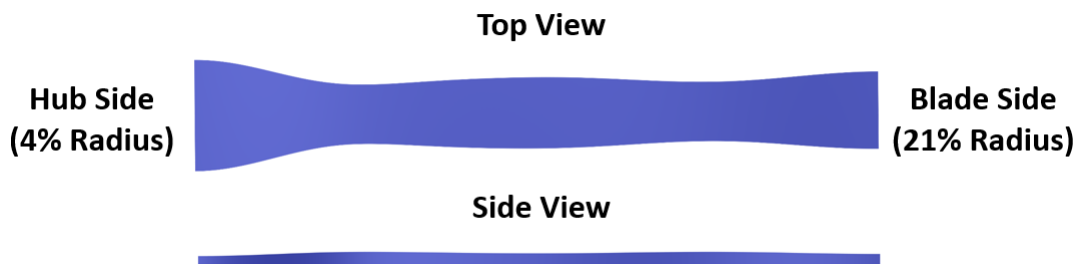


FIGURE 6.2: Flexbeam

The flexbeam, which is soft in torsion, is made of unidirectional E-glass fibre/epoxy. E-glass fibre was chosen due to its flexibility, long fatigue life, few handling problems, ease of manufacturing, and low cost. It is rigidly bolted and cantilevered to the hub at its root end. It connects to the rotor blade at its outboard end and is surrounded by the torque tube. The length of the flexbeam is 17% of blade radius, with the effective flap hinge around 7.5% of blade radius as shown in Figure 6.1. Using in-house CAD and 3D FEA tools (X3D), minute pieces were chipped away until the flexbeam and cuffs were chiselled into their optimal shapes that carry no more weight than the loads and fatigue conditions require.

6.2.2 Torque Tube

The main function of the torque tube is to transmit the torsional moments of the blade. The torque tube, which surrounds the flexbeam, is connected to the blade at its outboard end at 21% radius and to the pitch link at its inboard end. An elliptical cross-section was selected for the



torque tube to provide some aerodynamic benefits. It has a significantly higher torsional stiffness than the flexbeam and is made of graphite/epoxy composite. Therefore, a vertical motion of pitch link pitches the rotor blade via a rigid rotation of the torque tube and elastic twist of the flexbeam.

6.2.3 Elastomeric Lag Damper

An elastomeric lead-lag damper is provided to augment lead-lag stability of the soft in-plane *Caladrius* hub. Elastomeric dampers are better than hydraulic dampers due to their longer service life, high reliability and effectiveness over a wide range of temperatures and frequencies. The damper is located at the hub end of the flexbeam, bolted to the flexbeam on both top and bottom surfaces and it works in shear.

6.2.4 Pitch Horn and Pitch Link

The pitch horn for *Caladrius* is attached directly to the torque tube. The pitch horn contains a ball joint connection to the pitch links, chosen to alleviate the bending stresses on the pitch links. The midpoint of the ball joint is offset from the torque tube such that a pitch range of 40° is obtained for the main rotor without the pitch link striking the torque tube. Initially, the pitch horn was placed at the virtual flapping hinge to avoid pitch-flap coupling (δ_3 angle). This decision was taken to keep the flap frequency constant at different altitudes. However, after interviewing several pilots that have experience at different altitudes, it was determined that the vacuum frequency of the rotor is what determines the controllability of the aircraft. In addition, placing the pitch horn at the virtual flapping hinge lead to problems with the swashplate (Section 6.3). After further analysis, the pitch horn was placed inboard of the virtual flapping hinge at the trailing edge of the blade resulting in stabilizing pitch flap coupling of 25° . Pitch links are inclined in chordwise direction to obtain negative pitch-lag coupling (α_4 coupling) which is beneficial for air resonance stability.

The length and the diameter of the pitch links were sized using two criteria. First, to minimize the bending loads on the pitch links, a maximum angle (deviation from vertical) was chosen. This value, when combined with the chordwise location of the pitch horn from the pitching axis and the maximum required pitch angle results in the pitch link length. Next, to determine the pitch link radius, maximum pitching loads were used to check three major failure cases. Pure axial loading, axial loading with bending stress, and buckling were all used to size the pitch links. Due to the critical nature of the component, a safety factor of 10 was used for this sizing procedure. Finally, two different materials were tested: aerospace grade stainless steel and grade 5 titanium. Although the titanium can provide the same factor of safety at a lower weight, steel was chosen for the pitch links due to significantly lower cost and ease of manufacturing.

6.3 Swashplate Design

Several control actuation techniques were considered for *Caladrius*, each with its own appeal. The use of trailing edge flaps, shown to have potential for higher harmonic control [25] was considered due to reduced weight. However, the use of trailing edge flaps requires a very low torsional frequency, leading to aeroelastic stability issues. These were dropped as they were less mature and may not be adequate for high bandwidth gust tolerance and agility. Individual blade control(IBC) mechanism was also considered for the design. The use of IBC requires hydraulic actuators which replace pitch links and swashplate. These actuators are required to have a high actuation rate (one cyclic per revolution) and to provide adequate torque to counter the



pitching moment generated by each blade. All these requirements lead to relatively large and heavy actuators with a hydraulic support system, which is not ideal for a high altitude rescue mission, where every pound of weight is a premium. Therefore, a conventional tried and tested swashplate design was chosen for *Caladrius*.

The swashplate system of *Caladrius* is bolted to the top of the static mast, and an aluminum sleeve extends along the shaft to support the swashplate as shown in Figure 6.3. An aluminum spherical bearing is placed on the outside of the sleeve, and another low friction sleeve made of steel coated kevlar is placed between the bearing and the sleeve to allow the bearing to shift up and down. The non-rotating swashplate bolts onto the spherical bearing, allowing full rotation about the two axes.

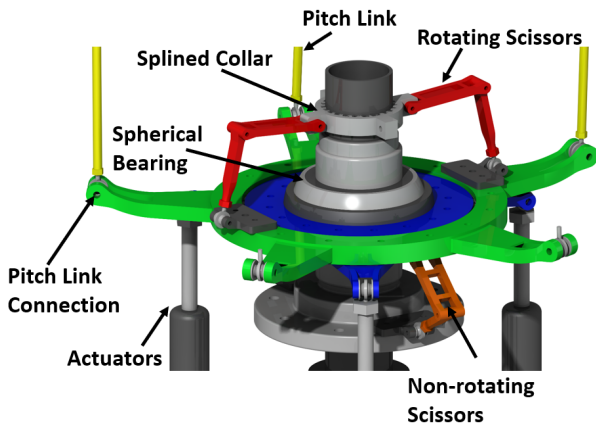


FIGURE 6.3: Swashplate assembly

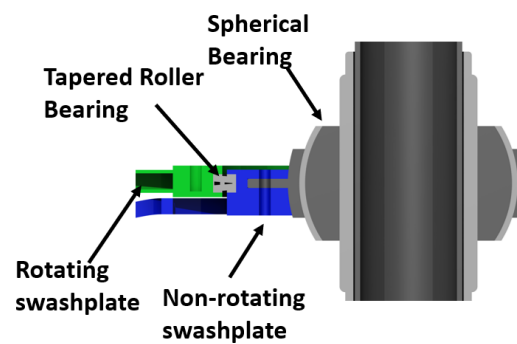


FIGURE 6.4: Cross-sectional view of the swashplate

A scissor linkage connects the rotating swashplate to matching splines on the shaft via a splined collar. This transmits the torque from the shaft to the rotating swashplate, leaving the pitch links to carry almost exclusively axial loads. The rotating swashplate is divided into two portions, an upper and lower portion, which fit together around a tapered roller bearing, which also attaches to the non-rotating swashplate as shown in Figure 6.4. A tapered roller bearing is used to allow rotation while transmitting the pitch link loads to the rest of the swashplate system. The other end of the roller bearing attaches to the non-rotating swashplate, which is supported by the hydraulic actuators. A fixed scissor linkage connects the non-rotating swashplate to the base of the aluminum sleeve, constraining the non-rotating swashplate from rotating with the rotor and minimizing the bending loads on the actuator rods.

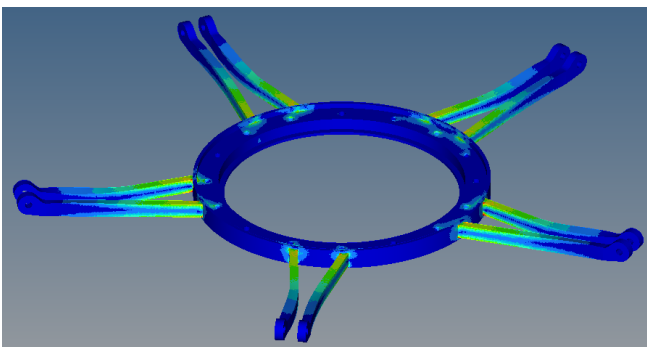


FIGURE 6.5: Original swashplate

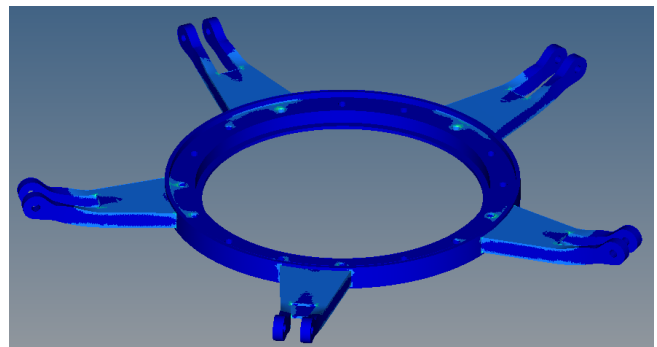


FIGURE 6.6: Refined swashplate

As mentioned in Section 6.2.4, the pitch horn was originally placed at the virtual flap hinge. Due to the large radius of the blade, the radial position of the pitch link was large, resulting in long arms on the rotating swashplate. This design was analyzed using a high fidelity 3D

FEA tool and the factor of safety was found to be less than two. Much like the pitch links, the swashplate is a critical component, and as such a factor of safety of at least five was desired. In order to achieve this, the radial location of the pitch horn was decreased and flanges were added at the inboard half of the swashplate arm to relieve the bending moments as shown in Figures 6.5 and 6.6. The finalized rotating swashplate design has a factor of safety greater than five, and additionally has a 10% weight reduction compared to the original model.

To summarize, a bearingless hub with a flap frequency of 1.06/rev was selected for *Caladrius* in order to find balance between control authority and gust sensitivity. All the hub components were sized for both steady and oscillatory loads with an adequate safety factor.

7 Blade Structural Design

The main rotor of *Caladrius* is a five-bladed soft in-plane bearingless rotor composed of composite materials (glass fibre and graphite/epoxy), which are superior to metals in terms of specific strength and fatigue life. The blade structure was designed to achieve the stiffness distribution required to carry the centrifugal forces and both steady and oscillatory flap, lead-lag, and torsional moments. Because it is a dynamic component, it is designed for a safe fatigue life of 5000 hours.

7.1 Structural Design

A specially developed cross-sectional analysis tool was used to calculate the inertial and stiffness properties at specified span locations based on the external blade geometry along the spar, spar and skin thicknesses, and ply orientations. The cross-sectional material distribution was designed to keep the elastic axis at or close to quarter-chord. Leading edge weights were included to ensure that the center of gravity is at the quarter-chord. The spanwise inertial and stiffness properties were then used as inputs to an in-house developed aeromechanics comprehensive analysis code with flap, lag, and torsion degrees of freedom to calculate the natural frequencies of the blade. This entire process was repeated for various design parameters until the desired structural frequencies were achieved across the entire range of operational rotor speeds.

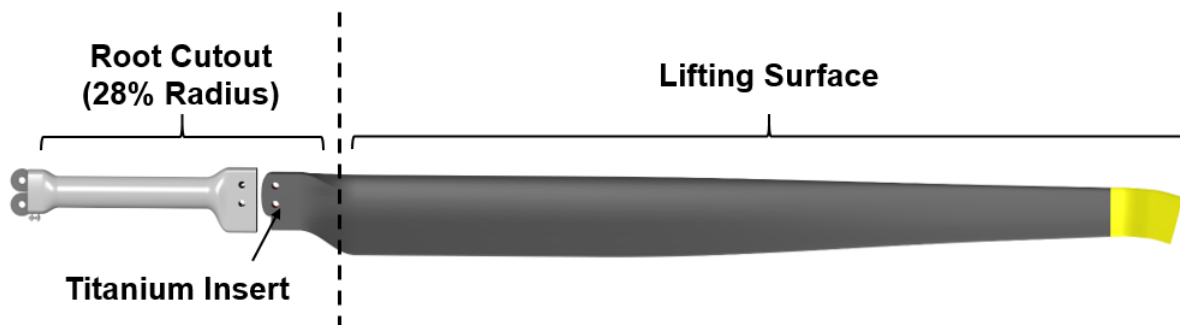


FIGURE 7.1: Primary sections of the main rotor

Figure 7.1 shows the primary structural sections of the rotor blade. The flexbeam surrounded by torque tube spans the inboard 17% of the radius. The torque tube is connected to the blade at its outboard end using steel bolts which are tapered slightly to help in shear. At this connection point, titanium root insert is used to transfer the centrifugal forces. The inboard 7% of the blade is a smooth transition region, where the spar transitions from wrapping around the root insert to a D-spar. Additional plies of carbon fiber are added in this transition region to facilitate the transfer of centrifugal forces. The primary lifting surface runs from 28% span to the tip. Even though root cutout is somewhat large, the effect on thrust is minimal.

7.2 Internal Blade Structure

The complete internal structure of the blade is shown in Figure 7.2. The primary load carrying member is a D-spar, which is composed of unidirectional T300 graphite/epoxy in a $[0/90/0_2/90/0_2/90]_s$ arrangement. The D-spar was selected due to its simple closed-section geometry that provides high torsional rigidity. The T300 graphite/epoxy material was chosen because of high specific stiffness, long fatigue life, and low thermal expansion coefficient making it robust for a mission with wide range of temperatures. The outer $[\pm 45]$ layers provide torsional stiffness, while the four layers of $[0]$ were intermixed with the $[90]$ plies to reduce the probability of delamination and prevent microcracks from coalescing.

The center of gravity was maintained at 24.9% of the chord through the use of tungsten leading edge weights placed interior of the D-spar. This eliminated pitch-flap flutter and pitch divergence. Rohacell 51 foam is inside the D-spar to maintain the aerodynamic profile of the blade while also preventing chordwise movement of the tungsten mass. A stainless steel strip forms the outer profile of the leading edge, protects the blade from abrasion and erosion [26]. Stainless steel strip was chosen due to its superior properties for rain/snow conditions, which is suitable for our mission. Electro-thermal deicing is provided through an electrically insulated heating element placed underneath the leading edge erosion strip.

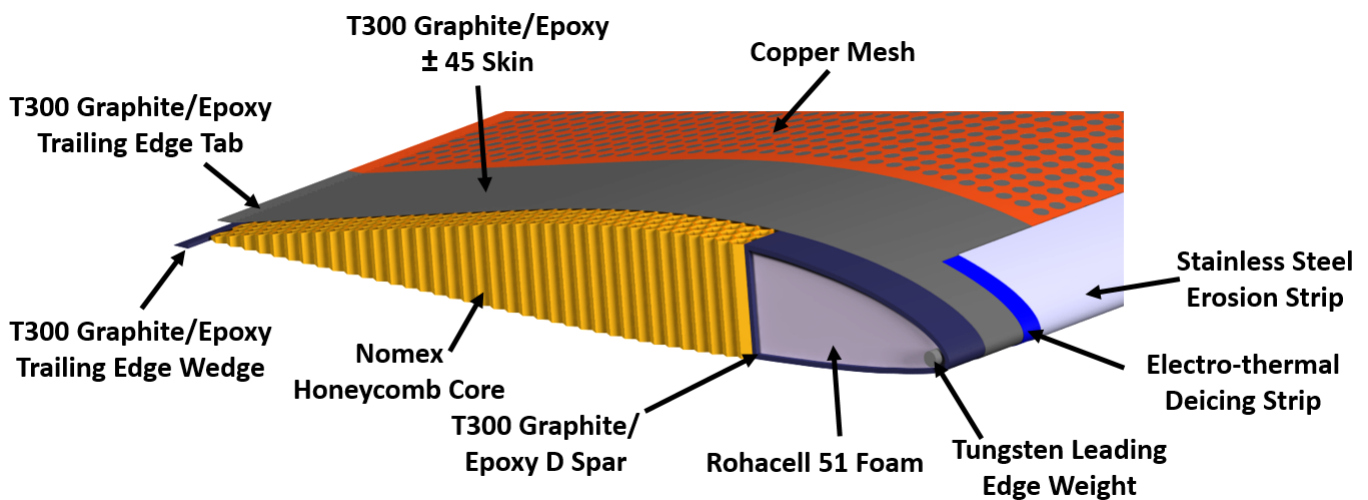


FIGURE 7.2: Internal structure of the blade

The blade skin consists of four balanced $[\pm 45]$ plies of T300 graphite/epoxy, which provides the majority of torsional stiffness and chordwise stiffness. A trailing edge tab of 2% of the chord is formed by the upper and bottom skin surfaces to help prevent trailing edge debonding. A wedge of graphite/epoxy is inserted at the trailing edge to provide additional support against delamination as well as to increase the lag stiffness. The remaining aft section of the blade is filled with a Nomex honeycomb core to maintain the aerodynamic profile of the blade. Nomex honeycomb was selected due to its low weight, excellent thermal stability, and low cost. Lightning strikes may cause delamination in the composite spar due to high heat, and the large current flow. In order to protect these components, the entire blade was wrapped using copper mesh which allows the current to flow spanwise to the root end attachment of the blade. This way, any electrostatic charge build-up can be avoided.

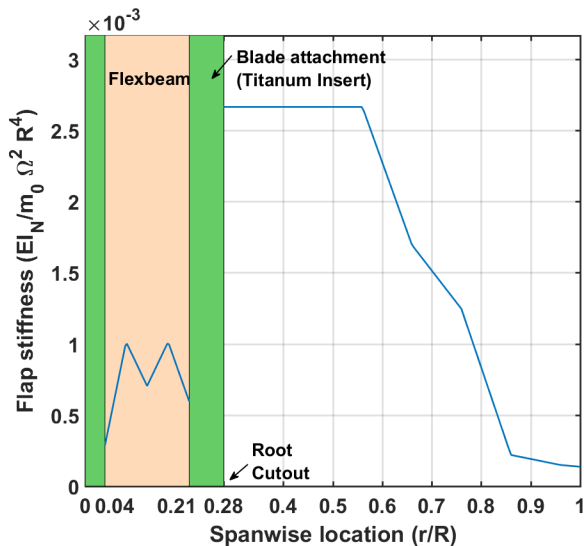
7.3 Blade Manufacturing

The rotor blades are manufactured in two steps. The first step is to create the spar which involves cutting a block of foam to match the internal geometry of the D-spar. Next, small cuts are made into the leading edge of the foam and tungsten weights are placed such that they are flush with the foam. The titanium root insert is placed adjacent to the foam and carbon fiber tape is wrapped around the blade from the tip to root insert and back to the tip. Automated fiber placement is used for better capture of the complex geometry of blade due to twist, taper, sweep and anhedral. Additional plies are added in the inboard 7% of the blade (transition region) to prevent the blade from shearing off. Finally, the spar is cured in a specialized mold that perfectly captures the geometry.

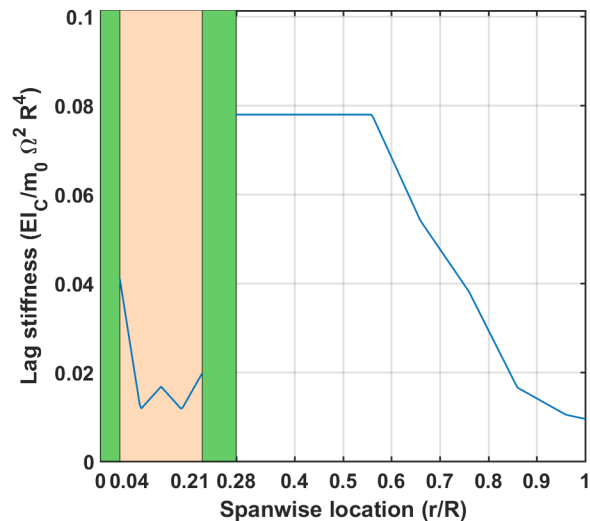
Next, the aerodynamic surface is created. The honeycomb core is cut to match the aerodynamic profile and is pressed up against the back of the spar. The plies for trailing edge wedge are laid up behind the honeycomb using automated fiber placement. This entire assembly is wrapped up using the $[\pm 45]$ plies to maintain the aerodynamic shape of the blade. A electro-thermal pad containing resistors is added at the leading edge for de-icing. The blade mold introduces a small recess in the skin where the stainless erosion strip is added. This entire fabrication is covered using a copper mesh for lightning protection.

7.4 Blade Sectional Properties

Based on the cross-sectional analysis, the weight of an individual blade is 51 kg (112 lb). For the entire system of five blades, this accounts for 257 kg (568 lb). The non-dimensional mass and stiffness distributions of the blade about its elastic axis are shown in Figures 7.3(a) to 7.3(d). The hub connection to the flexbeam begins at 4% span and the blade connection to flexbeam begins at 21% span, therefore the stiffness and mass properties within this region are dominated by the connecting materials. Outboard of the root cutout, the skin, spar, and leading edge weights contribute to the sectional properties and spanwise variations are observed due to the blade taper. The discrete changes in the sectional properties are a result of ply drop-offs from root cutout to blade tip.



(a) Flap stiffness distribution



(b) Lag stiffness distribution



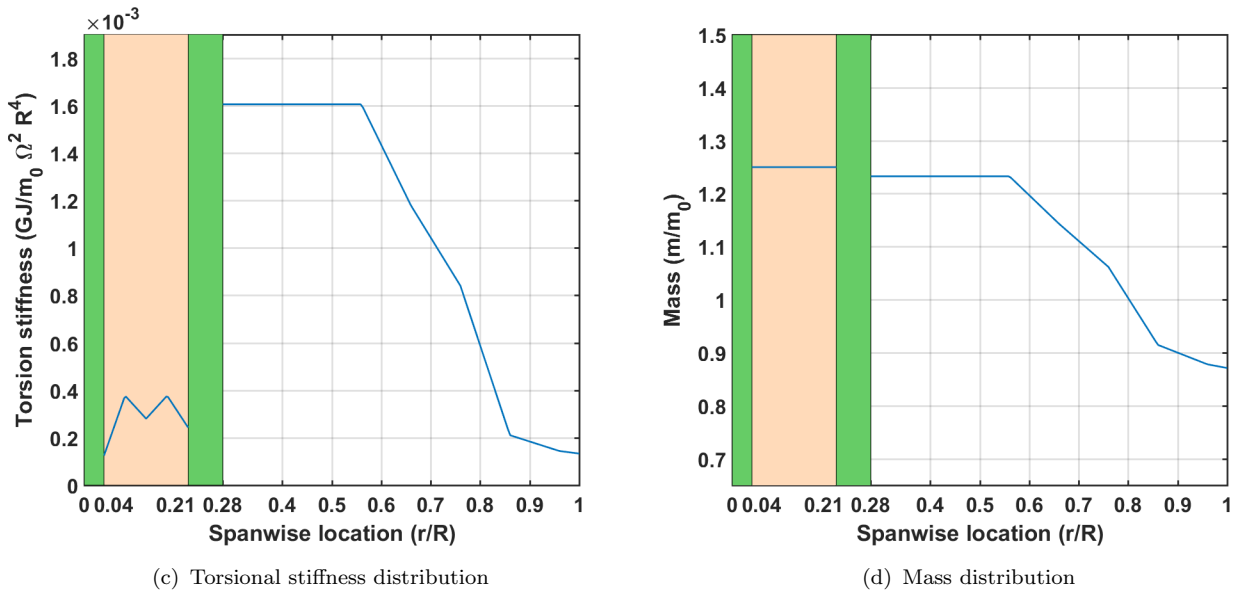
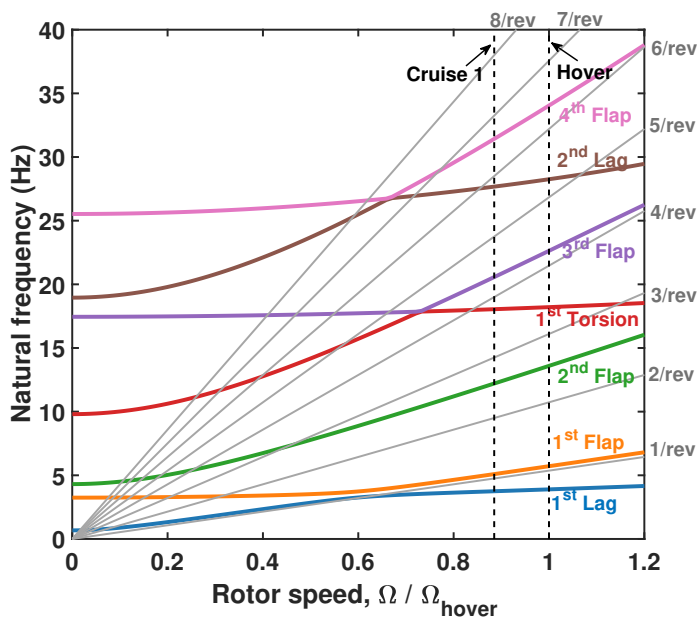


FIGURE 7.3: Main rotor sectional properties

Figure 7.4 shows the fan plot for *Caladrius's* main rotor. The rotor is soft in-plane with a first lag frequency of 0.72/rev. While stiff in-plane rotors alleviate concerns of air and ground resonance, they come at the expense of transmitting higher steady and vibratory hub loads and were therefore not selected. The first flap frequency of the rotor is 1.06/rev. This is a compromise between control authority (requires high hinge offset) and gust sensitivity (requires low hinge offset). The first torsional frequency was targeted for a higher value, which is 3.4/rev for aiding aeroelastic stability. The first six natural frequencies are provided for two operating rotor speeds (hover and cruise) in Table 7.1. These modes are sufficiently far away from the operational rotational speeds over the entire mission, thereby avoiding any resonance crossing.



Mode	Hover Ω (/rev)	Cruise Ω (/rev)
1 st Lag	0.72	0.79
1 st Flap	1.06	1.07
2 nd Flap	2.53	2.57
1 st Torsion	3.4	3.8
3 rd Flap	4.21	4.33
2 nd Lag	5.27	5.82

TABLE 7.1: First six blade frequencies at hover and cruise rotor speeds

FIGURE 7.4: Fan plot showing main rotor frequencies as a function of rotor speed



7.5 Aeroelastic Stability Analysis

Aeroelastic instabilities from pitch-flap and flap-lag coupling were considered during the rotor design by performing an eigen-analysis using the appropriate mass, damping, and stiffness matrices to ensure that the rotor has enough stability margin. Pitch-flap instability is a phenomenon that couple the pitching and flapping motions of the blade and is most effectively managed by placing the blade center of gravity at or in front of the quarter chord. Figure 7.5(a) shows the stability boundaries for pitch divergence and pitch-flap flutter as a function of the C.G. location and torsional frequency. With torsional frequencies of 3.4/rev and 3.8/rev in hover and cruise rotor speeds respectively, along with a C.G. at 24.9% of the chord, *Caladrius's* blades are stable from both pitch divergence and pitch-flap flutter instabilities.

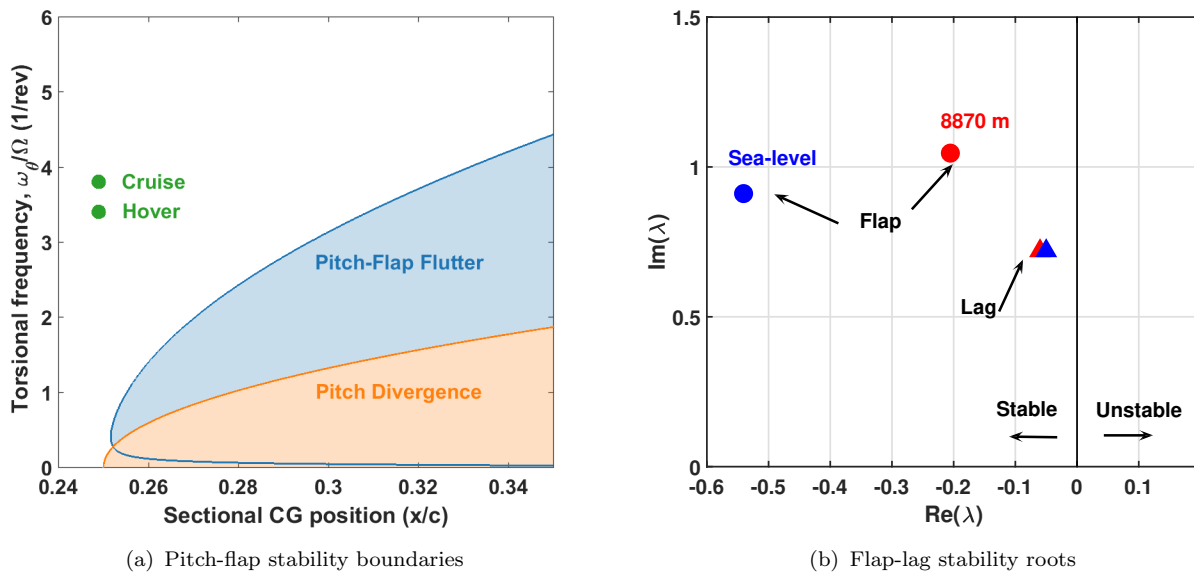


FIGURE 7.5: Divergence and flutter analysis

Flap-lag flutter is an undesirable coupling of the flap and lag modes resulting from perturbation in aerodynamic forces and the limited aerodynamic damping in lag motion. An in-plane elastomeric damper located on the hub provides sufficient damping to prevent this instability. The root loci obtained by an eigenvalue-analysis for flap-lag flutter are plotted in Figure 7.5(b) for sea level and at an altitude of 8870 m (29100 ft). It can be observed that the rotor is stable for flap-lag flutter at both of the altitudes. In addition, it is seen that the flap damping is lower at 8870 m (29100 ft) due to lower Lock number ($\gamma = 3.1$ at 8870 m) than at sea level ($\gamma = 8.2$ at sea level), hence more time is required to dampen out the disturbances.

7.6 Ground and Air Resonance

Ground resonance is an instability that arises from the coupling of the fuselage/landing gear modes with the regressing lag modes of the rotor. This issue is particularly problematic with soft in-plane rotors and when operating on soft landing surfaces. *Caladrius* has a soft in-plane rotor, which makes ground resonance an important consideration and a design challenge especially for a possible snow landing condition. Figure 7.6 shows the coupled ground resonance results for *Caladrius's* 5-bladed rotor, from which it can be seen that the body modes and lag modes are sufficiently separated in the operating range of *Caladrius*.



The instability occurs at a rotor rotational speed of 44.5 rad/s (425 rpm), caused by coalescence of rotor and body modes. In Figure 7.7(a), the damping ratio of this unstable mode for ground resonance is presented. The damping ratio of 0.02 shows that a lead-lag damper is required to stabilize this instability. Even though *Caladrius* is free from ground resonance in its operating range, Deutsch stability criteria [18] was used to obtain lead-lag damper requirements. Since the mission involves operation of the helicopter at different types of terrains such as concrete, snow, rock, grainy soil etc., the landing-gear damping(coulomb friction of the terrain) would differ. Table 7.2 shows the lead-lag damper requirement (% of critical damping) obtained using Deutsch criteria for different terrain conditions. The elastomeric dampers used on *Caladrius*'s bearingless hub have a relatively large damping ratio of 0.11 and therefore only require a small amount of support damping to remain stable from ground resonance at all terrains.

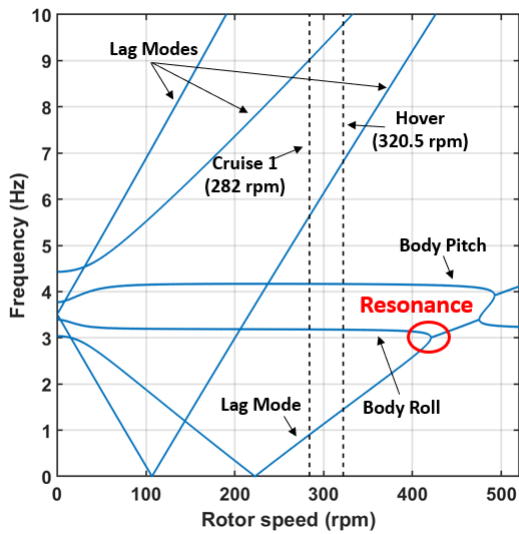
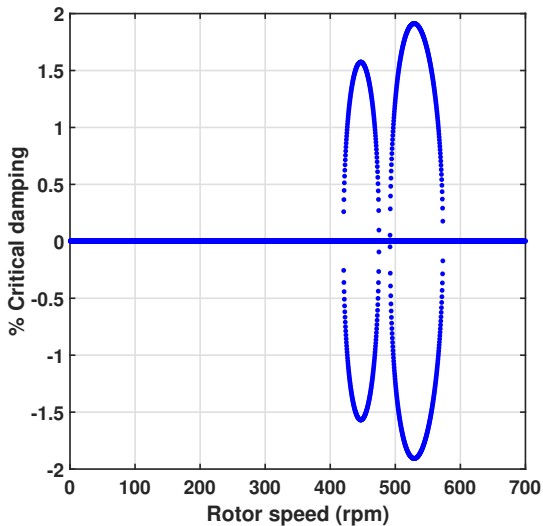


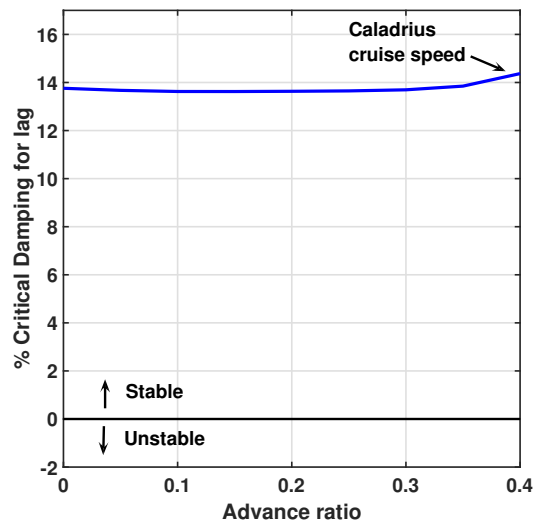
FIGURE 7.6: Stability analysis of ground resonance for *Caladrius*

Terrain Type	Landing gear Damping	Lead-Lag Damper
Concrete	0.05	0.02
Semi Prepared	0.03	0.04
Grass	0.03	0.04
Snow	0.01	0.1

TABLE 7.2: Damping requirements for different terrains



(a) Damping ratio of unstable mode for ground resonance



(b) Damping ratio of lag mode for air resonance

FIGURE 7.7: Damping ratio of the modes in ground and air resonance



Air resonance is an airborne phenomenon where flap and lag modes interact with the fuselage pitch and roll modes and create limit cycle instabilities. They are common for bearingless and hingeless rotors with a first flap frequency, $\nu_\beta > 1.08/\text{rev}$ which are designed for high maneuverability. In air resonance, the regressive lag mode coalesces with flap coupled gyroscopic nutation mode, causing the instability in the lag mode. Even though *Caladrius* has a lower flap frequency, analysis was performed to verify that the in-plane mode has a positive damping. The damping shown in Figure 7.7(b) includes elastomeric lag dampers, thereby augmenting the stability of the lag modes.

7.7 Stress Assessment

To substantiate the design of the main rotor blade and flexbeam, a high-fidelity analysis tool (X3D) was used. The main aim of this analysis was to capture the stress concentrations in the transition region of the blade, particularly the blade-flexbeam attachment. The main load transfer at this junction is the centrifugal force, so a hover test case was chosen due to the higher rotor speed.

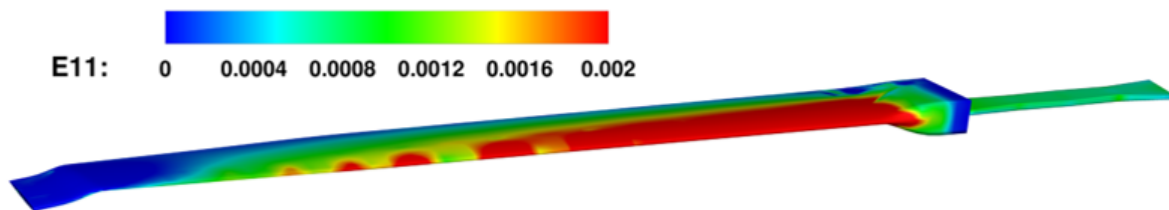
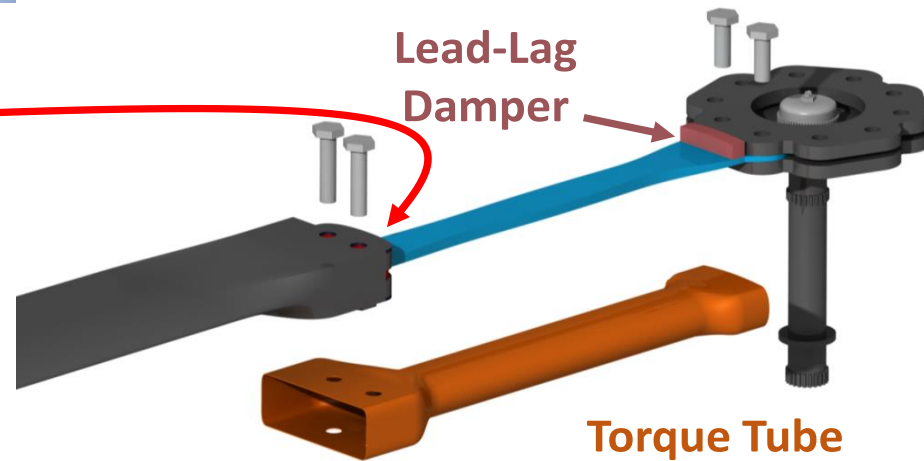
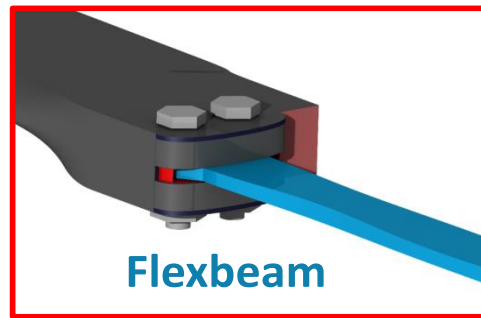


FIGURE 7.8: Strain analysis for main rotor blade using X3D

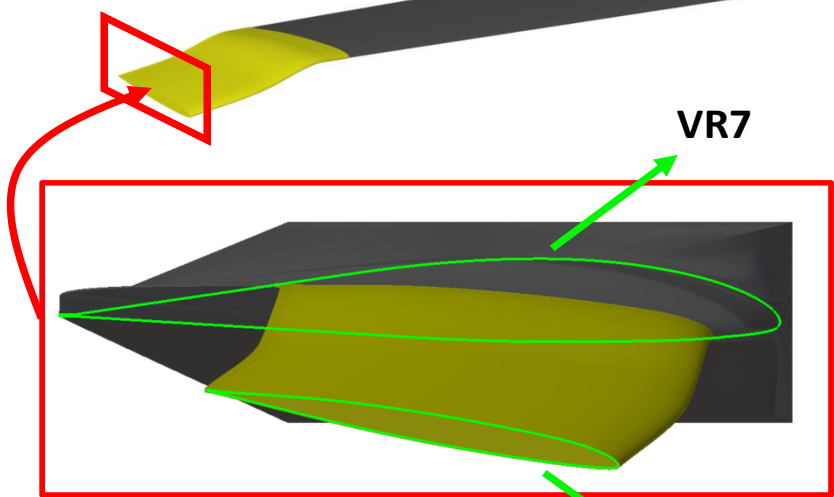
Figure 7.8 shows the strain distribution along the span of the blade during hover. It is seen that the maximum strain is about $2000 \mu\epsilon$, which gives a factor of safety of 1.5 for T300 graphite/epoxy. As expected, the maximum strain occurs inboard near the transition region. Adding additional plies in the transition region reduces the strain, hence lowering the risk of delamination.

To summarize, the main rotor blade of *Caladrius* was designed to achieve the targeted frequencies and to be free from all aeroelastic instabilities. A high-fidelity analysis was also performed to verify and refine the design.

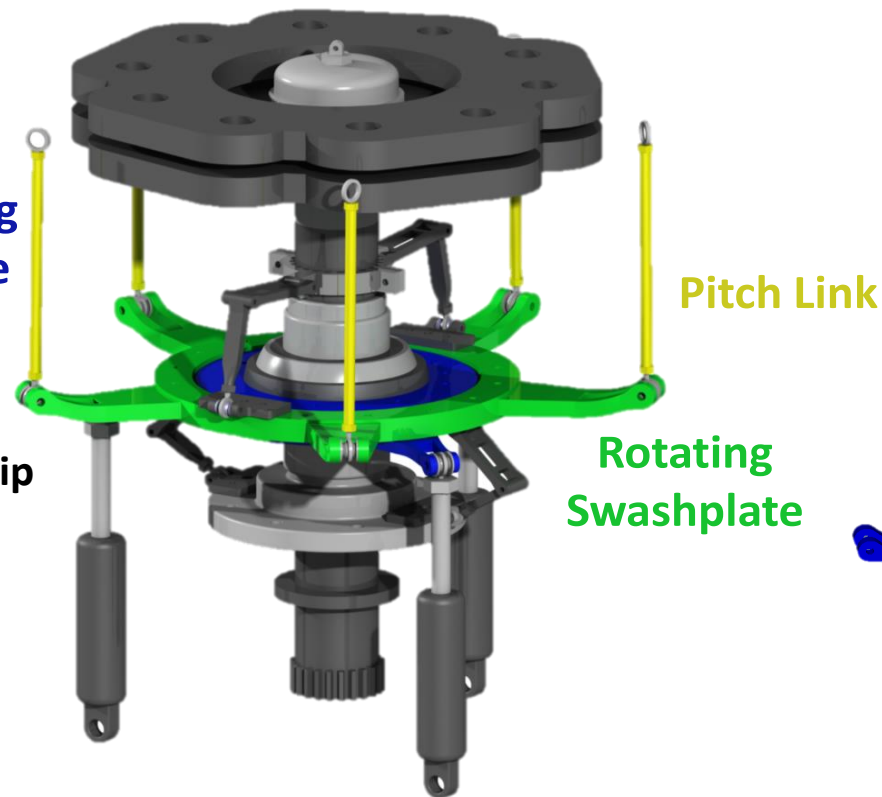
Main Rotor Assembly



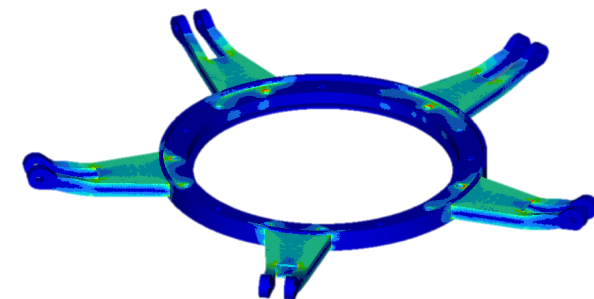
- Flap frequency: 1.06/rev to find the balance between high control power and high gust tolerance
- Soft in-plane
- Clean, robust, low drag profile hub
- Low part count
- Protected from snow and debris



- -6° bilinear twist
- Bilinear taper
- Swept, anhedral, thin tip



Rotating Swashplate



Sized for high control loads due to special airfoils



8 Tail Rotor

Given the uniqueness of the mission, *Caladrius's* tail rotor most important design drivers are: avoidance of loss of tail rotor effectiveness (LTE), high power margin, and severe cross wind/gust tolerance. The design process resulted in a 4-bladed tail rotor with twisted blades, and this process is discussed in this chapter.

8.1 Sizing

The configuration selection process found that the most suitable configuration to complete the mission was the single main rotor with a conventional tail rotor. For the tail rotor design, the parameters analyzed were: diameter, number of blades, aspect ratio, solidity, blade loading, tip speed, and mounting location with relation to the main rotor. It is desirable to design for the most demanding and restrictive flight conditions. During hover, the tail rotor is the sole source of anti-torque for yaw control. In forward flight, both the tail rotor and the vertical tail contribute to produce the anti-torque. Therefore, the tail rotor was sized for hover. The RFP states that *Caladrius* must hover for 30 min at high altitude; this is the condition used for the present analysis. Additionally, it was ensured that the blade tip does not experience drag divergence in forward flight. The power loading of the main rotor is 0.203 kW/kg (0.123 lb/hp). The tail rotor power can be translated into weight using this value, in order to quantify the advantage of lower power consumption. For example, if a specific tail rotor design that has a 2% decrease in the tail rotor power to main rotor power ratio, it would result in 65 kg (143 lb) of extra payload weight.

8.1.1 Diameter

For all the tail rotor diameters analyzed, the thrust was set to the required anti-torque during hover at 8870 m (29100 ft). This thrust accounts for the drag caused by the vertical tail in crosswinds up to 74 km/h (40 knots). Additionally, the condition of wind hitting from 270° azimuthth, can potentially lead to loss of tail rotor effectiveness (LTE) [27] due to the rotor entering the Vortex Ring State (VRS). The onset of VRS depends on the tail rotor inflow. With the anti-torque requirements setting the thrust, for a given tip speed, the tail rotor diameter sets the rotor inflow velocity [15]. Table 8.1 lists the maximum wind allowable before pushing the tail rotor into the Vortex Ring State for tail rotor diameters from 17.4% to 22.5% of the main rotor diameter. As the tail rotor diameter increases, the maximum gust velocity before VRS onset decreases. To generate equal thrust levels, a smaller diameter rotor must have a higher inflow velocity, and therefore delays the onset of VRS to larger gust levels. Smaller tail rotors would be less susceptible to loss of tail rotor effectiveness, but there are other considerations, such as efficiency and power consumption. Because the mission requires a 30 minute hover at extremely high altitude, it is especially important to design an efficient tail rotor. The power consumed for each tail rotor in high altitude hover is shown in Figure 8.1. As the rotor diameter increases, the power consumption decreases, therefore larger tail rotor diameter is beneficial from a power standpoint. Additionally, a smaller tail rotor would result in a higher blade loading coefficient (C_T/σ) for a given dimensional thrust value, which means the tail rotor would have to operate with a smaller stall margin. With these considerations, *Caladrius's* tail rotor diameter was chosen to be 2.8 m (9.2 ft). This was chosen so that there would be a 10% margin on gust tolerance for loss of tail rotor effectiveness over the requirements in the RFP, up to 81.4 km/h (44 knots) side wind at 8870 m (29100 ft) and 50 km/h (27 knots) wind at 1402 m (4600 ft). A smaller diameter was not desirable because of the associated increase in power consumption,



for example, the chosen diameter gives an extra 70 kg (154 lb) payload capability compared to a tail rotor of 2.4 m (7.9 ft).

TABLE 8.1: Maximum steady side wind in hover to avoid VRS

Diameter (m)	Steady wind at 8870 m	Steady wind at 1402 m
3.1 (22.5% of R_{mr})	74.0 km/h (40 knots)	44.4 km/h (24 knots)
2.8 (20.3% of R_{mr})	81.4 km/h (44 knots)	50.0 km/h (27 knots)
2.6 (18.9% of R_{mr})	88.8 km/h (48 knots)	53.7 km/h (29 knots)
2.4 (17.4% of R_{mr})	96.2 km/h (52 knots)	58.3 km/h (32 knots)

The tail rotor size was also compared to historical trends using Equation 8.1 [28]. The trends suggest a tail rotor diameter of 2.36 m (7.7 ft), 17.18% of the main rotor diameter. However this tail rotor would consume higher power as shown in Figure 8.1.

$$\frac{D_{tr}}{D_{mr}} = \frac{1}{7.15 - (0.27)DL_{mr}} \quad (8.1)$$

8.1.2 Number of Blades

Tail rotors with 2, 3, 4 and 5 blades were all compared with constant solidity. Figure 8.1 shows that the difference in power consumption was significant between 2, 3, and 4-bladed rotors. However, the difference was less between 4 and 5-bladed rotors. For the chosen diameter of 2.8 m (9.2 ft), in terms of payload capability, the 5-bladed rotor has 2 kg (4.4 lb), 7 kg (15.4 lb), and 20 kg (44 lb) extra payload compared to 4, 3, and 2-bladed rotors respectively. Hence, a 5-bladed rotor would appear to maximize payload, but the added weight of the additional blade and hub structure compared to a 4-bladed rotor more than offsets the power benefits, actually causing a reduction in payload. Therefore, a 4-bladed tail rotor was chosen, for it leads to light hub design while maximizing payload capacity [28].

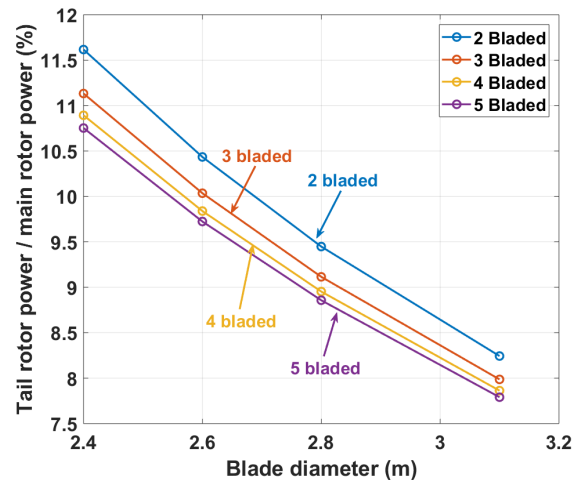


FIGURE 8.1: Ratio of tail rotor power to main rotor power (%) vs. blade diameter

8.1.3 Solidity

With diameter selected by gust tolerance and number of blades determined by power considerations, the tail rotor solidity was selected by blade loading (C_T/σ) considerations. Because the tail rotor thrust was fixed from the required anti-torque and the diameter is already decided, solidity directly dictates blade loading, C_T/σ . Low blade loading, which means high solidity, is desirable to increase the stall margin, which is of special importance in extremely gusty environments. Contrarily, high solidity results in high profile drag, which is not desirable. The aspect ratio was computed (Figure 8.2) directly from the rotor diameter and solidity.



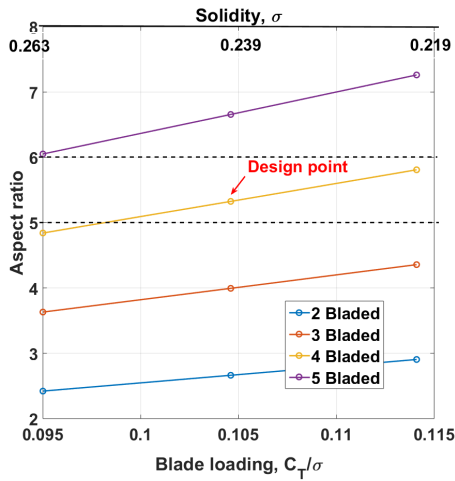


FIGURE 8.2: Aspect ratio at different C_T/σ

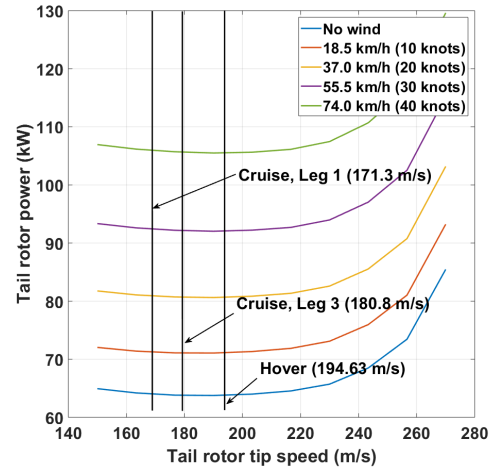


FIGURE 8.3: Tail rotor power variation with tip speed at hover

The expected range of solidity for *Caladrius's* tail rotor is higher compared to most helicopters, with a range of 0.13 to 0.18 [29]. This is because *Caladrius's* solidity is kept high to minimize blade loading to provide significant stall margin for maneuvers. Increasing the solidity to extreme values reduces the rotor aspect ratio which results in adverse 3-D/radial flow effects and very thick blades, which decreases aerodynamic efficiency. The aspect ratio of *Caladrius's* tail rotor was therefore not permitted to fall below 5. As shown in Figure 8.2, the highest solidity design point with an aspect ratio over 5 was chosen; an aspect ratio of 5.32 and solidity of 0.239. The resulting blade loading for the high altitude hover for this design point is 0.1041, which provides a significant stall margin.

8.1.4 Tip Speed

Tail rotor tip speed should be low to minimize noise levels. On the other hand, high tip speed minimizes weight, for higher speeds mean lower torque, and hence a lighter drive shaft [28]. Additionally, power consumption is of utmost importance for long duration hover at extremely high altitude. Hence, tail rotor power for different tip speeds was studied, and the results are shown in Figure 8.3. Each line corresponds to a different wind speed; all wind is from 90° azimuth, because this condition requires maximum tail rotor power. It can be seen that the power required is nearly constant up to 220 m/s (722 ft/s) and this trend is true for all wind speeds. Because there is negligible impact on power, the tip speed was chosen to ensure the tip Mach number during cruise does not exceed the drag divergence Mach number. Therefore, for the selected airfoil, discussed in Section 8.2.1, the hover tip speed of 194.63 m/s (638.55 ft/s) was selected. The tail rotor speed reduction ratio from hover to cruise is the same as the main rotor, as the gear boxes are mechanically linked through a drive shaft.

8.1.5 Location, Configuration, and Direction of Rotation

The mounting location of the tail rotor was decided based on the moment arm of the tail rotor from the center of gravity to provide the best anti-torque. A tip clearance between main and tail rotor of 0.1 m (0.33 ft) was ensured for safety, and therefore the horizontal distance between the main rotor and tail rotor is 8.39 m (27.5 ft) from the diameters of both rotors.



TABLE 8.2: Tail rotor properties

Parameter	Value
Diameter	2.80 m (9.19 ft)
Chord	0.27 m (0.89 ft)
Solidity, σ	0.239
Moment arm, l_T	8.39 m (27.53 ft)
Hover rotor speed	139 rad/s (1328 rpm)
Hover tip speed	194.63 m/s (638.55 ft/s)
Twist	-20° linear
Airfoil	RC510

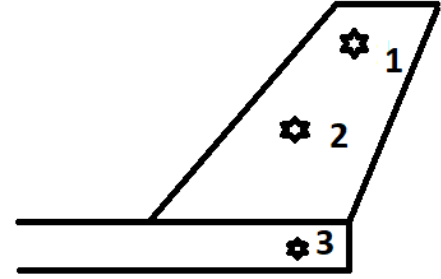


FIGURE 8.4: Tail rotor vertical positioning

Three possible vertical positions for the tail rotor hub were considered, which are all shown in Figure 8.4. Position 1 was chosen for *Caladrius* for three main reasons: (1) higher positions are safer for ground crew, (2) the trim roll angle in hover was found to be lower with the tail rotor in position 1, which is crucial for precise hover during rescue operations, and (3) the area of tail rotor in the main rotor wake in cruise is minimized by placing the tail rotor as high as possible, this is confirmed by the CFD wake picture shown in Figure 9.4. It is beneficial to minimize the effect of main rotor wake on the tail rotor to minimize interactional aerodynamic effects and have clean inflow for the most efficient operation. Because of these three reasons, position 1 was chosen, but this design decision means the vertical tail spar needed to be structurally strengthened compared to position 2 or 3. This small disadvantage does not outweigh the other benefits that lead to fast and safe emergency rescue operations.

Caladrius's tail rotor was chosen as a pusher because the power consumption is lower compared to a tractor type. The reason is that the tail rotor wake is blocked by the vertical tail in the later configuration [29]. However, the pusher configuration is more susceptible to tail rotor blades hitting the vertical tail during forward flight due to flapping. Therefore, the flapping stiffness, the separation between hub, attachment point on the vertical tail, and a δ_3 angle for pitch-flap coupling (Section 8.3) were chosen carefully.

The direction of rotation was chosen as “aft-at-the-top” because the advancing side moving into the main rotor wake provides a better aerodynamic performance than the “aft-at-the-bottom” case [28].

8.2 Aerodynamic Design

8.2.1 Airfoil Selection

Unlike the main rotor, a single airfoil was decided for *Caladrius's* tail rotor primarily because of simplicity and low cost of manufacturing. Keeping the tip Mach number same as main rotor (0.85) would lead to the use of thin supercritical airfoils which might cause structural difficulties. As a result, it was decided to have a lower tip Mach number (a maximum

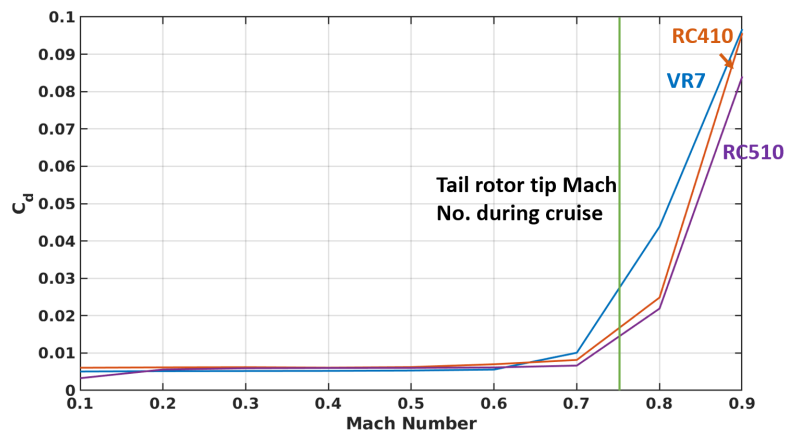


FIGURE 8.5: Tail rotor airfoil selection



of 0.75 in cruise) for the tail rotor. Figure 5.3 shows that RC510 has good L/D and Figure 8.5 shows that it has better drag divergence characteristic than VR7. Hence, RC510 was chosen as the tail rotor airfoil.

8.2.2 Blade Geometry

Figure 8.6 shows the variation in tail rotor power consumption in hover and axial climb for different values of blade twists. It can be seen that a -30° blade twist is ideal. However, a highly twisted blade has poor axial descent performance and might lead to tail rotor stall and loss of tail rotor effectiveness in high gust conditions. A decrease in twist to -20° results in a good stall margin (4° at root) with only marginal increase in power of about 1.48%. Hence, -20° was chosen as the twist for the tail rotor blade. The blades do not have taper primarily because the associated manufacturing complexities and costs do not justify the marginal gain in performance. The design parameters of *Caladrius's* tail rotor is listed in Table 8.2.

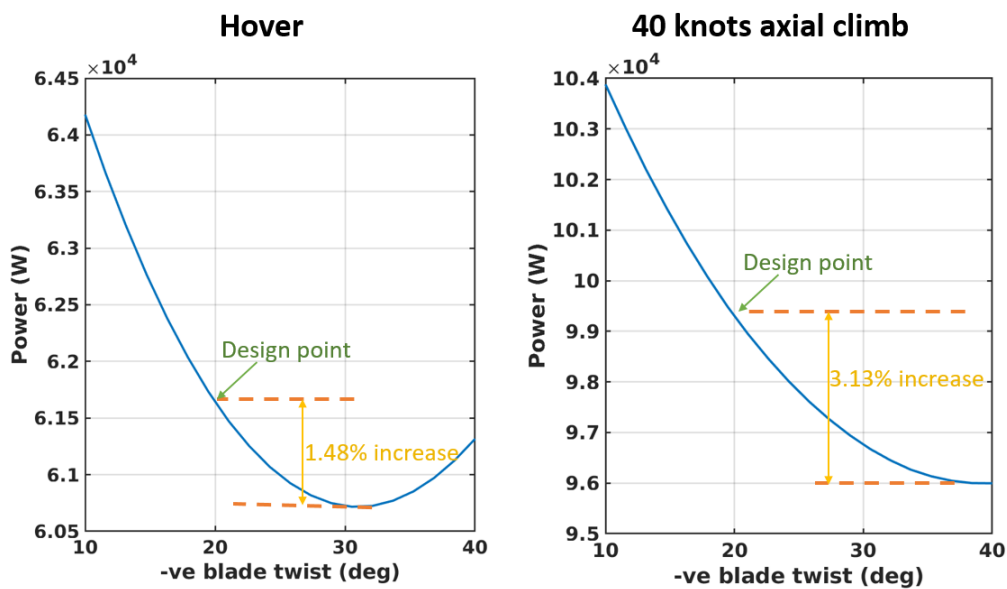


FIGURE 8.6: Power required by tail rotor as a function of twist

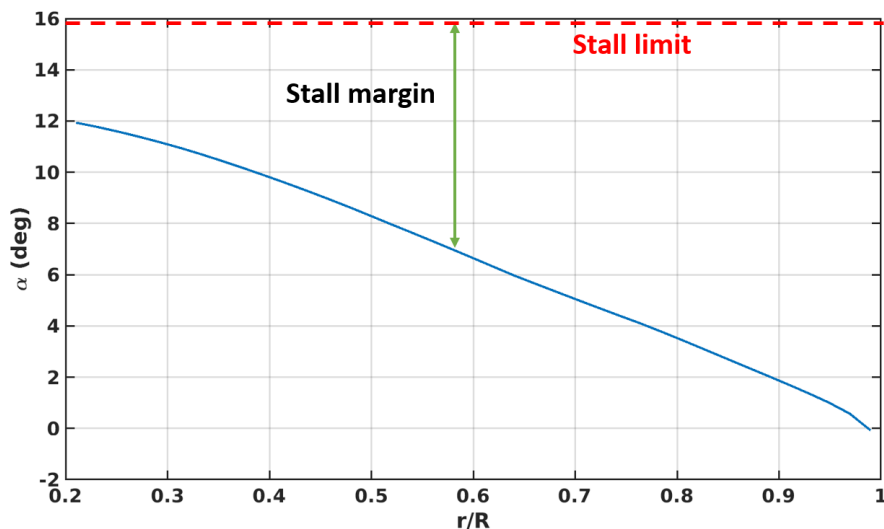


FIGURE 8.7: Angle of attack of different tail rotor blade sections at 40 knots steady side wind



8.3 Structural Design

Caladrius's tail rotor is a 4-bladed stiff in-plane bearingless rotor composed of composite materials. A stiff in-plane rotor was chosen to eliminate the damper requirements and a bearingless construction for a cleaner configuration with low part count and shielded from extreme weather conditions.

8.3.1 Hub Design

Spider Actuator

Only collective control is needed for the tail rotor, so a spider assembly was chosen. A conventional swashplate was not considered due to the weight penalty associated with additional structure and actuators. A hydraulic actuator is used to control the tail rotor collective and is located in the vertical tail. The actuator rod runs through the rotating hub to the spider.

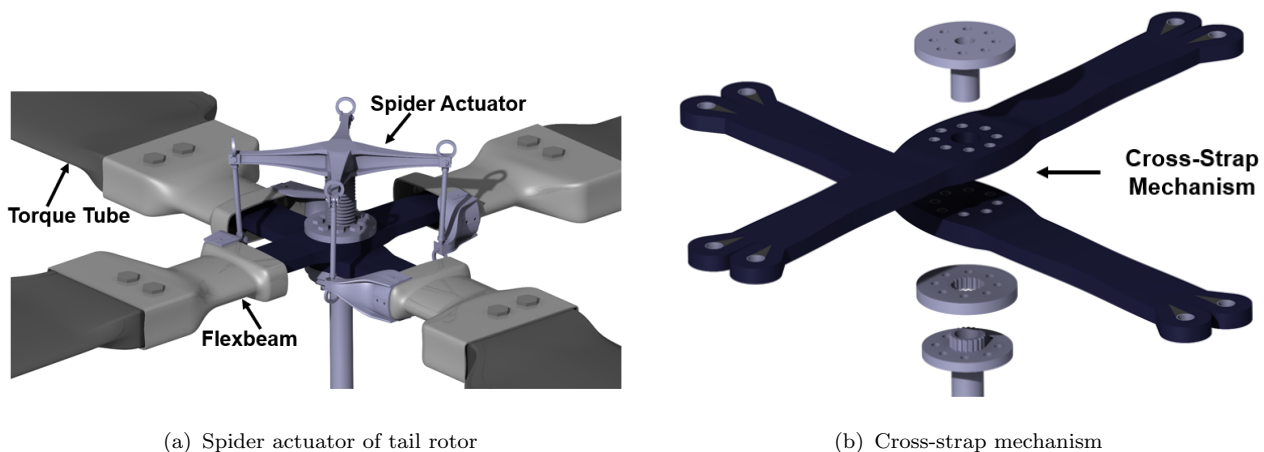


FIGURE 8.8: Tail rotor hub components

Hub Attachments

Caladrius's tail rotor contains many of the same components as that of main rotor with a few subtle differences. A cross-strap type mechanism (Figure 8.8(b)) was chosen for the flexbeams to reduce overall weight and mechanical complexity [30]. In this configuration, the flexbeams for two opposite rotors are connected and bolted straight to the hub. Although the shear force on the flexbeam at the bolts will be minimized due to the centrifugal forces balancing, extra $[\pm 45]$ plies were added in the center to increase its shear strength. The flexbeam was tailored to achieve the desired frequencies for the rotor. E-glass fibre was used for the flexbeam (same as the main rotor).

A torque tube is utilized to carry the pitching moments of the blade. The torque tube for the tail rotor has an elliptical cross-section to provide low drag. A graphite/epoxy composite was chosen for the torque tube due to a high stiffness to weight ratio. Just like for the main rotor, the pitch horn is attached directly to the torque tube. A δ_3 coupling of 25° is provided to minimize blade flapping without increasing the hub loads.

A conventional mast retaining nut cannot be used for the tail rotor due to the actuator rod for the spider. Instead, a flange is placed along the tail rotor shaft and the flexbeams bolt directly to the flange. A steel cap was placed between the bolt head and the flexbeam to help distribute the compressive loads on the flexbeam.

8.3.2 Blade Design

The tail rotor blade has a D-spar made of T300 graphite/epoxy. Most of the components used on main rotor blades like deicing strip, erosion strip, leading-edge weights were also used on the tail rotor blades to protect from the extreme weather at the high summit. A similar design methodology as that of main rotor was followed for achieving the target frequencies of tail rotor. Figure 8.3.2 shows the fanplot for the tail rotor and Table 8.3 provides the first four frequencies at hover and cruise rotor speeds. The first flap and lag frequencies are 1.12/rev and 1.4/rev, respectively. A high flap frequency reduces the chances of tail rotor striking the vertical tail. A high torsional frequency of around 4.21/rev prevents aeroelastic instabilities.

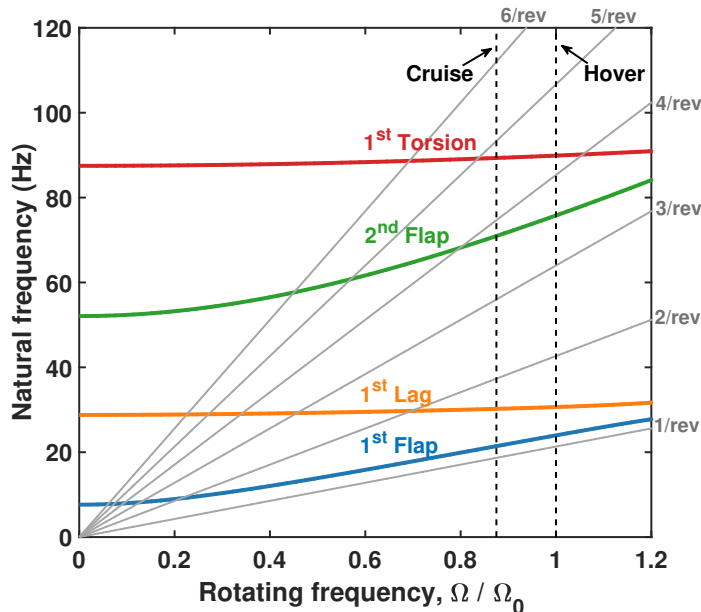


FIGURE 8.9: Fan plot showing tail rotor frequencies vs. rotor speed

Mode	Hover Ω (/rev)	Cruise Ω (/rev)
1 st Flap	1.12	1.14
1 st Lag	1.43	1.6
2 nd Flap	3.55	3.8
1 st Torsion	4.21	4.78

TABLE 8.3: First four blade frequencies at hover and cruise rotor speeds

Caladrius's tail rotor plays a key role in achieving the critical requirement of high hover efficiency and gust tolerance for the mission. By designing highly twisted four-bladed blades, the tail rotor power consumption was minimized and it was ensured that it is safe from LTE and VRS in the winds up to 74 km/h (40 knots) at high altitude.

9 Empennage Design

9.1 Vertical Tail

Even though tail rotors are generally adequate for directional stability, a vertical tail can help streamline the tail rotor support, supplement direction stability, unload the tail rotor in forward flight by providing additional anti-torque force, and allow emergency landing in case of tail rotor failure [29]. Most modern helicopters are therefore equipped with a vertical tail. Off-loading the tail rotor in forward flight helps reduce dynamic loads on tail rotor hub and pitch links and thus increases the fatigue life of hub and mechanical linkages [28].

The size of the vertical tail is dictated by two contradictory factors. A large vertical tail is advantageous in forward flight but introduces blockage effect and responds adversely to high winds in hover. The current mission involves forward flight in legs 1 and 3 at different altitudes



and speeds. In order to unload the tail rotor completely in these flight segments, the required vertical tail area is 1.4 m^2 (15.1 ft^2) and 1.2 m^2 (12.9 ft^2), respectively. If the higher value was chosen, it would produce anti-torque force during forward flight in leg 3 that would necessitate some side slip angle as the vertical tail incidence is kept fixed. In order to avoid this side slip angle and to minimize the tail rotor blockage, the vertical tail area was selected 1.2 m^2 (12.9 ft^2). Because the airflow on the vertical tail is not clean due to the wakes from main rotor and fuselage, dynamic pressure was assumed 70% of the freestream dynamic pressure in this analysis. In Reference [29], vertical tail planform area is plotted against the tail rotor solidity for some helicopters and it follows a linear trend. The area of *Caladrius's* vertical tail would be about 3.25 m^2 (35 ft^2), if it were to follow this statistical trend. However, this trend is deliberately avoided to account for severe winds in hover at high altitude.

To provide enough anti-torque with a small surface area, a highly cambered airfoil, NACA4415 at an incidence of 5° , was chosen initially. However, the thickness of the vertical tail was not enough to enclose the tail rotor gear box drive system. Therefore, NACA4418 airfoil was finally selected, although it has slightly smaller cl/cd . The final properties of the vertical tail are listed in Table 9.1. The aspect ratio was chosen as 2.7; however, the effective aspect ratio is higher due to the presence of horizontal tail and tail rotor hub (endplating). This was calculated using Equation 9.1 from Reference [31]. The geometric parameters K_H (factor relating relative size of horizontal and vertical tails), $A.R.V/A.R.V+B$ (ratio of the aspect ratio of the tail alone to that of the tail in presence of fuselage) and $A.R.V+B+H/A.R.V+B$ (ratio of the aspect ratio of the tail in the presence of body to that of the tail in presence of body and horizontal tail) quantifies the endplating effect and the effective aspect ratio was found to be 6.94. Hence, the flat plate area of the vertical tail was reduced from 0.21 to 0.08 m^2 . The trailing edge of the vertical tail has been clipped to reduce the strength of the tip vortices, which can form if the wind hits the tail from around 45 deg azimuthal direction. This blunt trailing edge, thus, prevents the loss of tail rotor effectiveness.

$$A.R.V_{eff} = A.R.V_{geo} \left[\left(\frac{A.R.V}{A.R.V+B} \right) \left[1 + K_H \left(\frac{A.R.V+B+H}{A.R.V+B} \right) \right] \right] \quad (9.1)$$

Thrust and the required power sharing between tail rotor and vertical tail to provide the anti-torque at different cruise speeds was obtained for leg 3 cruise where the tail rotor is completely unloaded at 283 km/h (153 knots) as shown in Figure 9.1(a). Because the vertical tail lift is proportional to the square of the cruise speed, at lower speeds the tail rotor was found to be highly loaded and it gets unloaded to 50% thrust only at 222 km/h (120 knots). Even though the tail rotor is completely unloaded at 283 km/h (153 knots), 12 kW (16 hp) power is still required to overcome the profile drag of the tail rotor as shown in Figure 9.1(b). However, the total power required for anti-torque reduced to half compared to tail rotor only design. Power required for vertical tail is the power to overcome the drag from vertical tail consisting of its profile drag, induced drag and the interference drag due to the tail rotor.

TABLE 9.1: Vertical tail properties

Parameter	Value
Area	1.2 m^2 (12.9 ft^2)
Span	1.80 m (5.9 ft)
Root chord	0.89 m (2.92 ft)
Tip chord	0.44 m (1.44 ft)
Moment arm, l_v	8.0 m (26.2 ft)
Aspect ratio	2.7
Airfoil	NACA4418
Incidence	5°



9.2 Horizontal Tail

The relative merits of installing the horizontal tail at three different locations (Figure 9.2) is compared in Table 9.2. In case 1, similar to UH-1H and H145, the horizontal tail is attached to the tail boom. Being closer to the main rotor hub, this design would need higher planform area to provide the pitch stability in cruise compared to the other two designs. Furthermore, being under the main rotor wake during hover, there would be minimum pitch variation during transition from hover to climb, however the download drag imposed during 30 minute hover would make this design high power consuming and hence not desired.

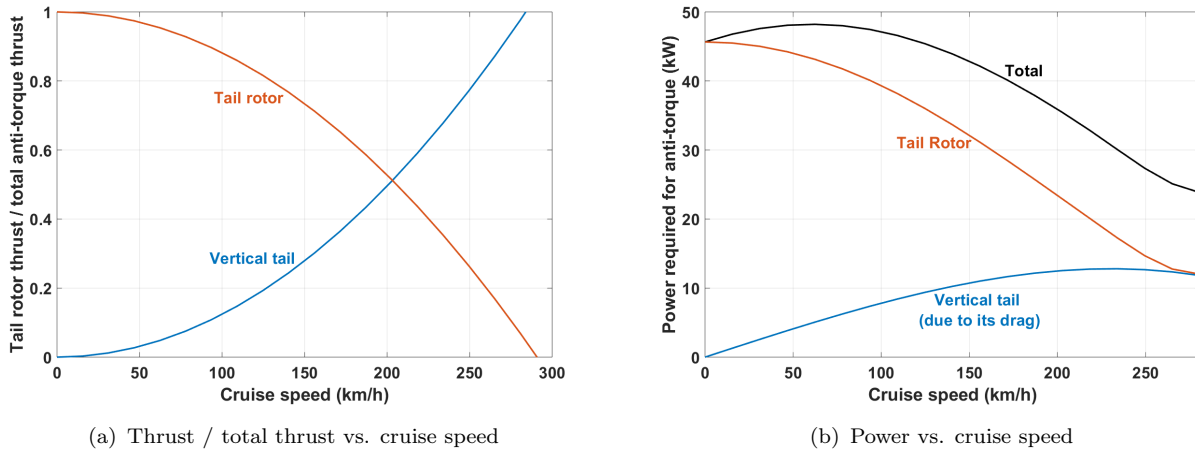


FIGURE 9.1: Thrust and power sharing between anti-torque devices vs cruise speed

TABLE 9.2: Horizontal tail location comparison

	Case 1	Case 2	Case 3
Vertical location from tail boom	same level	above	same level
Longitudinal position from vertical tail	towards the main rotor hub	near vertical tail	near vertical tail
Effect of wake during transition	no sudden change from hover to forward flight	minimum	from hover to forward flight
Planform area	high	low	medium
Download penalty	during hover	none	during climb and forward flight
Structural consideration	high weight	low weight but heavy vertical tail	medium weight

The other two options to install the horizontal tail are marked 2 and 3 in Figure 9.2. Because the tail rotor location coincides with the horizontal tail for case 2, it could only be installed on one side, right side of the vertical tail when seen from rear. This would in fact help balance the rolling moment from the main rotor during forward flight. Due to the bearingless hub design of the main rotor, the rolling moment would be significant and mitigating this with horizontal tail



would reduce the cyclic requirement and thus reduce the vibration in airframe. For case 2, the effect of the main rotor wake on the horizontal tail would also be minimized compared to the other option except perhaps during descent.

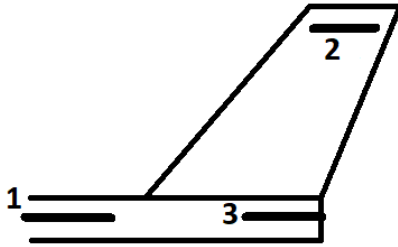


FIGURE 9.2: Horizontal tail positioning

TABLE 9.3: Horizontal tail area for the three cases

Case	l_h	η	S_h
1	6.0 m (19.7 ft)	0.75	3.4 m ² (37 ft ²)
2	7.9 m (25.9 ft)	0.90	2.1 m ² (23 ft ²)
3	7.6 m (24.9 ft)	0.75	2.6 m ² (28 ft ²)

In order to select between cases 2 and 3, further analysis was performed by calculating the planform area required to provide similar equivalent sizing parameter, K_h , defined by Equation 9.2. This parameter represents the ability of the horizontal tail to provide static longitudinal stability. It is a function of η (a factor dependent on vertical location of the horizontal tail), l_h (horizontal tail moment arm), s_h (horizontal tail area), T (main rotor thrust), h (height of the main rotor relative to helicopter’s C.G.) and K_r (a constant dependent on the hub moment from the main rotor). Statistically, $K_h=3$ provides sufficient stability [32], and this value was used here to obtain the horizontal tail area for the three cases as shown in Table 9.3.

$$K_h = \frac{\eta l_h s_h 10^3}{T \cdot h + K_r} \tag{9.2}$$

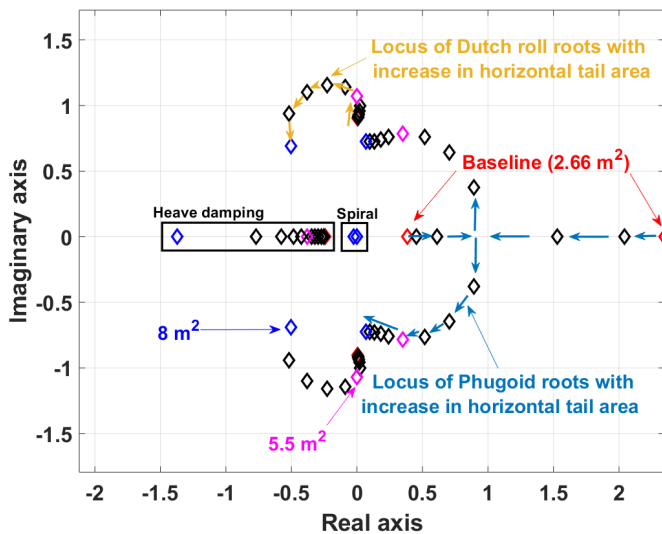


FIGURE 9.3: Effect of horizontal tail on dynamic stability

TABLE 9.4: Horizontal tail properties

Parameter	Value
Area	2.66 m ² (28 ft ²)
Span	3.65 m (12 ft)
Chord	0.73 m (2.4 ft)
Moment arm	7.6 m (25 ft)
Aspect Ratio	5.0
Airfoil	NACA4412 inv
Incidence	2.25° (nose up)

Option 2 is a one sided horizontal tail, so the vertical tail must be heavier. Also, in order to maintain an acceptable aspect ratio of 5, chord for this horizontal tail would be 0.65 m which can not be supported near the tip of the vertical tail. These structural problems could be avoided by going with option 3. It also provides additional ground safety from the tail rotor tip. Moreover,



the endplating discussed in Section 9.1 works most favorably with option 3. Therefore, case 3 was selected for *Caladrius*. There will be sudden change in pitch during transition from hover to climb but this is common to modern helicopters and can be easily managed by the pilots. The complexity involved in the variable pitch or free floating horizontal tail and the fact that these designs can increase the pilot workload meant these options were discarded. A fixed incidence horizontal tail design appear the best option. Table 9.4 shows the final properties of *Caladrius*'s horizontal tail. An inverted NACA4412 was used to provide negative lift in forward flight and a fixed incidence of 2.25° maximizes its effectiveness in cruise.

Horizontal tail plays a key role in providing the longitudinal dynamic stability to the helicopter in cruise. Like many other helicopters (example helicopter in [31]), *Caladrius*'s longitudinal roots (without feedback) were found unstable for the designed horizontal tail area of 2.66 m^2 . The horizontal area was varied and the roots were tracked as shown in Figure 9.3. It was found that the modes came close to imaginary axis for horizontal tail area of 8 m^2 . The dutch roll mode is also modified for tail area greater than 5.5 m^2 and the effect on Phugoid and Dutch roll are switched. Moreover, larger horizontal tail makes the helicopter heavy and more susceptible to vertical gust. Instead, attitude and rate gains were added to augment the stability as discussed in Section 10.3.

CFD analysis of the main rotor, in cruise flight ($\mu = 0.4$), was conducted to analysis the wake structure and its impact on the tail. Figure 9.4 shows an iso-surface of Q-criterion. From this flow field, it can be seen that the strong tip vortex passes through the tip of the vertical tail. This interaction is another strong reason not to place the horizontal stabilizer at location 3, for it could potentially cause issues such as tail buffeting.

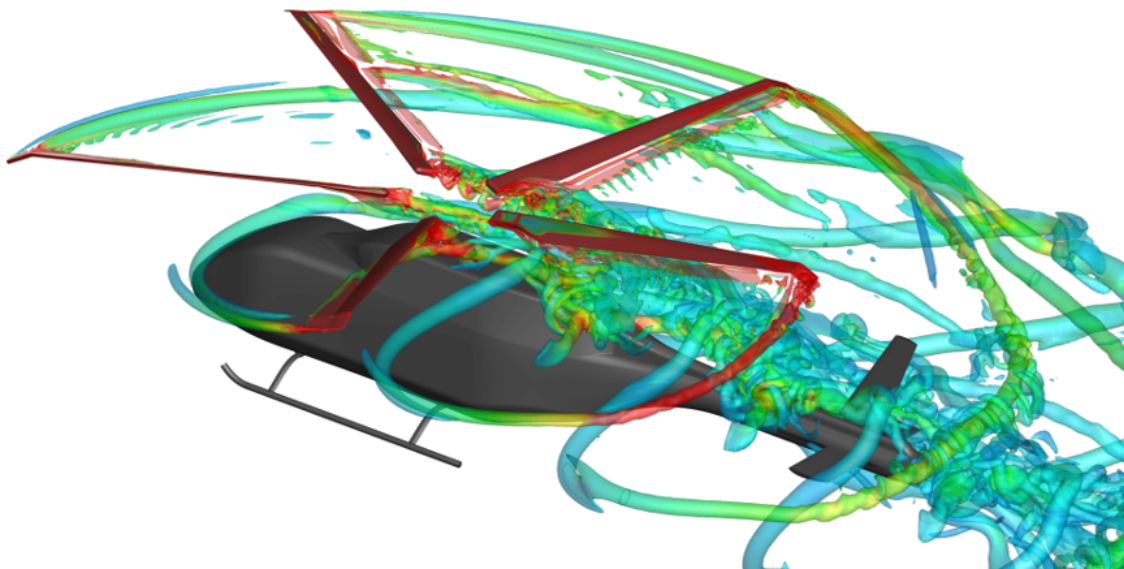


FIGURE 9.4: Main rotor wake for $\mu = 0.4$, $C_T/\sigma = 0.073$ and $\alpha_s = 5.1^\circ$

Large tail boom and high speed winds on the empennage produce a significant moment about the helicopter's C.G.. Therefore, smallest possible empennage were designed without compromising stability to the helicopter using high C_l/C_d airfoils, high aspect ratios and careful positioning.

10 Flight Mechanics and Controls

Caladrius's flight control system was designed to reduce the pilot workload at critical times during the high altitude rescue operation. Additionally, good agility in hover is another feature of *Caladrius* to enhance maneuverability, which helps to stabilize the underslung load, even under strong disturbances. These features were achieved by selecting an explicit model following flight control system design.

10.1 Flight Dynamics

A linear rigid body flight dynamics was developed consisting of three translational, three rotational and three kinematic relations. These equations in perturbation form about the trim condition is shown in Equation 10.1. The state vector, $\{x\}$, consists of $\{u, v, w, p, q, r, \phi, \theta, \psi\}$.

$$\{\dot{x}\} = [A]\{x\} + [B]\{u\} \quad (10.1)$$

The A and B matrices contain the stability and the control derivatives respectively. The control vector $\{u\}$, in this formulation, includes the main rotor collective, longitudinal and lateral cyclics, and the tail rotor collective.

10.2 Vehicle Control

Because *Caladrius* is an SMR, it uses conventional rotorcraft controls. Main rotor swashplate inputs include collective for thrust, longitudinal cyclic and lateral cyclic for pitch and roll, and the tail rotor provides yaw control with pedal control. Traditional mechanical linkages provide stick inputs to the swashplate, with control mixing for decoupling lateral and longitudinal response of the vehicle. The range for these control angles have been carefully selected based on all expected flight conditions and additional margin for maneuvers and gusts, are listed in Table 10.1.

TABLE 10.1: Range of control angles

Control angles	Range (deg)
MR collective	-2 to 16
MR longitudinal cyclic	-10 to 16
MR lateral cyclic	-8 to 8
TR collective	-10 to 25

10.3 Control System Design

Precise hover during any rescue mission is demanding and difficult, the added complexity of the unpredictable and strong wind patterns on Mount Everest make the task of hovering for 30 minutes extremely daunting. Therefore, reducing pilot workload is the main objective of *Caladrius*'s control system design. The traditional stability augmentation system (SAS) modifies the closed loop response to pilot controls and can potentially lead to handling problems [33]. Furthermore, to provide a good agility without compromising the helicopter stability, a model following architecture was selected for the Automatic Flight Control System (AFCS) because it decouples the command tracking and disturbance rejection problems. The overall model following concept is shown in Figure 10.1.

The feedback compensation, $H(s)$, which is part of the stabilization loop along with rotorcraft dynamics, $P(s)$, stabilizes the vehicle and rejects disturbances. The feedforward loop contains the inverse of rotorcraft dynamics, $P^{-1}(s)$, and the compensation, $H(s)$. Because the rotorcraft's inherent modes are canceled with the feedforward loop, any desired dynamic response is



easily achieved with the command model, $M(s)$, without affecting feedforward shaping or the stabilization loop [34]. This attribute also helps achieve multi-mission capability.

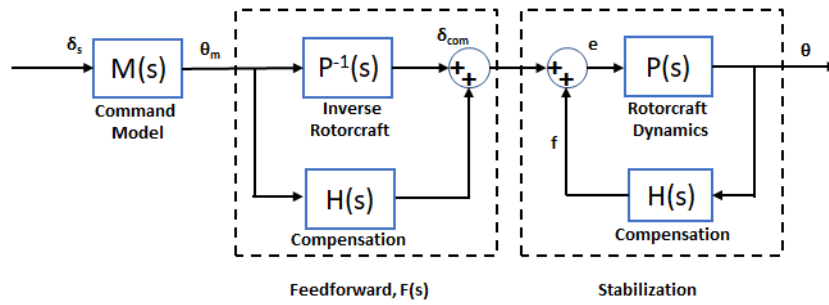


FIGURE 10.1: Generic model following concept

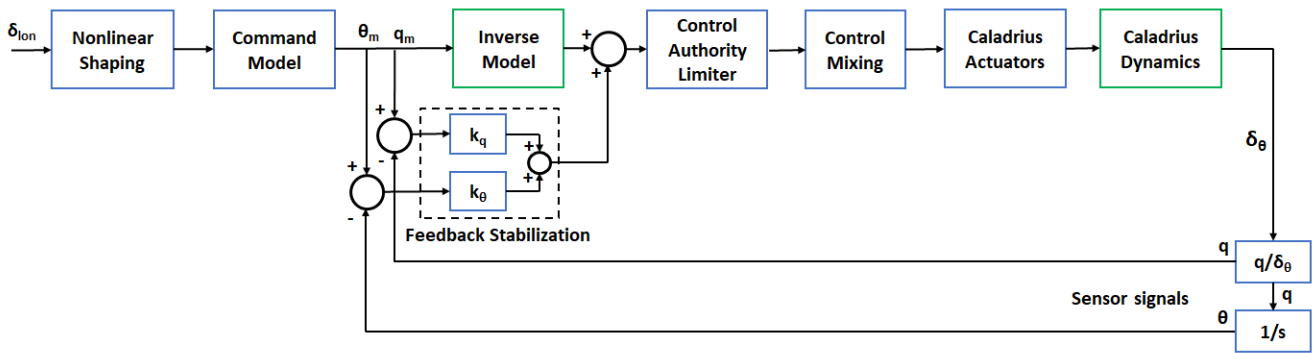


FIGURE 10.2: Model following control law implementation: Pitch attitude channel

The model following architecture (Figure 10.1) was implemented into the pitch channel as shown in Figure 10.2. The roll and yaw channels were included in similar manner. The current control laws of AFCS are to be implemented in the Flight Control Computer (FCC). The control modes of AFCS are following:

Hover/Low speed: Attitude Command Attitude Hold (ACAH) for pitch and roll, Rate Command Direction Hold (RCDH) for heading, Translational Rate Command (TRC) and Altitude Hold for precision hover

Cruise: Attitude Command Velocity Hold (ACVH) for pitch, Rate Command Altitude Hold (RCAH) for roll, RCDH with automatic turn coordination

The transition between modes can be switched by the pilot. The command models for these modes was implemented as simple first and second order transfer functions [35]. The example transfer functions for the command model gives the desired bandwidth and phase delays for Level 1 handling qualities (Figure 10.3) specified in ADS-33E-PRF [36]. The assumption is that the inverse model is exact and the time delay takes care of delay in rotor response. For future development of *Caladrius*'s AFCS, a simple inverse model can be developed and command model can be modified accordingly.

The resulting rate and attitude commands drive the feedforward dynamics and the stabilization loops. Precision hover is achieved using speed feedback from pitot-static probe, altitude from a combination of radar altimeters and GPS.



	Command Model
Pitch	4.0.(0.2)
(θ_m/θ_c)	$s[1.0, 2.0]$
Roll	5.45.(0.2)
(ϕ_m/ϕ_c)	$s[1.0, 2.54]$

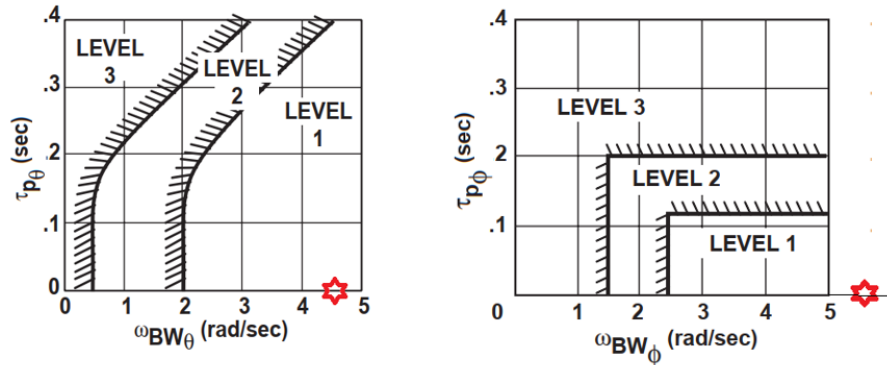


FIGURE 10.3: Transfer functions for command model and corresponding handling qualities

On *Caladrius*, all pilot controls are mechanically linked to the corresponding control surfaces using hydraulic actuators (trim and booster actuators). AFCS has 20% authority on the actuators managed by Control Authority Limiter. This mechanical system was selected over Fly-By-Wire system because it is a proven technology that is safe, reliable, and affordable. This control authority gives nominal frequency for attitude augmentation system [37]. The decoupling of lateral and longitudinal response to respective inputs is ensured through Control Mixing Unit.

A flight director was selected which computes navigation commands using a Guidance Function and can work with or without AFCS. Adding to the reduced pilot workload, *Caladrius* is also equipped with a Flight Management System (FMS) for flight planning and waypoint navigation.

Caladrius is equipped with accelerometers, gyroscopes, radio altimeter, pitot-static port, Global Positioning System (GPS) for the functioning of AFCS. These critical sensors are triple redundant to ensure the flight safety. In addition, the Flight Control Computers are also triply redundant and each working with dual CPUs.

10.4 Stability Derivatives

Once the mathematical model of the rotorcraft dynamics was derived, the control loops were designed around the linearized mathematical model. The roots of matrix A, which contains the stability derivatives, was then obtained and shown in Figure 10.4. Due to bearingless hub design of and the low Lock number (low density), the pitch and roll damping of the bare airframe (no feedback) was high. This ensured good gust response. However, the Phugoid pair was unstable in both hover and cruise, an inherent characteristic of all helicopters. Therefore, proper feedback gains scheduled at different flight conditions were added to stabilize the vehicle. The values of these gains for hover at high altitude and cruise at the lower altitude are given in Table 10.2.

TABLE 10.2: Gains for stabilization loop

Axis	Feedback Parameter	Selected Gain	
		Hover	Cruise
Lateral	Attitude, k_ϕ	1.5	1.25
	Rate, k_p	0.1 sec	0 sec
Longitudinal	Attitude, k_θ	0.75	1.5
	Rate, k_q	0.1 sec	0.1 sec
Directional	Attitude, k_ψ	1.0	1.0
	Rate, k_r	0.1 sec	0.2 sec

In this study, these gains were used for attitude and their rates fed back to control angles rather than stick displacements. With these gains added, the stability derivatives were modified and the key values for hover and cruise are shown in Table 10.3. The force and moment derivatives are normalized by the mass and moment of inertia of the vehicle. Roll and yaw derivatives are



coupled through the product moment of inertia, I_{xz} . Difference in the roll damping term, L'_p , between hover and cruise is apparent due to difference in altitude and thus the Lock number.

TABLE 10.3: Key stability derivatives in hover (leg 2) and cruise (leg 1)

Derivative	Hover	Cruise	Units	Derivative	Hover	Cruise	Units
X_u	-0.0329	-0.0650	1/sec	M_u	0.0737	0.1597	rad/sec-m
X_w	0	-0.2112	1/sec	M_w	0	0.2624	rad/sec-m
X_q	2.5284	2.5662	m/rad-sec	M_q	-5.6584	-5.6444	1/sec
Z_u	0	0.0593	1/sec	L'_v	-0.2317	-0.2010	rad/sec-m
Z_w	-0.1811	-1.0025	1/sec	L'_p	-17.5454	-7.8710	1/sec
Z_q	0	81.1424	m/rad-sec	L'_r	0.1930	0.8919	1/sec
Y_v	-0.0447	-0.2623	1/sec	N'_v	-0.0288	-0.0210	rad/sec-m
Y_p	-2.5460	-1.1358	m/rad-sec	N'_p	-2.3675	-1.0533	1/sec
Y_r	0.5894	-79.0101	m/rad-sec	N'_r	-1.1391	-5.5642	1/sec

The gain scheduling mentioned earlier becomes difficult due to strong coupling between pitch and roll in cruise, which was observed by the effect of horizontal tail area on the roots as shown in Figure 9.3. Therefore, the feedback gains shown in Table 10.2 were tuned simultaneously. The magnitude of these gains were finalized to achieve desired gust response in compliance with ADS-33E 3.3.7.1 [36]. Wind of 74 km/h (40 knots) was considered in hover at high altitude, however wind of 37 km/h (20 knots) speed in cruise (low altitude) was considered to avoid over-designing the feedback system. The roots are shown in Figure 10.4.

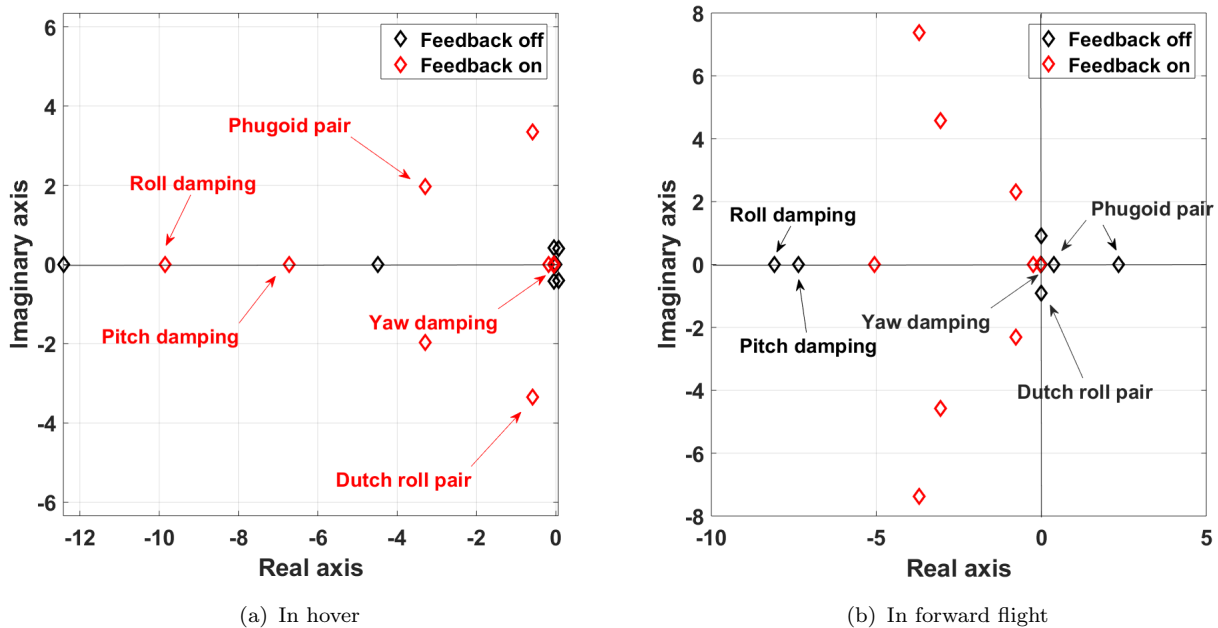


FIGURE 10.4: Stability roots with feedback on and off

The requirement states that the peak value of yaw rate to step lateral gust shall not exceed 0.3 deg/sec per unit gust speed in ft/sec for Level 1 handling quality. The attitude rates response are well within the limit as shown in Figure 10.5.



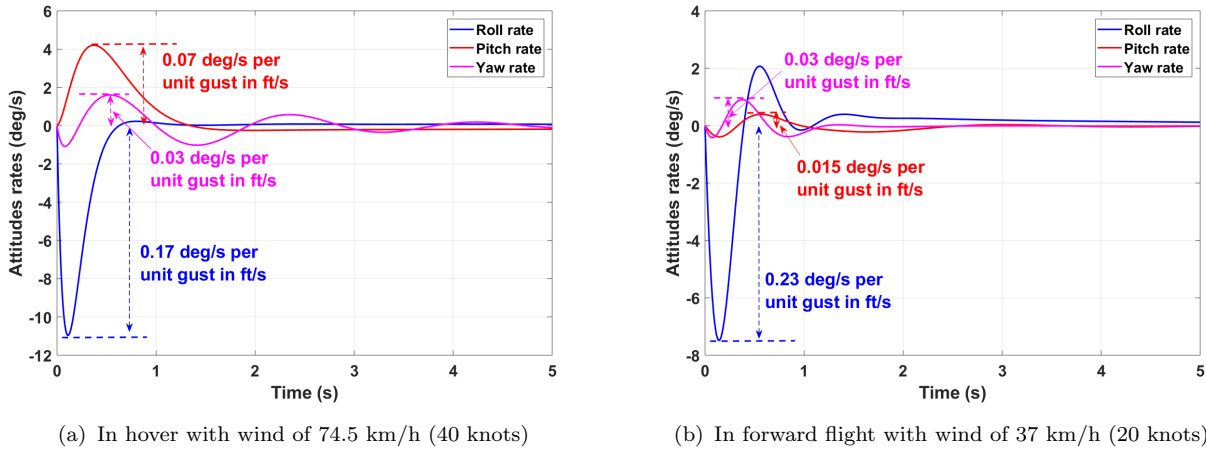


FIGURE 10.5: Body rates response to step lateral wind

10.5 Gust Rejection

The challenge of severe gust at Mount Everest was addressed by carefully choosing the feedback gains of the stabilization loop of AFCS. A typical gust of (1-cosine) profile [38] was applied to the helicopter stabilization loop for the worst condition and the response of the vehicle was obtained in terms of attitudes and corresponding rates as shown in Figure 10.6(a). Also, the attitude rate response shows that the amplitude of the disturbance damps to less than half in one cycle (Figure 10.6(b)) which fulfills the compliance with CS 29 requirement for dynamic stability [39].

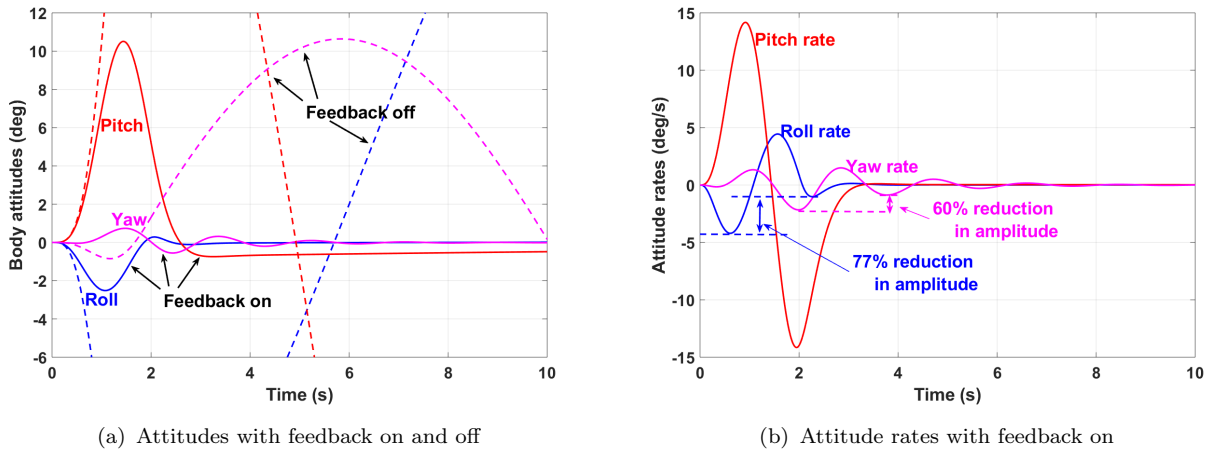


FIGURE 10.6: Vehicle response to cosine gust from 45 deg azimuth in hover

10.6 Effect of Underslung Load

The effect of the underslung load on the helicopter dynamics is dictated by two main factors; (1) mass ratio of the load to the aircraft and (2) cruise speed. The presence of the external load can modify the flight dynamics and the handling qualities as the load may make the helicopter unstable under certain flight conditions [40]. However, it was ensured that this instability does not occur for *Caladrius's* maximum slung load for all expected flight speeds. This is possible because of *Caladrius's* low slung load to helicopter mass ratio (7%). The perturbation equation of motion for the helicopter with longitudinal and lateral motion of the load was derived, and



it was determined that in hover, the effect of the load on the helicopter is negligible. The load may experience sustained and undamped oscillations with the pendulum frequency [41], but it can easily be damped aerodynamically by maintaining some forward speed (dynamic hoisting). Some control systems have been designed for helicopter slung load operations ([42]), but they are only necessary for heavy loads and moderate speed; yet, *Caladrius* does not have any dedicated sensing and control mechanism for underslung load because it was determined that the system was unnecessary.

Redundancy in the sensors, reliable mechanical linkages, and an advanced control architecture that decouples gust rejection and control power increases safety and decreases pilot workload for this demanding mission. In addition, multi-mission capability can easily be achieved by modifying the command model.

11 Transmission Design

Power from the engines is transmitted to the main and tail rotors through a drivetrain system. The high engine rotational speed is stepped down to the needed rotor speed through a set of gears. The gears designed for *Caladrius* are rated for 1193 hp powered by two engines. A first set of engine output reduction gearboxes are used to reduce the rotation speed of the main engines from approximately 3141.6 rad/s (30,000 rpm) to 628 rad/s (6,000 rpm). The main gearbox further reduces the speed to 33.6 rad/s (320.5 rpm). These rotation speeds are given for hover and speed reductions in leg 1 (88%) and leg 2 (93%) are achieved by adjusting the engine speed. A weight minimization strategy is used to identify the appropriate reduction ratios.

11.1 Drive System Configuration

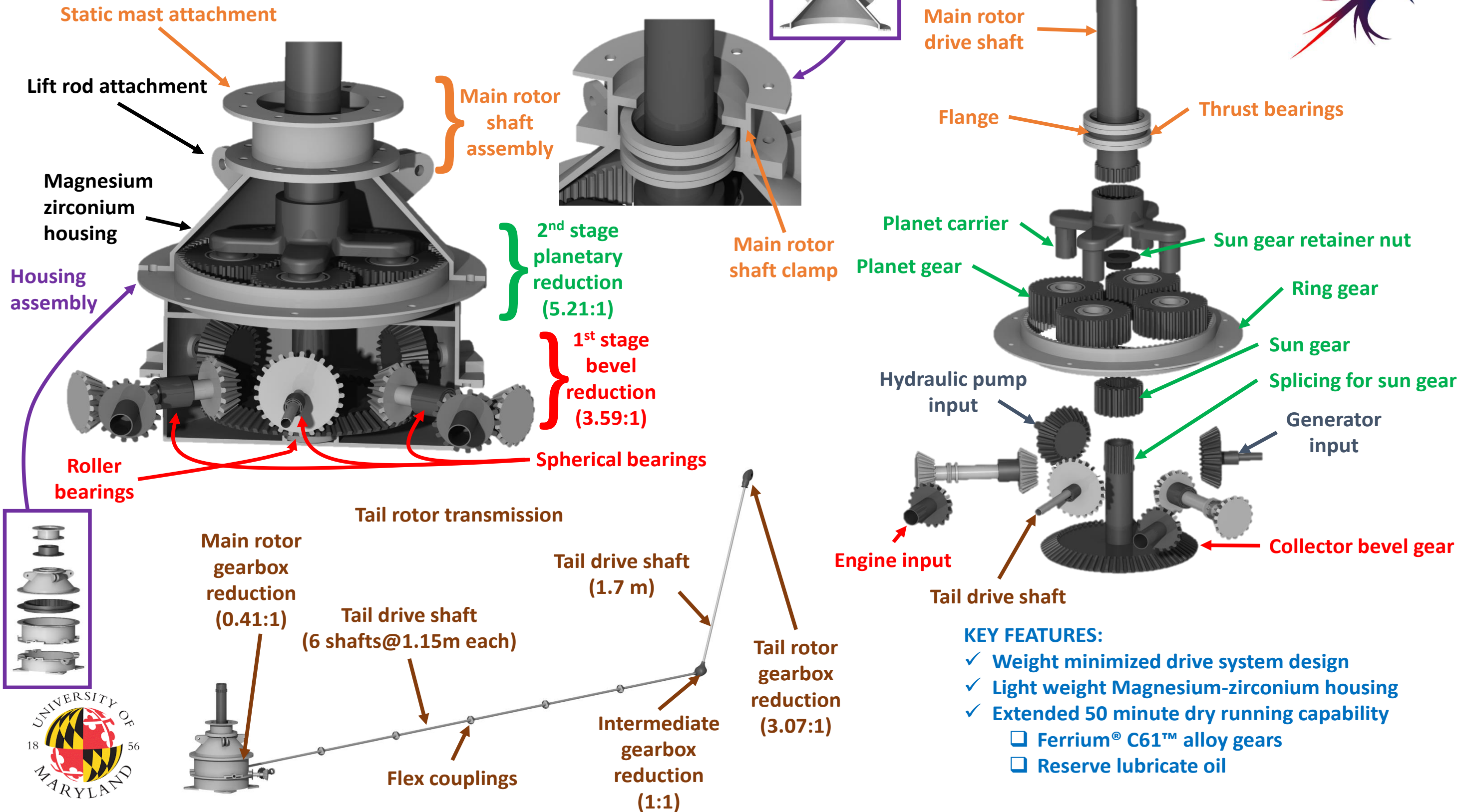
Bevel gears are used extensively in helicopter transmissions for changing shaft angles. For this purpose they are preferred over other gears such as hypoid gears or worm gears because they can be more easily machined and are better suited for reduction ratios of 5:1 or lower required for *Caladrius's* drive system. For this reason all configurations considered for *Caladrius's* drive system used a bevel gear reduction in the first stage. Both bevel gears and planetary gears were considered for the second stage. Planetary gears consist of an input sun gear, a stationary ring gear and planet gears in between the two which drive an output carrier. The main advantage of planetary gears is that multiple contact locations of the sun with the planets splits a large torque which leads to an efficient and more compact speed reduction. It also enables the use of higher reduction ratios of approximately 5:1, which cannot be achieved easily with other gear configurations.

11.1.1 Weight Minimization

The weight of the transmission system is estimated using empirical relations [43]. Three combinations were analysed for *Caladrius's* transmission design, (i) a two stage bevel gear, (ii) a three stage bevel gear and (iii) a two stage bevel and planetary gear setup. The results of the weight minimization process are listed in Table 11.1. An overall reduction from 6000 rpm to 320.5 rpm is targeted in all three configurations, resulting in an overall reduction, $i_0 = 18.72$. For a twin engine system a two stage bevel gear reduction represents the simplest design solution. For this configuration weight minimization expressions result in a first stage bevel gear reduction of 5.47 which is high. This reduction is further broken down into two stages resulting in a three stage bevel gear configuration. Adding more bevel gear reduction stages resulted in heavy and



Transmission Assembly



inefficient designs and they were not considered. Lastly, a two stage reduction (bevel gear and planetary gear) was considered because planetary gears can achieve high reduction ratios efficiently.

TABLE 11.1: Reduction ratios for transmission system

Drive train system	RPM Reduction	Gear Weight (kg)
Two stage bevel	5.47×3.41	156.49
Three stage bevel	$2.41 \times 2.41 \times 3.24$	168.74
One stage bevel and one stage planetary	3.59×5.21	112.95

11.1.2 Choice of configuration

The two stage speed reduction with one bevel gear reduction stage and one planetary gear reduction stage was chosen based on the following criterion:

- **Weight estimation:** The weight of the two stage bevel gear system is approximately 39% higher than the two stage bevel and planetary configuration, this amounts to a large weight penalty.
- **Compactness:** A two stage bevel and planetary drive train results in a more compact design in terms of planform area.

11.2 Design Methodology

The teeth on transmission drive systems are sized based on the stresses that might be encountered in bending at the base of gear teeth and the contact stresses at the point of contact between two teeth which can lead to appearance of fatigue cracks at or below the surface of the teeth, commonly known as pitting. The final sizing of the gear teeth can be carried out using the bending and contact stress relationships enlisted in AGMA standards for aerospace spur and bevel gears. ANSI/AGMA 2003-B97 [44] was followed for bevel gear design and ANSI/AGMA 2001-D04 [45] for spur gear design.

11.3 Gearbox setup

After a nose gearbox reduction, bevel gears are used to change shaft angles by 60° on both sides of the gearbox. The angled shafts are used to drive a collector bevel gear. This is the first reduction stage in the gearbox with a speed reduction of 3.59. Important design parameters are presented in Table 11.2. The collector bevel gear shaft is used to drive the second stage planetary sun gear. The planetary system has four planets for torque splitting. Important design parameters are presented in Table 11.3. Three output shafts are added on the collector bevel gear for the tail rotor drive system and accessory modules. The rotor shaft is splined onto the carrier and is held in place using flanges on the housing. A sprag clutch is added at the location of the connection of the output nose gearbox with the main engine input shaft to decouple the main gearbox from the engine in the event of engine failure to allow for autorotation.

11.4 Notable Features of the Drive System

- **Choice of material for gears:** All gears are to be manufactured using carburized and case hardened Ferrium[®] C61[™] type steel. It has higher core hardness than other



TABLE 11.2: Design parameters for the first stage bevel gears

Quantity (symbol, units)	Pinion	Gear
Number of teeth	17	61
Face width (F , cm)	4.57	
Diametrical pitch (P_d , teeth/cm)	1.86	
Pressure angle (deg)	20°	
Input torque, (T , N·m)	709	
Contact geometry factor, (I)	0.08	
Geometry factor, (J)	0.25	0.19
Load-distribution factor, (K_m)	1.11	
Size factor for pitting resistance, (C_s)	0.66	
Size factor for bending, (K_s)	0.53	
Crowning factor for pitting, (C_{xc})	1.5	
Stress cycle factor for pitting resistance, (C_L)	0.92	0.95
Stress cycle factor for bending strength, (K_L)	0.82	0.84
Allowable contact stress number, (S_c , GPa)	1.72	
Allowable bending stress number, (S_t , GPa)	0.28	
Maximum contact stress, (σ_c , GPa)	1.46	0.77
Maximum bending stress, (σ_b , GPa)	0.18	0.23
Wear factor of safety, (S_H)	1.08	2.13
Bending factor of safety, (S_F)	1.29	1.02

steels used for fabrication of gears like AISI 9310 [46] and a significantly higher tempering temperature, thereby enabling a lighter cooling and lubrication system and extending the runtime in case of loss of lubrication.

- **Hunting ratio:** To increase the lifespan of all gears, the teeth are sized to hunting ratios. This ensures that due to the appearance of any localized defects on a pinion/gear, any subsequent wear on mating teeth can be distributed evenly between all teeth on the mating gear.
- **High contact ratio design:** All gear teeth are designed as high contact ratio gears. Bending and contact stresses are found to be 18% and 19% lower than the corresponding normal contact ratio gears, which gives the gear teeth a higher load carrying capacity [47].
- **Design life:** All gears were designed for an overall design life of 11,000 hours which is 10% more than the standard design life of 10,000 hours.

11.5 Housing

The drive system housing of a helicopter is designed to transfer the loads produced by the main rotor and transmission to the helicopter airframe. Magnesium zirconium alloy is used for the gearbox housing because of its relatively lower weight compared to aluminum alloys. Cored passages are provided to spray lubricate oil at locations where pinion and gear contact occurs. Roller bearings are used wherever large radial loads might need to be reacted because of the motion of the main rotor shaft. Input pinion shafts are supported by spherical ball bearings. The housing of input pinion shafts consists of flanges and thrust bearings to react any axial



TABLE 11.3: Design parameters for second stage planetary gear system

Quantity (symbol, units)	Sun	Planet	Ring
Number of teeth	23	37	97
Face width (F , cm)		7	
Diametrical pitch (P_d , teeth/cm)		2.24	
Pressure angle		20°	
Input torque, (T , N·m)		5089	
Geometry factor for pitting stress, (I)	0.099	0.116	0.260
Geometry factor for bending stress, (J)	0.342	0.375	0.450
Load-distribution factor, (K_m)	1.07	1.05	1.03
Reliability factor, (K_R)		1.002	
Allowable contact stress number, (S_c , GPa)		1.72	
Allowable bending stress number, (S_t , Gpa)		0.28	
Maximum contact stress, (σ_c , Gpa)	1.16	0.84	0.38
Maximum bending stress, (σ_b , Gpa)	0.25	0.22	0.18
Wear factor of safety, (S_H)	1.28	1.76	3.96
Bending factor of safety, (S_F)	1.01	1.12	1.37

loads that could be generated due to bevel gear shaft angle changes. The main gearbox housing has three sections that are attached by bolting. This enables easy assembly and disassembly of gearbox sections. A clamp is provided at the output section of the main rotor gearbox, consisting of flanges supported by thrust bearings to react the lift produced by the main rotor.

11.6 Tail Rotor Transmission

The torque for powering the tail rotor is drawn from the collector gear of the first stage of the transmission. The intermediate gearbox is located at the end of the tail boom. The direction of rotation is changed at this stage with no speed reduction because it would result in a higher torsional design loads on all subsequent drive system components which power the tail rotor. Instead, a larger speed reduction is performed at the location of the tail rotor (tail gearbox). The total length of the tail rotor drive shaft is 8.6 m (28.2 ft) of which 6.9 m (22.6 ft) is along the tail boom and 1.7 m (5.6 ft) along the vertical fin. The shaft is divided into 6 sections along the tail boom (1.15 m (3.8 ft) each) which are connected with each other using flexible couplings. Along the vertical fin, a single shaft is used due to space limitations and relatively shorter overall length. The torque acting on the tail drive shaft is 189.6 N·m (1678 lbf·in). Both the intermediate and tail gearboxes are designed as bevel gears to change shaft angles. The tail rotor drive system designed for *Caladrius* is presented in Table 11.4.

11.7 Oil System

An oil system is provided to lubricate all rotating parts of the transmission and prevent them from overheating. Cored passages pass oil through the housing and dedicated sprays spray oil onto all teeth contact locations. The lubrication system contains a pressure and return manifold. Two oil pumps are provided to pump oil into the transmission housing. Oil filters are used to remove contaminants and metallic particles produced as a result of gear wear. A metallic particulate trap (MPT) is provided which can detect metallic particles and burn them using a high voltage spark. The filtered returning lubricant is passed onto the oil cooler. The cooling system consists



TABLE 11.4: Design parameters for the tail rotor drive system

Parameter	Main gearbox (pinion/gear)	Intermediate Stage (pinion/gear)	Tail Gearbox (pinion/gear)
Number of teeth	61/25	14/14	14/43
Rotation speed (rpm)	1672/4080	4080/4080	4080/1328
Diameter (cm)	32.82/13.44	8.38/8.38	6.22/19.13
Face width (cm)	4.57	1.27	1.91
Safety factor for bending stress	6.93/8.38	1.09/1.09	1.30/1.00
Safety factor for contact stress	4.73/2.99	1.11/1.11	1.08/2.03
Weight (kg)	3.66	1.28	3.42

of a blower fan and radiator. CS (and FAA) 29.927 requires the transmission system to be able to operate with complete loss of lubricant in the event of a leakage for at least 30 minutes. Recent studies have shown that the 30 minutes dry running can be extended to 50 minutes by providing reserve oil reservoirs from which oil can be sprayed onto critical locations of gear contact [48], reserve oil is provided for this purpose. Additionally, Ferrium[®] C61[™], used for fabrication of gears has a high tempering temperature of 900°F, which is approximately 400 – 600°F higher than conventional gear steels. This leads to enhanced dry running capabilities. MIL-L-23699 category certified fluids are chosen for lubrication because they are capable of operating over a large temperature range of –40°C to 50°C [49] which is crucial for *Caladrius's* mission.

11.8 Shaft Sizing

A fatigue analysis using the Goodman criteria was performed to size all rotating shafts [50]. For the main rotor drive shaft, the maximum mean and oscillatory hub loads were evaluated based on trim analyses in cruise and hover for varying C.G. locations. The shaft was sized for combined axial-bending-torsional loading which helped in selecting the outer diameter of the shaft based

TABLE 11.5: Sizes of transmission shafts

Parameter	Outer diameter (mm)	Inner diameter (mm)
Main rotor drive shaft	94	84
Tail drive shaft	21	18
Tail rotor drive shaft	32	28
1st stage bevel gear output shaft	64	57
Drive system input shaft	35	31

on the Goodman criteria [50]. All other shafts were designed for oscillatory torsion loads. The tail drive shaft was checked for critical rotational speed, which was found to be far above the operating rotational speed of 4080 rpm. The factor of safety is taken as 2. The fatigue strength of the material was calculated using appropriate modification factors for fatigue loading [50]. A sizing code was developed to minimize the weight of the shaft which has a tubular cross-section. For varying inner and outer diameters, Goodman criteria was used and the lightest design that provides infinite fatigue life was used. The shaft sizing results obtained are shown in Table 11.5.



The material chosen for all shafts is Ferrium® S53® for its high fatigue resistance and resistance to corrosion over other alloys such as AISI/SAE 4340 [51]. Additionally the shaft is super finished to limit crack growth propagation and nitrided to enhance corrosion and fatigue resistance.

11.9 Weight Estimation

The total weight of the drive system obtained from the sizing estimate is approximately 260 kg (573 lb). An approximate weight for the drive system was obtained using empirical relations and the CAD model. The overall weight of the drive system was found to be approximately 190.6 kg which is almost 26.7% lower than the estimation provided using NDARC [13]. An approximate weight breakdown of the drive system components is given in Table 11.6.

TABLE 11.6: Drive system weight

Component	Weight (kg)
Main rotor gears	99.2
Housing	31.7
Tail rotor gearbox	8.6
Tail rotor shaft	8.4
Bearings	13.8
Main Rotor shaft	7.0
Lubrication system	22.2
Total	190.6

11.10 Load Paths

The transmission drive system is a critical component in the load transfer mechanism in rotary wing aircraft. The large axial lift forces and moments generated by the rotor hub are eventually transferred to the airframe through the drive system and the main gearbox housing. The loads that are required to be reacted are the bending moments, lift and torque generated by the main rotor. To react the lift and mast moments, thick flanges are added to the magnesium zirconium housing and the main rotor shaft. The axial loads appearing on the upper section of the housing are transmitted to the stiffened locations of the airframe through lift rods. Lift rods are made of steel and have solid circular cross-sections. To minimize the weight of the upper conical housing component while simultaneously being able to react the main rotor loads efficiently, the cross-sectional thickness of the housing is linearly decreased with increasing depth (also increasing radius) from the output of the gearbox. The housing itself is mounted on four elastomeric bearings to minimize the effect of vibrations. Any torque appearing on the housing is transferred to the airframe through the bolted connections to be eventually reacted by the moment from the tail rotor thrust.

In summary, *Caladrius's* drive system was designed to reduce a high speed engine input, 6000 rpm after an engine output reduction, to 320.5 rpm for the main rotor with an overall speed reduction of 18.72. This was achieved using a 2-stage reduction process. Bevel gears were used in the first stage (reduction ratio of 3.59) and planetary gears were used in the second stage (reduction ratio of 5.21). A lightweight design for the gearbox was adopted with an extended dry running capability of 50 minutes was provided.

12 Powerplant System

The main power source of *Caladrius* was determined by making a comparison between turboshaft and diesel engines. Current battery and fuel cell technologies have low specific power and specific energy, which result in heavy systems for the required total power. Hence, these two options were eliminated and a comparison between turboshaft and diesel engines was performed. Turboshaft engines are the standard in the rotorcraft industry, with established reliability and usually lower



weight than a diesel engine for the same power. However, at extremely high altitude (low temperature and low density air, low engine mass flow rate) that *Caladrius* is designed for, the engine lapse rate and therefore power loss for the turboshaft engine could make the diesel engine a viable option. These two types of engines were evaluated on the metrics of weight, efficiency, and safety and reliability. The weight calculation breaks down into the power to weight ratio of the dry engine as well as the weight of the required fuel, fuel delivery system, and the transmission. The engine is sized by leg 2 due to high power required and the engine lapse rate at high altitude. For safety, twin engine configuration was decided for *Caladrius*; each engine having an installed power of 50% of the total power. There is a 10% margin included in the total power calculations for safety and robustness as well as general specification creep in certification. It is beneficial to have higher power available because the empty weight of the rotorcraft tends to increase while manufacturing it. In addition, the drag force is also usually underestimated in preliminary design. Finally, this additional power margin also offers additional safety in one engine inoperative (OEI) conditions.

12.1 Turboshaft Engine

Table 4.3 shows that the installed power required is 2502 kW (3355 hp) [ISA]; resulting in, power per engine is 1251 kW (1678 hp). Specific fuel consumption (SFC) was calculated by fitting a logarithmic curve for power vs. SFC values of various engines as shown in Figure 12.1(a). Given the time spent in leg 2 and therefore the required energy, the required fuel weight is calculated by using the AFDD00 weight model [13], as well as the fuel system weight and transmission weight. The engine weight was calculated by using the linear fit from the weight and power values of various engines as shown in Figure 12.1(b). The weight of the total propulsion system is therefore 1007 kg (2220 lb).

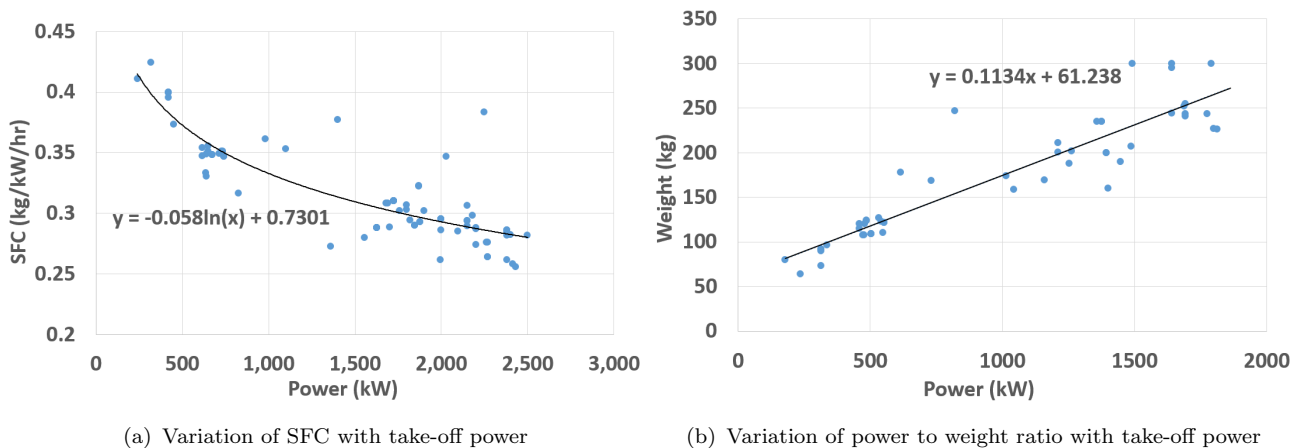


FIGURE 12.1: Turboshaft engine efficiency and weight trends

For a given mission, tank-to-rotor efficiency can be defined as:

$$\eta = \frac{\text{output energy (kW}\cdot\text{h)}}{\text{energy content of fuel (kW}\cdot\text{h)}} = \frac{\sum \text{engine power X time}}{\text{LHV X fuel mass}} \quad [43]$$

where LHV is the lower heating value of fuel and the summation is carried out over all the mission segments since the power varies for each segment. For batteries, the denominator becomes the total energy used for the mission. This metric is the total efficiency of the system to turn fuel into



usable energy for the rotor. Higher efficiency is more beneficial for both cost and environment. Turboshaft engines have a tank-to-rotor efficiency of 0.235 [43]. In addition, they are established in aviation reliability and safety, almost guaranteed not to stall if it operates within the limits specified by the manufacturer.

12.2 Diesel Engine

A diesel engine does not suffer from lapse rate up to 30,000 ft [52]; hence, the required power is 891 kW (1195 hp); per engine is 446 kW (598 hp). Using a specific power of 0.9 kW/kg (0.547 hp/lb) [43], the total weight of a diesel engine is calculated. Using an SFC of 0.23 kg/kW/h (0.378 lb/hp/h), the weight of the fuel was calculated. The fuel carrying system is estimated as half of the fuel weight, and the total transmission weight is estimated by using $W = 0.2914P^{0.9472}$ (SI units). This gives an overall weight of 1440.2 kg (3168 lb).

Diesel engines have a tank-to-rotor efficiency of 0.17 [43], which is lower than of a turboshaft engine. In addition, unlike turboshaft engines, diesel engines have the possibility to stall. Other complications include fuel filters, carburetors, starters, and start and stop issues. Hence, the diesel engines are considered inferior in terms of reliability and safety for the present mission.

12.3 Engine Selection

The turboshaft engine was selected because of the reduced weight, increased safety and reliability, and increased tank-to-rotor efficiency. With a required installed power of 1251 kW (1678 hp) per engine and the goal of the lowest weight, Pratt & Whitney Canada PT6C-67A (Figure 12.2) was selected. This engine can provide a take-off power of 1447 kW (1940 hp) [ISA], has dry weight of 190 kg (419 lb), and an SFC of 0.308 kg/kW/h (0.506 lb/hp/h). The output shaft speed is 30,000 RPM, the diameter is 635 mm (25 in), and the length is 1651 mm (65 in) [53].

This results in an actual system weight of 926 kg (2041 lb) [54], which is lower than the value calculated from the linear fit of Figure 12.1(b).

After choosing the main power source for *Caladrius*, different options for powering the tail rotor was investigated.

12.4 Tail Rotor Power

After deciding the engine type for the main rotor, powering the tail rotor separately with an electric motor driven by a generator, batteries, or fuel cells was also considered.

A considerable portion of the empty weight of the rotorcraft is the engine weight. Due to the lapse rate and high power required at high altitude, engine weight becomes even more predominant. Hence, offloading the turboshaft engine by using an electric motor for the tail rotor was examined. Moreover, having a tail rotor speed that is able to be changed independently from the main rotor might be advantageous because of the combination of the high speed cruise and high altitude hover with possible high wind drafts, both of which may require different optimal tail rotor rotational speeds. In addition, a simpler transmission may be possible if the transmission is not

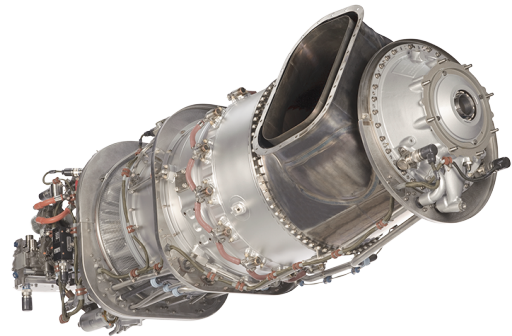


FIGURE 12.2: PT6C-67A engine

required to change directions towards the tail rotor and driveshaft, intermediate gearbox, and tail rotor gearbox can be eliminated.

12.4.1 Weight Calculations

Option 1: Baseline

The baseline case is where both the main and tail rotors are powered by the same turboshaft engines. To compare the weights of the alternatively powered tail rotor systems, the system weight of the baseline tail rotor was calculated. The tail rotor power is conservatively assumed to be 10% of the main rotor power. Weight of the tail rotor transmission system, which includes driveshaft, bearings, gearbox, and couplings, was determined. The amount of fuel required to power the tail rotor is found by multiplying the SFC of the engine by the energy required, and this provides a total turboshaft-powered weight.

Option 2: Battery Powered Tail Rotor

This option is defined as the main rotor being powered by the engines, and the tail rotor solely being powered by batteries which are connected to an electric motor. Based on the Request for Information (RFI) responses, batteries can be replaced at the refueling stops; hence, they are not required to store the energy needed to complete all three legs at once. Batteries must be sized for the larger of the power or energy requirements. Given the current technology, the best Lithium-Ion battery has a specific power of 0.34 kW/kg (0.207 hp/lb) and a specific energy of 0.25 kW·h/kg (0.152 hp·h/lb) [43]. The battery weight must be added with the weight of cabling to the tail rotor as well as the electric motor and the associated gearbox. The cabling required would be an additional 20 kg (44.1 lb) [43], and the specific power for the motor and gearbox combined is 2 kW/kg which results in 55 kg (121.25 lb) [43]. The weight saving would be from the weight of the tail rotor driveshaft and intermediate and tail rotor gearboxes as well as the decrease in fuel and engine weight. This results in a system that is 463.6 kg (1019.9 lb) heavier than the first option.

Option 3: Generator Powered Tail Rotor

This option is defined as the engines providing the power to the main rotor and generators providing power to the electric motor that is connected to the tail rotor shaft. The system would include the generators as well as the motor and a gearbox. Including the efficiency of both the generators and the motor (95% each), total required power is calculated. The specific power for the best generator in use currently is 3.75 kW/kg which results in a weight of 29.5 kg (65.04 lb) [43]. The weights for the electric motor, gearboxes and cabling are the same as the second option. The weight saved is only the weight of the driveshaft and tail rotor gearboxes, because the engine would still be using the fuel to generate electricity. This results in a system that is still 128.5 kg (282.7 lb) heavier than the first option.

Option 4: Fuel Cell Powered Tail Rotor

This option is defined as the main rotor being powered by the engines, and the tail rotor being powered by fuel cells. The weight for this option is calculated identically to the second option except from the fact that the specific energy is 0.65 kW·h/kg (0.396 hp·h/lb)[43]. The fuel cell weighs less than the batteries, but the overall system is still 242.6 kg (533.7 lb) heavier than the first option. PEM fuel cells have the additional problem of hydrogen storage; SOFC work with conventional fuel but have poor specific power and operate at a very high temperature, creating a hot spot in the tail with no benefit.



Weight breakdown and comparison of all the options explained above is presented in Figure 12.3.

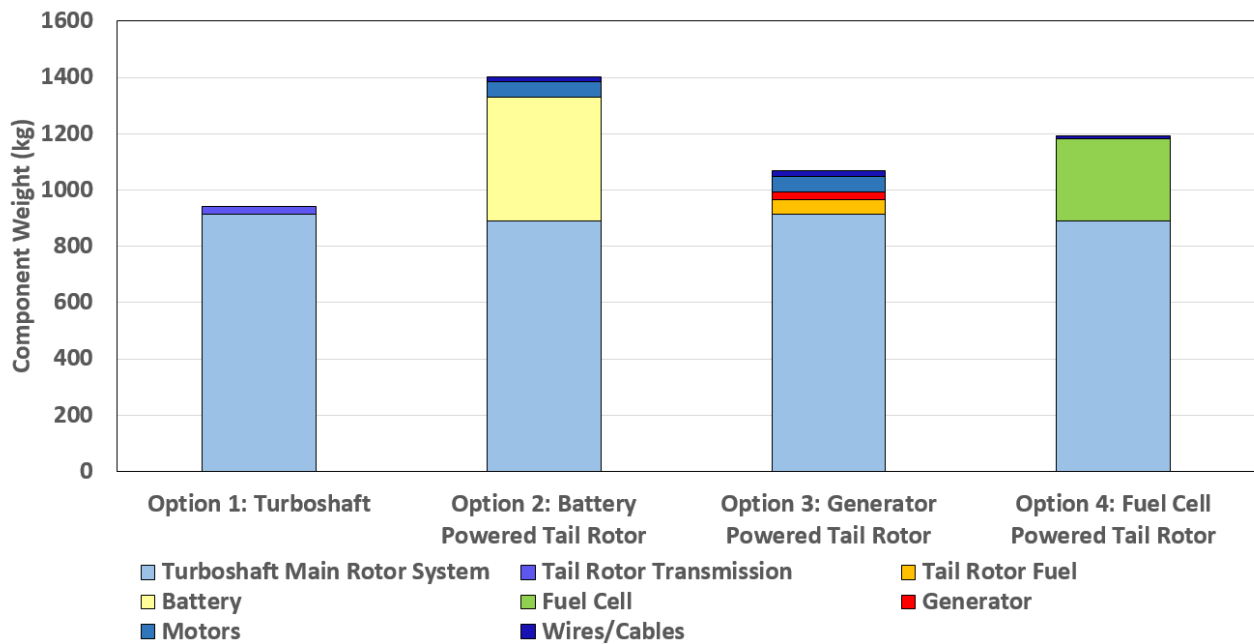


FIGURE 12.3: Powerplant system comparison

12.4.2 Performance Analysis

In addition to the weight calculations, a performance analysis was also carried out. The required power for different tail rotor speeds was calculated, and it was observed that the rotational speed for minimum power changed minimally for different wind speeds as shown in Figure 8.3. Hence, it can be concluded that no real performance gain would be achieved with an electric powered tail rotor after all, at least for this mission.

With the increased weight and no performance gain even with high wind speeds, the idea of an electric tail rotor was abandoned and the conventional configuration of tail rotor driveshaft from a turboshaft engine was selected for tail rotor propulsion.

13 Airframe and Landing Gear Design

13.1 Airframe Design

Caladrius's airframe structure is built around seven bulkheads. The structure consists of five larger bulkheads and two smaller ones at the ends, as shown in Figure 13.1. The bulkheads were spaced based on the location of large components such as drive system, engines, doors, windows and cabin space while minimizing the flat plate area. Two keel beams run along the base of the airframe to support the cabin floor. A transmission deck supports the drive system. It is supported by cross beams as shown in the zoomed image in Figure 13.1. A model of the airframe was generated using CATIA V5. The model was then imported into ANSYS for structural analysis. According to CS 29.337, the airframe is to be sized for a load factors ranging from 3.5 to -1. Aluminum lithium alloy (2090-T86) was used to for the bulkheads and keel beams due to its high specific strength and high specific energy absorption capabilities in case of hard landings. The highest stressed locations on the airframe have a safety factor of 1.84 which is greater than 1.5 required by CS 29.303.

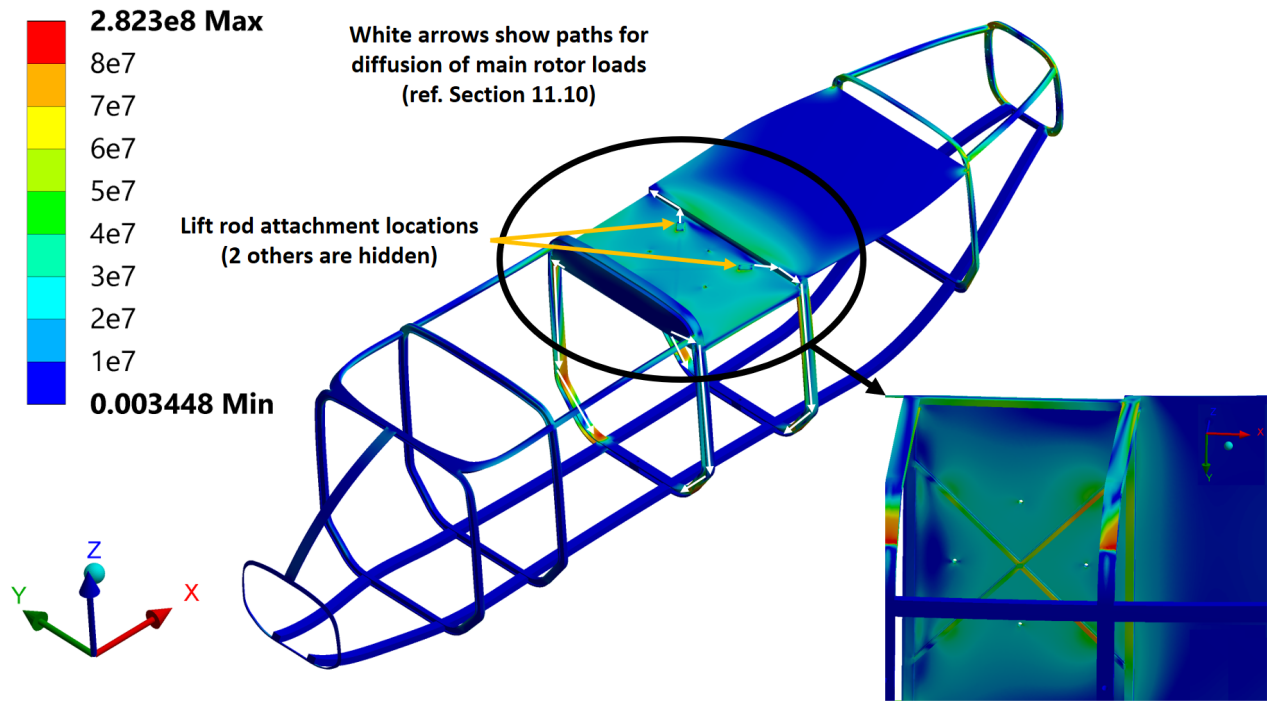


FIGURE 13.1: Airframe stress analysis results (all the stresses are in units of Pascals)

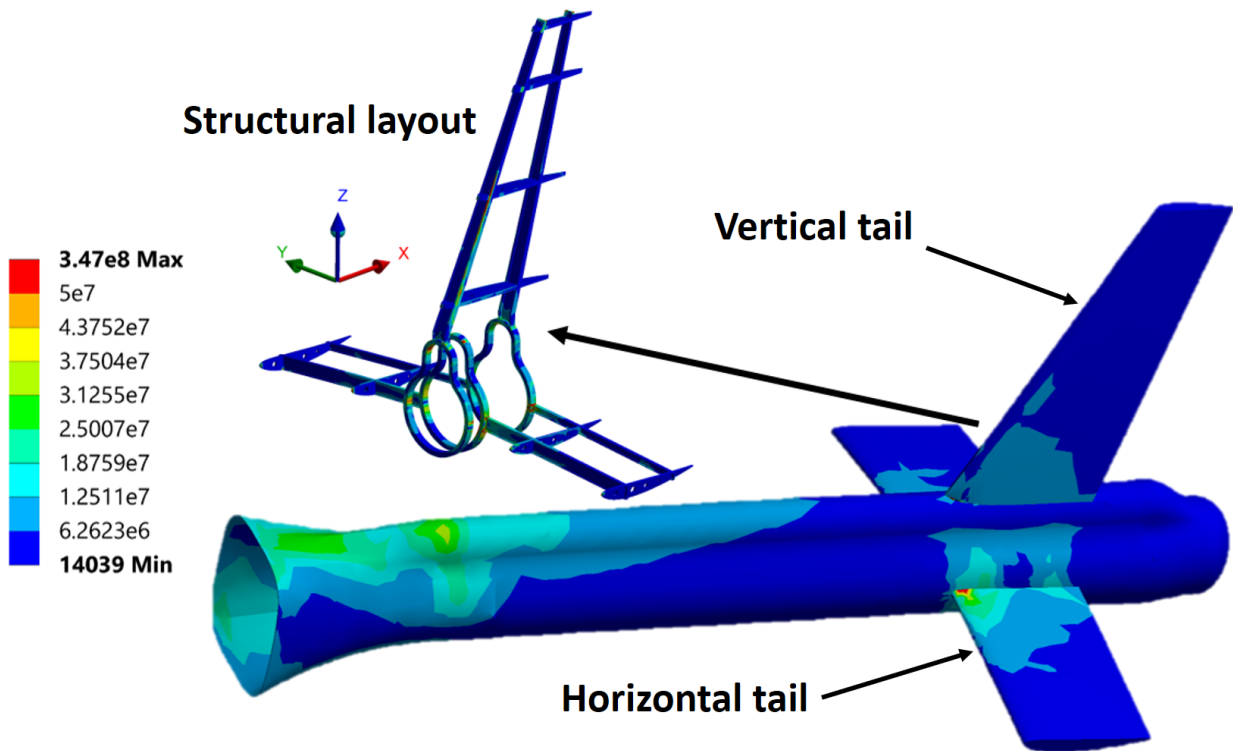


FIGURE 13.2: Stress analysis of tail boom (all the stresses are in units of Pascals)

The horizontal and vertical tails are made of Aluminum material and tail boom is made of E-glass composite sandwich with honeycomb in the middle to increase the bending and torsional stiffness [55]. CS 29.351 and CS 29.427 stipulates a number of load cases for these structures. Updrafts and downdrafts expected on Mount Everest were considered also for the tail components. Using



CS 29 load cases and combining with an updraft of 20.6 m/s (40 knots) on one side of the horizontal tail and downdraft on the other side where applicable, the most critical condition was obtained. The empennage and tail boom were sized for this case for a factor of safety of 1.5. Figure 13.2 shows a visualization of the stresses that were generated on the tail boom.

13.2 Windshield

The windshield and bubble window were sized to withstand a 1 kg (2.2 lb) bird strike at V_{NE} (170 knots) as given by 14 CFR 29.631. The thicknesses were optimized such that the components are as light as possible while having a stress safety factor of 1.5 with respect to the material yield stress. Using the Altair subroutines, the bird strike was modeled statically, dynamically, and aerodynamically. The impact from the windshield and the bubble window can be seen in Figure 13.3(a) and Figure 13.3(b) respectively.

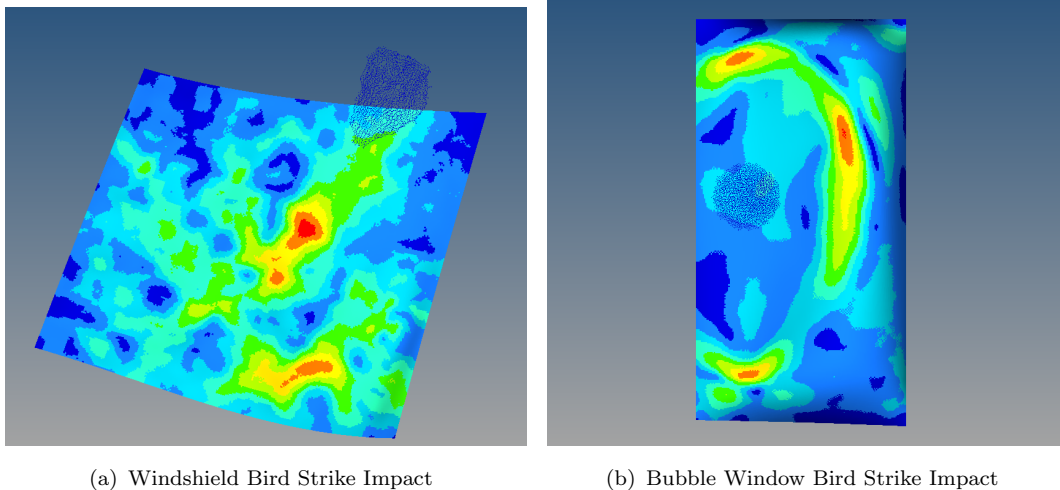


FIGURE 13.3: Bird strike impact on windshield and bubble window

13.3 Landing Gear Design

The main types of landing gears used in helicopters are skid landing gears and wheeled landing gears of retractable and non-retractable type. Skid landing gears are well suited for helicopters heavier than 12000 lbs [43]. However, they also induce a significant drag penalty compared to retractable wheeled landing gear. A simple sizing study was carried out for skid and retractable wheeled landing gears for the complete mission profile given in the RFP. The required approximations were in accordance with NDARC [13].

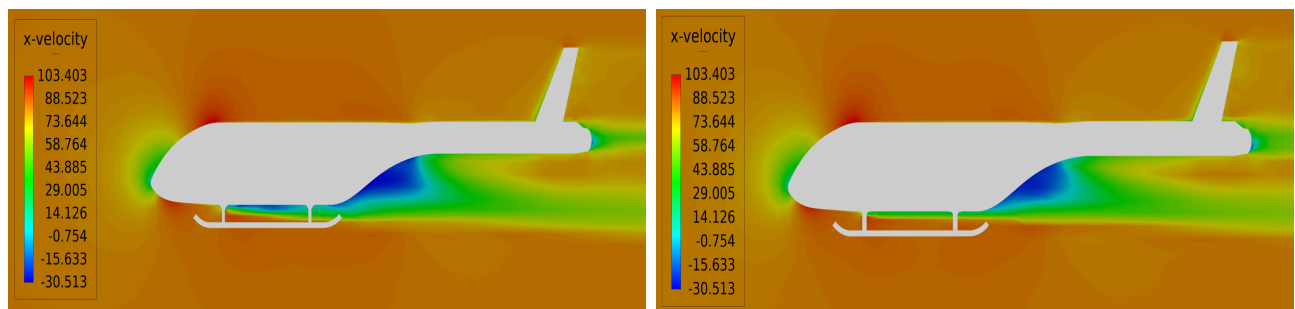
TABLE 13.1: Sizing results for landing gear configurations

Quantity (units)	Retractable wheeled landing gear	Skid landing gear
Gross weight (kg)	3638	3500
Flat plate area (m ²)	0.95	1.20
Installed power (kW)	2595	2509
Fuel weight (kg)	238	232

For the given mission profile, *Caladrius* spends a large portion of the first and third leg in cruise while the second leg is predominantly hovering flight. While skid landing gears induce more

drag in cruise, they are better suited for hovering missions due to lower weight. The overall performance of skid and wheeled gears for the given mission profile is compared in Table 13.1, and it was found that skid gears result in a more efficient aircraft. This is because the critical aspect of the mission is hovering at high altitude for 30 minutes. A lighter helicopter is better suited for this high altitude mission; therefore, skid landing gear was chosen for *Caladrius*.

The length of the landing gear was determined using pitch and roll angles for static stability while the helicopter is on the ground. The cross tubes on the landing gear primarily carry the transverse loads from the fuselage. The design loads on the cross tubes are evaluated as per CS 29.725 regulations. For normal landing conditions, a drop from a height of 330 mm (13 inches) is used to determine load factors. Chernoff [56] determined these load factors experimentally for both forward and aft cross tubes. Based on these results, an equivalent static load analysis was performed and bending moments were evaluated for these loads at critical locations. To size the cross tubes, a variety of cross-sections were considered. The circular cross-section was found to be slightly lighter than the elliptical cross-section (30.5 kg for circular versus 32 kg for elliptical). However, the elliptical cross-section was significantly more efficient in forward flight (the flat plate area of *Caladrius* with elliptical cross tubes was 10% lower than that of circular cross tubes). CFD analysis was done to compare the aerodynamic performance of the circular and elliptical cross-sections using Altair HyperWorks Virtual Wind Tunnel. It was found that due to landing gear-fuselage interaction, more flow separation was observed for the circular cross tubes, which can be seen in Figure 13.4. For this reason elliptical cross tubes were chosen for *Caladrius's* landing gear.



(a) Fuselage-landing gear interaction for circular cross tubes causes early separation of flow (b) Fuselage-landing gear interaction for elliptical cross tubes results in delay in flow separation

FIGURE 13.4: Comparison of elliptic and circular cross tubes for landing gear

13.3.1 Crashworthiness

In case of hard/crash landings, energy attenuation mechanisms are required to absorb the kinetic energy of the aircraft. A part of this energy is dissipated by allowing large plastic deformations in the landing gear. It is important to provide appropriate materials for this purpose. Aluminum alloys are generally used in landing gears because of their ductility. Aluminum 7075 was chosen for the landing gear because of its higher strength to weight ratio. Additionally, further energy dissipation takes place by the buckling of keel beams.

Any remaining kinetic energy is dissipated by stroking of the helicopter seats. Fixed-load energy absorbers (FLEAs) are tuned to operate at a constant load throughout their operational lifetime. They are generally tuned to provide 14.5 g seat deceleration. For lighter passengers, this can be a cause for serious injuries. An improvement to FLEAs are fixed-profile energy absorbers

(FPEAs). They are designed to stroke more efficiently than FLEAs and limit the action of large deceleration loads on passengers to a shorter interval of time but they are also tuned to operate at a predetermined load and passenger weight. Variable load energy absorbers (VLEAs) are designed such that they can be tuned to operate at different levels of forces. This can be adjusted depending on the weight of the passenger. For this reason, the light-weight wire bender type VLEA was added to all the seats, to attenuate shock loads that are encountered during hard landings.

Finally semi-active magnetorheological (MR) energy absorbers are used to improve vibration isolation from rotor loads. For a four-bladed helicopter, they have been proven to successfully attenuate 90% of all 4/rev rotor vibrations for the 50th percentile male [57] with a minimum weight penalty. In the event of a crash, the MR damper can stroke up to a limited amount after which the wire bender VLEA is allowed to deform in order to attenuate the remaining loads.

In summary, *Caladrius's* airframe was designed to withstand high load factors and high updrafts/downdrafts observed at Mount Everest. The landing gear cross tubes were designed for the mission profile, requiring efficient cruise in legs 1 and 3 and 30 minute hovering flight during leg 2. Efficient vibration isolation through magneto-rheological damping of seats ensures comfort of crew and passengers.

14 Avionics and Search & Rescue Equipment

High safety and low pilot workload are crucial for *Caladrius* to successfully complete its mission. These design drivers were prioritized along every step of the design process. In accordance with these two design drivers, state-of-the-art search and rescue equipment and avionics that enable single pilot day and night IFR operations were selected. In this chapter, the most important equipment are described and Table 14.1 provides a detailed equipment list, with weight, dimensions, and power consumption. The equipment marked with an asterisk are specifically selected for mountain rescue missions. The displays for some of the avionics are shown in the glass cockpit designed for *Caladrius* (Figure 14.1).

14.1 Automatic Flight Control System

Caladrius is designed to expeditiously and precisely locate and then rescue any rescuees, even in adverse weather conditions. Considering that the most critical leg of the mission (leg 2) will be performed by a single pilot, reducing the pilot workload is essential. An automatic flight control system can drastically reduce the workload.

Caladrius is equipped with triple redundant Stability Augmentation System (SAS) and four-axis Automatic Flight Control System (AFCS) as well as a Flight Director and a Flight Management System (FMS). AFCS has authority over collective, longitudinal and lateral cyclics, and pedal motion. This enables the use of flight control modes such as attitude and altitude hold, which is especially valuable during the rescue operation, where the pilot has multiple tasks and a very high workload. The critical data that flight control system uses are provided by triple redundant electrically heated pitot-static tubes, inertial measurement units (IMU), GPS, and radar altimeter.



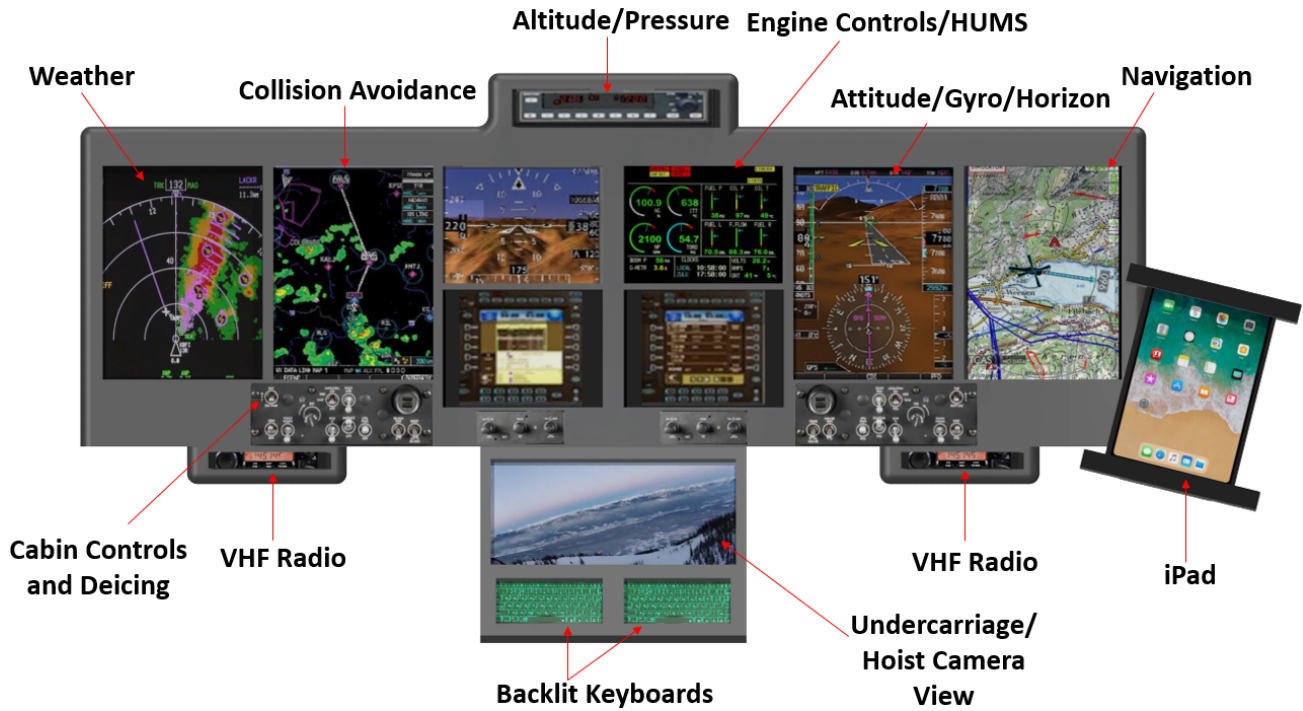


FIGURE 14.1: *Caladrius's* Glass Cockpit

14.2 Search Equipment and Hoist System

Due to possible snow, whiteout, fog, and high wind conditions in the rescue area, effective mountain search equipment is of utmost importance for this mission. *Caladrius* is equipped with a powerful external searchlight (25 million candlepower), shown in Figure 14.2(a), and an electro-optical system (camera turret and hand controller), shown in Figure 14.2(b); providing thermal imaging capabilities with a coverage of 360° azimuth, and 150° elevation. This camera can also be used as a landing camera instead of relying on mirrors that increase the flat plate area.



FIGURE 14.2: Some of the search equipment

In the scenario of the rescues being trapped under snow, where the electro-optical system would be unable to detect their heat signature, an avalanche detector can be used by the crew to locate

the rescuees. The avalanche detector is shown in Figure 14.3. This system has a range of 200 m (656 ft) through air and 30 m (98 ft) through snow and it requires the rescuee to be wearing a reflector on them. Many common brands of mountaineering equipment routinely integrate these reflectors into clothing such as jackets, pants, boots, backpacks, and helmets, meaning most Mount Everest climbers are already equipped with these reflectors.

Finally, night vision goggles are provided for the crew to increase safety through situational awareness and navigation ability. For ease of access, these goggles are attached to each crew member's helmet, as shown in Figure 14.2(c). An electronic rescue hoist with 91.4 m (300 ft) cable length is installed at the starboard side of the helicopter. It can raise and lower a 272.1 kg (600 lb) load at a speed of 45.7 m/min (150 ft/m). A translating drum type hoist was chosen to fix the cable payout point.

Additionally, a camera pointing down along the cable is integrated on the hoist to provide pilots with a visual of the operations in addition to the bubble side window. As a result of the advanced automatic flight control system designed for *Caladrius*, the pilot can check the hoist operation from his/her screen so that the delay to take necessary actions is minimized.



FIGURE 14.3: Recco detector for avalanche

14.3 Deicing and Anti-Icing Systems

Main and tail rotor blades, horizontal tail, and vertical tail of *Caladrius* are all equipped with electro-thermal deicing systems per CS 29.1419 [39] to ensure maximum safety and minimum performance penalty due to icing in adverse weather conditions. The pilot(s) turn this system on and off based on use visual cues from ice evidence probes that are included in the design as well as aircraft vibration and performance. Furthermore, the engine inlet and the pitot tube are equipped with anti-icing systems based on CS 29.1093 and CS 29.1323. This prevents the formation of ice at all times as opposed to a deicing system that allows ice to form prior to removing the ice through applying heat. Finally, based on CS 29.773 and Jean Boulet's experience with icing on the windshield of SA 315B Lama helicopter in his altitude record flight [5], equipment for deicing of front windshield and of the side and floor windows are integrated into the aircraft through the use of a transparent conductive material along with a heat controller. Thus, hot air flow for demisting, as well as internal heating ensures there is no loss of visibility due to icing during the mission. Electro-thermal deicing system is chosen over other systems such as fluid, pneumatic, electro-impulse, and vibratory systems and windshield spray-on coatings (under research) due to its high reliability, technology maturity, and lower weight impact.

In addition to the deicing and anti-icing systems, heating pads and blankets are also included to prewarm the engines, gearbox, and oil tanks when the helicopter is on the ground. This ensures that the wear and tear due to cold start can be minimized without using any on-board power when rapid dispatch times are crucial.

14.4 Weather Radar

Although weather information can be transmitted from the ground station, it is beneficial to have an on-board weather radar as a second source for weather data in case of loss of communication. With the help of this radar (Figure 14.4), the pilots are provided with detailed information, including turbulence and precipitation, which informs best approach trajectory planning. Another advantage of a weather radar is that the pilots can detect and avoid clouds or precipitation during IFR conditions, which can help avoid ice formation on the helicopter.

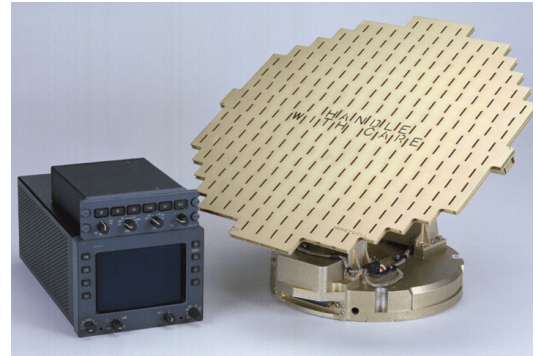


FIGURE 14.4: Honeywell weather radar system

14.5 Air Conditioning System

Air conditioning is important for both crew and the passengers. Heating is provided by using the engine bleed air while a dedicated system is used for cooling. For this mission, heating is especially important considering the low temperature environment and possible hypothermia that the rescuees may experience before the helicopter arrives.

14.6 Communications

Communication with the ground station, other aircraft, and among the crew needs to be consistent and have superior clarity for safe and effective operation of the helicopter. For example, information such as weather, status of the rescuees, and positioning of the helicopter with respect to the extraction point need to be transmitted and received between personnel on the aircraft and relevant offboard personnel.

Bose A20 noise cancelling headsets with wired connections to the aircraft are used with amplifiers to ensure high quality communication among the crew in a noisy environment. Wireless communication is achieved if the same headset is connected to a VHF and UHF capable radio. Communication with other aircraft or ground station is conducted through a VHF radio.

14.7 Navigation

Caladrius is equipped with a state-of-the-art Garmin navigation system to reduce pilot workload, especially while approaching the mountain. Information from weather radar and navigation system can be used to decide on the best approach trajectory to the rescue area. In addition, an iPad mount with a power outlet is also provided for pilot handbooks, navigation, access for live camera feeds near the summit, and weather data that can be downloaded at the international and/or small airport.

14.8 Radar Altimeter

A sensitive altimeter is not only an IFR requirement, but it is also essential to provide precise altitude information, especially when near terrain, so that the pilot and the control system can accurately keep track of the helicopter's altitude. Hence, a radar altimeter with a range of up to 762 m (2500 ft) is included in the avionics.

14.9 IFR Requirements

In order to conform with the RFP requirement that the rotorcraft should be capable of single pilot day and night IFR operations, the equipment and indicators listed below are included in *Caladrius* based on the IFR requirements outlined in paragraph 1303 and Appendix B of CS 29.

- Airspeed indicator
- Magnetic direction indicator
- A clock that shows hours, minutes, and seconds
- Free air temperature indicator
- A non-tumbling gyroscopic bank and pitch indicator
- A standby attitude indicator combined with an internal slip-skid (turn-and-bank) indicator
- A magnetic gyro-stabilized direction indicator
- A rate of climb indicator
- A speed warning device to give aural warnings when V_{NE} (never-exceed speed) is exceeded by 5.6 km/h (3 knots) (Category A requirement)
- Instrument and thunderstorm lights (CS 29.1381)

In addition to the equipment mentioned above, the following IFR requirements are also satisfied in the design:

- Adequate ice protection for IFR systems
- Automatic de-energizing or disconnection of the generating system in the case of hazardous voltage
- Visual means to indicate the adequacy of power being supplied to each flight instrument
- Alternate source for instruments that require a static source

To sum up, state-of-the-art avionics and search and rescue equipment were selected specifically for mountain rescue missions. Hoist camera, weather radar system, camera turret, detector for avalanche, searchlight system, automatic flight control system, wireless intercom system, and anti-icing/deicing systems on various components of the helicopter ensures high mission effectiveness, reduced pilot workload, and high safety.

15 Health and Usage Monitoring System

Health and Usage Monitoring Systems (HUMS) are used to provide diagnostic information through a network of sensors to monitor the working of critical components or subsystems. Three distinct maintenance operations that are required on helicopters are:

- **Hard-time:** These checks are done at fixed intervals.
- **On condition:** On condition maintenance is less rigorous checks than hard-time inspections. They are performed to inspect/replace selected components when suspected.
- **Condition monitoring:** Condition monitoring processes are those where the condition of certain systems/components are monitored on a continuous basis in order to be able to take corrective measures whenever necessary.

Caladrius is equipped with on-line and off-line HUMS. The on-line capabilities include monitoring essential in-flight specifications such as average rotor torque or flight regime characteristics. The off-line capabilities include monitoring of parameters and components that would be required for determining future hard-time overhauls. They are recorded during flight operations and analyzed when the helicopter is on ground.

A chart showing the flow of data through *Caladrius's* HUMS is presented in Figure 15.1.

15.1 Main rotor

Continuous monitoring of the rotor blade is desirable to maintain optimal performance and maximize *Caladrius's* lifespan. A series of strain gauges and accelerometers are added for this



TABLE 14.1: Avionics list

Equipment	Manufacturer	Model	Weight kg (lb)	Dimensions (H × W × D) mm (in)	Power
Four-Axis Automatic Flight Control System	n/a	n/a	22.68 (50)	n/a	n/a
Flight Crew Intercom System	Becker Avionics	DVCS 6100			
		ACU6101 (Audio Control Unit)	0.6 (1.32)	47.6 × 145.8 × 93 (1.9) × (5.7) × (3.7)	27.5 VDC ≤ 0.15 A
		REU6100 (Remote Electronic Unit)	3 (6.6)	195 × 57 × 338.5 (7.7) × (2.2) × (13.3)	27.5 VDC ≤ 4.5 A
Wireless Intercom System*	Axnes	IC3100 (Amplifier)	0.7 (1.54)	128.5 × 45 × 245 (5.1) × (1.8) × (9.6)	27.5 VDC ≤ 2A
		PNG (Basic System)	2.2 (4.9)	n/a	n/a
		CP50 PNG (Cockpit Control Panel)	0.6 (1.3)	n/a	n/a
GPS/Navigation/ Communication (VHF)/ MFD (pilot and copilot)	Garmin	MP50 PNG (Mobile Transceiver)	0.4 (0.9)	n/a	n/a
		2 × GTN 750	4.24 (9.3) each	152 × 159 × 286 (6) × (6.3) × (11.3) each	10-16 W each



Equipment	Manufacturer	Model	Weight kg (lb)	Dimensions (H × W × D) mm (in)	Power
iPad Mount	RAM Mounts	Tab-Tite	0.82 (1.8)	216 (8.5) to 283 (11.13) × 162 (6.38) to 197 (7.75) × 3.3 (0.13) to 14.2 (0.56)	n/a
Cockpit Voice and Flight Data Recorder (CVFDR)	Honeywell	Solid State Digital Voice/ Data Recorder (SSDVDR)	6.8 (15)	n/a	115 VAC or 28 VDC
Health and Usage Monitoring System (HUMS)	Honeywell	RECON	2.9 (6.4)	84 × 184 × 241 (3.3) × (7.3) × (9.5)	n/a
Enhanced Ground Proximity Warning System (EGPWS) and Helicopter Terrain Avoidance and Warning System (HTAWS)	Honeywell	MK XXII	1.8 (3.9)	157.5 × 76.2 × 307.3 (6.2) × (3) × (12.1)	28 VDC 15 W
Traffic Collision Avoidance System (TCAS)	Honeywell	KTA 870 KA 815 (Antenna) 3×KRA 405B (Receiver/ Transmitter)	4 (8.8) 0.4 (0.9) 1.4 (3) each	178 × 114 × 351 (7) × (4.5) × (13.8) 69 × 89 × 151 (2.7) × (3.5) × (6) 88.9 × 76.2 × 279.5 (3.5) × (3) × (11)	22 - 30 VDC n/a 27.5 VDC ± 20% at 850 VDC mA
Radar Altimeter	Honeywell	KNI 416 (Radar Altimeter Indicator) 2 × KA 54A (Antenna)	0.8 (1.7) 0.09 (0.2) each each	82.8 × 82.8 × 169.8 (3.3) × (3.3) × (6.7) 18.5 × 89 × 93 (0.73) × (3.5) × (3.7)	27.5 VDC ± 10% at 120 mA n/a



Equipment	Manufacturer	Model	Weight kg (lb)	Dimensions (H × W × D) mm (in)	Power
Transponder	Garmin	GTX 335R	1.3 (2.9)	42 × 160 × 224 (1.7) × (6.3) × (9.9)	14/28 VDC 0.9 W
Weather Radar System *	Honeywell	WU-880 (Radar + Antenna) WI-880 (Indicator) WC-880 (Controller)	6.8 (15) 5.4 (12) 0.9 (2)	Dia: 304.8 (12) 106.7 × 154.9 × 292.1 (4.2) × (6.1) × (11.5) 47.6 × 146 × 165.1 (1.9) × (5.8) × (6.5)	28 VDC 110 W 28 VDC 36 W 28 VDC 8.5 W
Electro-Optical System *	L3 Wescam	MX-8	7.8 (17.2)	Dia: 211 × H: 262.5 Dia: (8.3) × H: (10.3)	16 - 32 VDC ≤ 180 W
Detector for Avalanche *	Recco	n/a	< 1 (2.2)	n/a	n/a
Searchlight System *	Spectrolab	SC-Y Starsun	25.1 (55.4)	Dia: 280 × H: 420 Dia: (11) × H: (16.5)	26.5 - 29 VDC ≤ 50 W
Rescue Hoist *	Goodrich	44301-10-4	41.8 (92.1)	H: 312.9 × W: 222.2 H: (12.3) × W: (8.8)	28 VDC ≤ 125 A
Hoist Camera *	Rugged Video	HD19	n/a	Dia: 19 × H: 72 Dia: (0.8) × H: (2.8)	10 - 36 VDC
Air Conditioning System	RSG Rotorcraft Services Group	SH3509SW	37.2 (82)	n/a	1900 W
Deicing for Main Rotor, Tail Rotor, Horizontal Tail, Vertical Tail and Anti-Icing for the Engine Intake *	n/a	n/a	35.9 (79.2)	n/a	44.7 kW
Deicing for Front Windshield and Side and Floor Windows *	Astronics	n/a	2 (4.4)	n/a	30 kW
3 × Pitot-Static Probe with Anti-Icing	n/a	n/a	0.06 (0.13) each	n/a	≤ 19 W
Preheat Kit *	Tanis Aircraft	TSHEC145-2143	3.4 (7.5)	n/a	115 V 878 W



purpose. The data from these sensors is compared with a pre-existing database of failure modes compiled during flight testing and certification. Strain gauges also provide data for detection of potential fatigue problems. In the event that a potential failure mode is detected, corrective steps can be taken. The collected vibration data can also be used for routine condition checks such as track and balance.

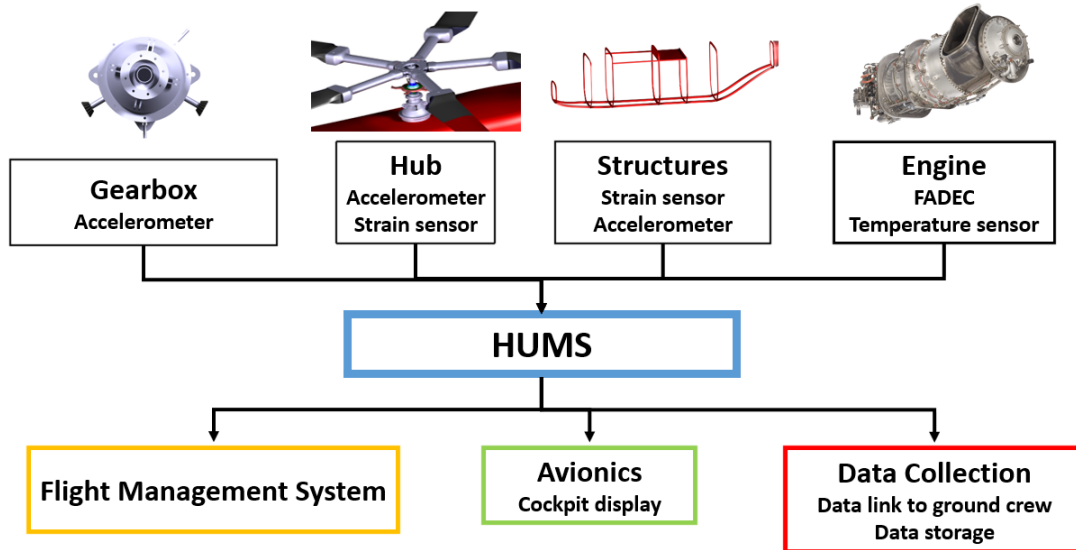


FIGURE 15.1: Health and Usage Monitoring System flowchart

15.2 Engine

Turboshaft engines share the same base technology with engines that power larger commercial and military aircraft; however, the demands on the engine control system are much severe because overall aircraft operation requires a constant rotor speed even under varying loading conditions. For this reason, the main engine is equipped with a full authority digital engine control (FADEC) system. The system transmits important information to the HUMS system including specifications such as time spent above torque limit, flight performance data, oil temperature, and fault monitoring.

15.3 Drive System

Accelerometers are placed on the main and tail rotor gearboxes. The vibrations on both are continuously monitored. The recorded data can be processed to obtain the vibrations on the main and tail rotor drive shafts. The bearings are also monitored for vibrations [58].

15.4 Structure

Accelerometers and strain gauges are mounted at critical locations of the airframe and other load bearing elements such as the gearbox housing. This helps to diagnose any initiation and propagation of cracks in such members.

15.5 Advantages

- **Enhancing safety:** Round the clock in flight health monitoring helps enhance safety of the aircraft and the crew.

- **Increase aircraft availability:** Continuous and efficient health monitoring of aircraft components compounded with automated pattern based fault detection reduces downtime which is critical for *Caladrius's* mission at peak times (May and September) at Mt. Everest.
- **Reduce maintenance costs:** Automated computer based fault determination reduces maintenance costs.
- **Optimize parts and inventory management:** Timely fault detection and efficient tracking of component health helps optimize inventory management.

16 Weight Breakdown and C.G. Analysis

16.1 Weight Breakdown

TABLE 16.1: Weight breakdown

Component	Weight		Component	Weight	
	kg	lb		kg	lb
Main Rotor Group	474.38	1045.82	...		
Blades	257.11	566.82	Air Conditioning	37.20	82.01
Hub	217.27	479.00	Auxiliary Power Group	45.36	100.00
Tail Rotor Group	37.32	82.27	Instruments Group	45.36	100.00
Blades	18.66	41.13	Cockpit Controls	54.43	120.00
Hub	18.66	41.13	Avionics	119.58	263.63
Empennage Group	74.63	164.53	Search and Rescue Equipment	65.48	144.36
Horizontal Tail	51.31	113.12	Camera Turret	6.80	14.99
Vertical Tail	23.32	51.41	Search Light	16.90	37.26
Fuselage Group	387.37	854.00	Rescue Hoist	41.78	92.11
Alighting Gear Group	48.99	108.00	Electrical Group	45.36	100.00
Engine Group	461.44	1017.29	Fuel System Group	9.66	21.30
Air Induction Group	180.71	398.40	Furnishings and Equipment Group	90.72	200.00
Drive System Group	259.91	573.00	Fluids (oil, unusable fuel)	22.68	50.00
Rotor Flight Controls	133.90	295.20	Empty Weight +1% Margin	2693.80	5938.71
Hydraulics for Rotor Controls	34.79	76.70	Fuel	232.24	512.00
Anti-Icing and Deicing Systems	37.83	83.39	EMS equipment	150.00	330.69
Main Rotor Blades	30.41	67.03	Pilot	85.00	187.39
Tail Rotor Blades	1.15	2.54	Pilot/Hoist Operator	85.00	187.39
Horizontal Tail	1.35	2.98	EMS Specialist	85.00	187.39
Vertical Tail	0.64	1.41	Passenger 1	85.00	187.39
Engine Intake	2.28	5.03	Passenger 2	85.00	187.39
Windshield, Side Window, and Floor Windows	2.00	4.41	Maximum Take-Off Weight	3501.04	7718.34
...					



The weight calculations were carried out based on AFDD and Tischenko weight models [13, 43]. *Caladrius's* weight breakdown according to MIL-STD-1374 with full fuel and two passengers is given in Table 16.1. Note that the origin is defined as the intersection of the vertical line drawn tangent to the nose and the horizontal line drawn tangent to the bottom of the landing gear. The axis system is such that x is towards the tail, y is port, and z is up.

16.2 C.G. Analysis

The C.G. and weight change of *Caladrius* during the rescue mission is shown in Figure 16.1.

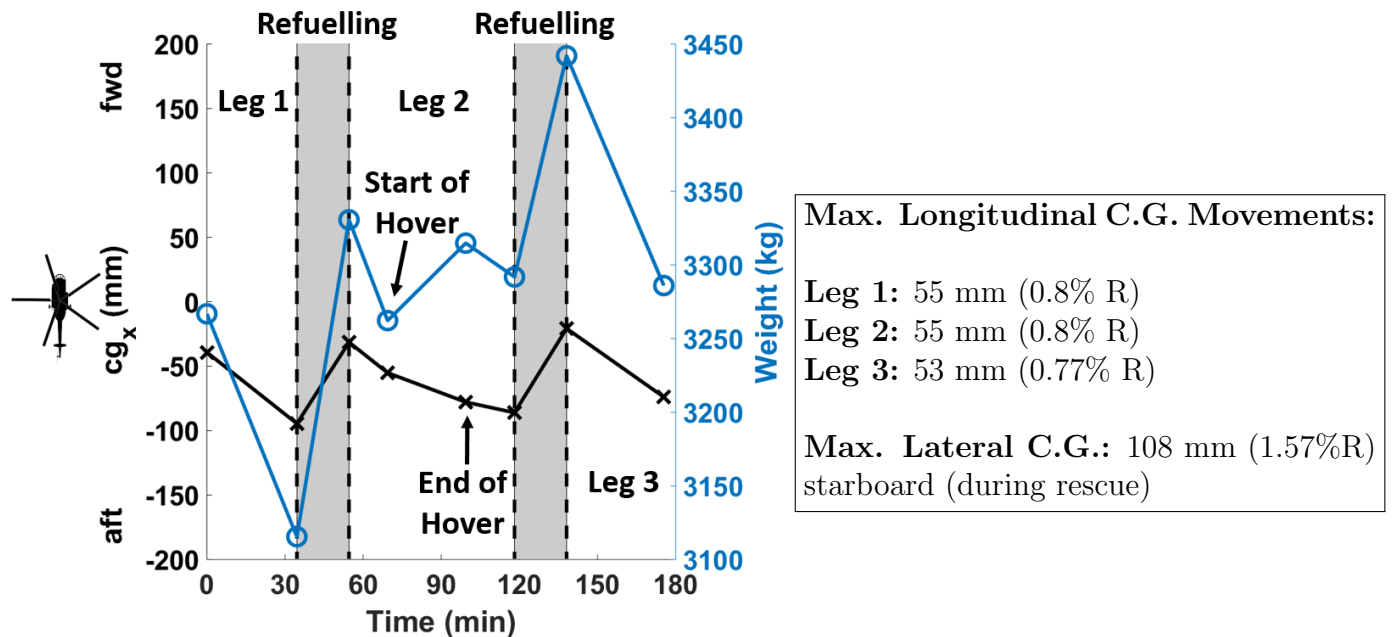


FIGURE 16.1: Longitudinal C.G. with respect to hub and weight change with mission time

17 Acoustics

The noise levels of *Caladrius's* main rotor were analyzed using an in-house acoustic analysis based on Ffwocs-Williams-Hawkings equations, using Farassat formulation 1A [59, 60].

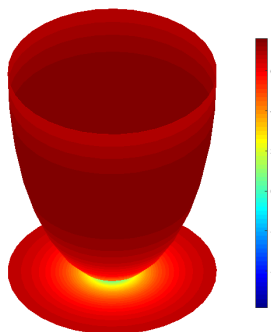


FIGURE 17.1: Noise distribution(SPL in dB) 150m below the vehicle in hover

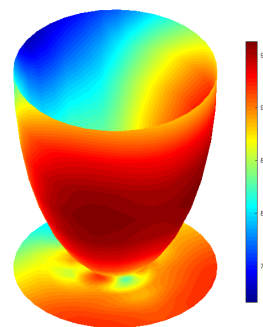


FIGURE 17.2: Noise distribution(SPL in dB) 150m below the vehicle in cruise

The thickness and loading noises were calculated for observers located on a plane 150 m (492 ft) below the vehicle, in accordance with FAA requirements and also on a hemisphere around

the vehicle. The results in SPL are presented in Figures 17.1 and 17.2. Other types of noise generated by the vehicle are high Speed Impulsive(HSI) noise and Blade Vortex Interaction (BVI) noise. High speed impulsive noise, is highly directional and propagates in the plane of rotor. Hence it has little effect on the observers on ground. Blade vortex interaction noise is minimized in *Caladrius* through the use of tip anhedral for the main rotor. The anhedral forces the vortex to start further down the blade, thereby increasing blade-vortex miss distance.

18 Vehicle Performance

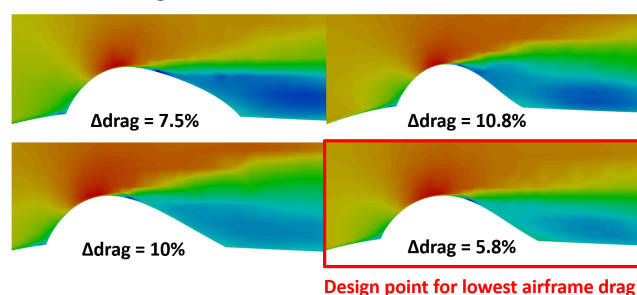
Caladrius was designed for a search and rescue mission at the highest altitudes of the planet with extreme weather conditions. An excellent hover efficiency at the highest altitude and a good cruise performance were aimed for *Caladrius*. Vehicle's flat plate area was estimated using simulations in Altair's Virtual Wind Tunnel. The hover calculations were carried out to determine the ceilings for different take-off weights and ambient conditions. Forward flight calculations were performed to determine the range, endurance and maximum cruise speed. These calculations take into consideration details such as the intake losses, rotor and transmission efficiencies, and power required for avionics. The detailed performance analysis of *Caladrius* is summarized in this section.

18.1 Drag Estimation

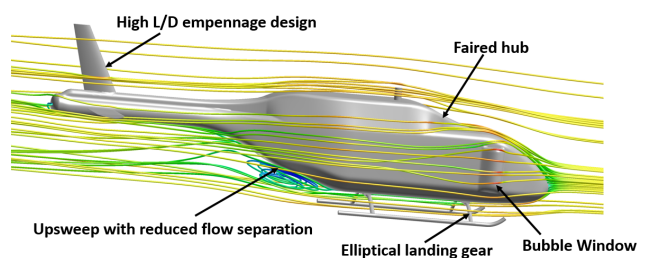
Preliminary estimate of flat plate area of *Caladrius*'s fuselage was carried out using the methods presented by Prouty [31]. Frontal areas for the various components were calculated from the drawings and combined with empirical factors to calculate the flat plate area of the entire helicopter. These estimates were then refined using CFD simulations in Altair's Virtual Wind Tunnel. Simultaneously, several innovative methods were used to streamline the vehicle and reduce its overall drag. These are summarized below:

TABLE 18.1: Component breakdown of flat plate area

Component	f (m ²)	f/A _{MR}	%
Fuselage	0.27	0.00182	27.27
Main rotor hub	0.2	0.00135	20.20
Landing gear	0.16	0.00108	16.16
Empennage	0.14	0.00094	14.14
Landing gear-fuselage interaction	0.15	0.00101	15.15
Bubble window	0.07	0.00047	7.07
Total	0.99	0.00666	100
Additional 20%	1.2	0.00807	100



(a) Increase in flat plate area due for different profiles of bubble window



(b) Flow Stream lines around fuselage

FIGURE 18.1: CFD results using Altair Virtual Wind Tunnel

1. Use of elliptical landing gear instead of conventional circular sections reduced the flat plate area by 10%.

2. Bubble window profile was optimized for minimal increase in vehicle's drag.
3. Upsweep angle of the fuselage was optimized to delay the onset of flow separation.
4. Fairings were used to streamline the flow around engine and main rotor hub.
5. Empennage were designed for high L/D.

Table 18.1 shows the component breakdown of flat plate area of different components. Additional 20% was added to the overall estimate to account for drag from the tail rotor hub, pitch links, turret camera, searchlight, and rescue hoist that are difficult to estimate or predict.

18.2 Hover Performance

The engine of *Caladrius* is sized to meet the requirement of the RFP for HOGE at 8870 m (29,100 ft) and it results in an installed power of 2320 kW at sea level and ISA + 20° state. The available engine power decreases with altitude due to reduced air density as shown in Figure 18.2. The transmission is sized by adding a 10% margin to the maximum torque required for the mission.

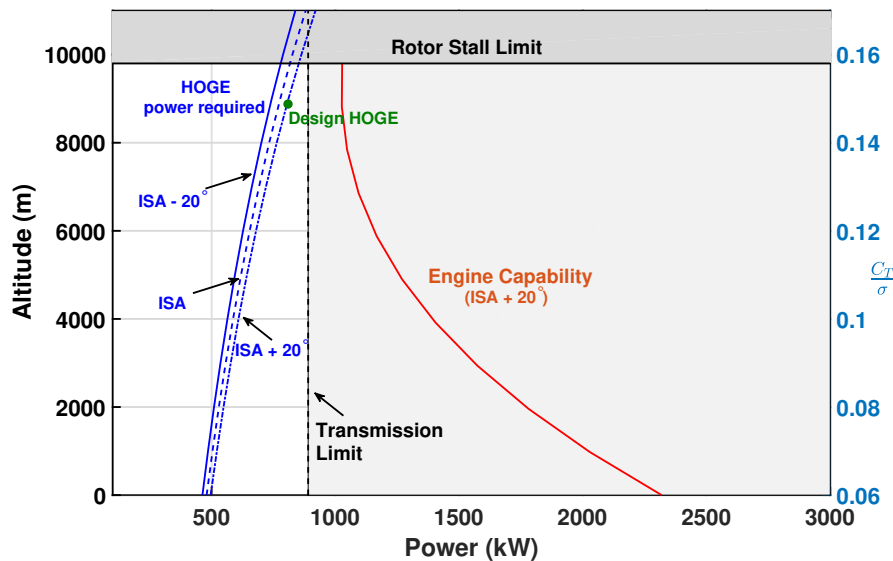


FIGURE 18.2: Variation of HOGE power required at design gross take-off weight (3500 kg) and power available with altitude

The power required to HOGE increases with altitude and with increase in temperature. These required power curves for different temperatures are shown in Figure 18.2. It is seen that HOGE hover ceiling is limited by blade stall, defined by $C_T/\sigma = 0.16$ at approximately 9,800 m (32,150 ft) at ISA + 20° state, not by available engine power or transmission limit. Figure 18.3(b) shows the Weight-Altitude-Temperature plot for *Caladrius*, illustrating the variation of take-off weight of the vehicle with altitude for different temperature conditions. A design gross take-off weight of 3500 kg, which includes the weight of two rescuees, was obtained for *Caladrius* based on the sizing leg: leg 2 (Section 4). A greater margin from transmission limit is available at lower altitudes due to lower power requirements for HOGE (Figure 18.2). This provides the aircraft with the capability to hover with a higher take-off weight at lower altitudes (Figure 18.3(b)). Unlike in extreme altitude, at lower altitudes it is the transmission which limits the maximum lifting capability of the aircraft, and not rotor stall. Figure 18.3(b) shows that *Caladrius* can hover with an alternate design gross take-off weight of about 4500 kg at sea level in ISA condition.



Because most of the structural components of *Caladrius* were sized to a load factor of 3.5 per CS 29 requirements for the design gross take-off weight of 3500 kg, a higher take-off weight will have a lower allowable load factor (but still around 2.8 for 4500 kg).

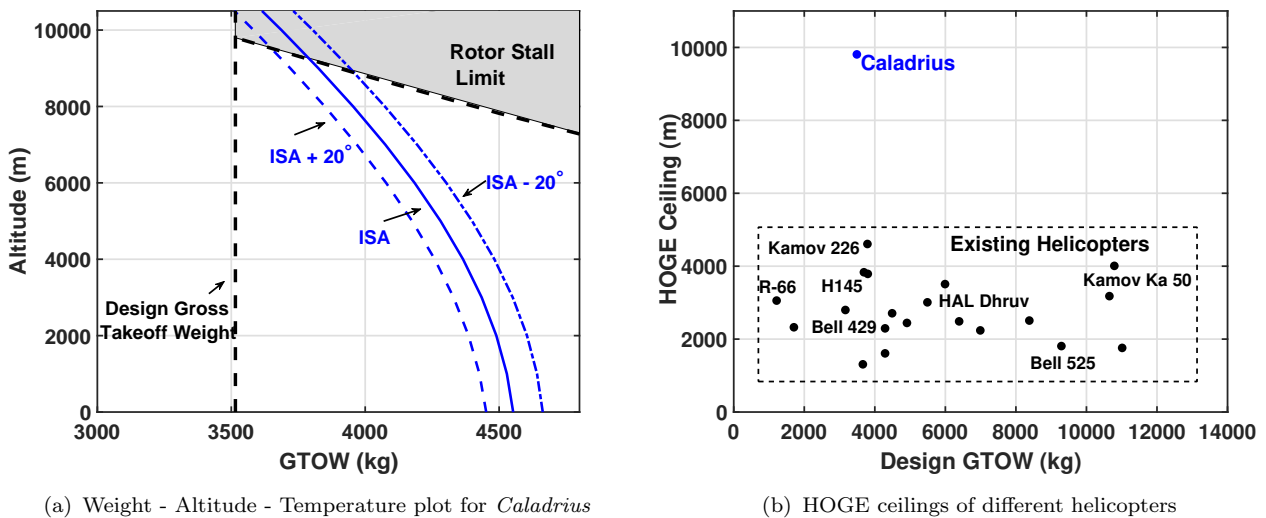


FIGURE 18.3: Hover performance charts

Caladrius was specifically designed for a high altitude mountain rescue mission. None of the existing helicopters have the capability to hover at such extreme altitudes. Figure 18.3(a) shows the hover ceilings of some of the existing helicopters. The maximum hover ceiling of these helicopters with their corresponding design GTOW is around 5000 m. *Caladrius* has twice the hover ceiling of these helicopters, of around 9,800 m (32,150 ft) at ISA + 20° state. This comes at a cost of low payload fraction (high empty weight fraction), low range and endurance 18.4.

18.3 Forward Flight Performance

A time constraint of three hours and a minimum speed of 259 km/h (140 knots) required by the RFP for the mission makes the cruise segments quite important. *Caladrius*'s blades and fuselage were designed to have low drag and superior cruise performance.

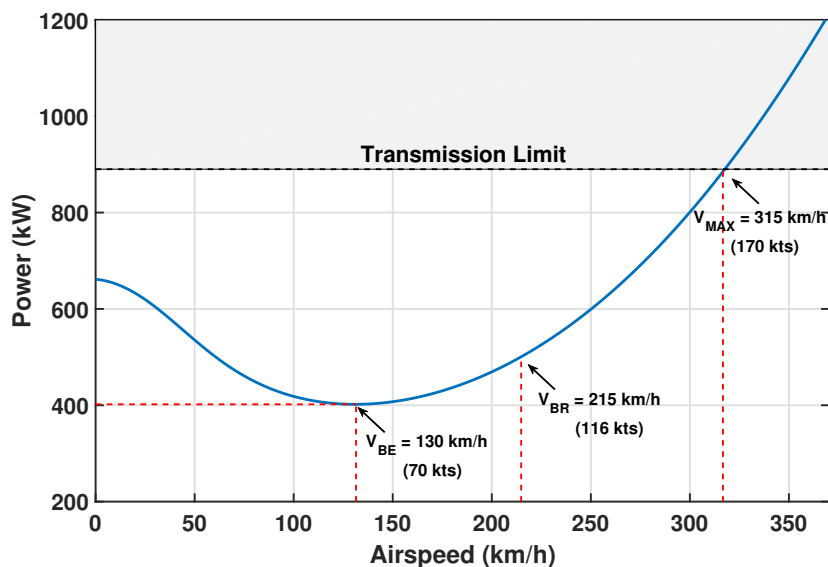


FIGURE 18.4: Power required vs airspeed for design GTOW (3500 kg) at 3780 m, ISA + 20°



The forward flight performance was estimated for *Caladrius* at the design gross take-off weight for different altitudes and temperatures. Here afterwards, all the performance calculations are carried out for design gross take-off weight of 3500 kg (7716 lb), unless stated otherwise. Figure 18.4 shows the variation of the power required with forward speed at 3780 m (12400 ft) and ISA + 20° state.

The speeds for respectively best endurance (V_{BE}) and best range (V_{BR}) are shown in Figure 18.4. The transmission system limits the maximum speed (V_{MAX}) of the vehicle. Figure 18.5 shows the variation of power required with forward speed for different altitudes at ISA + 20° state. The induced power component of the rotor is a major contributor to the total power at lower airspeeds, resulting in higher power requirement for higher altitudes. On the other hand, at higher airspeeds, the parasitic power is a major contributor to the total power, resulting in lower power requirement at higher altitudes. An increase in best endurance speed, best range speed and maximum speed is observed with an increase in altitude as shown in Figure 18.6. This is due to the decrease in atmospheric density with increase in altitude.

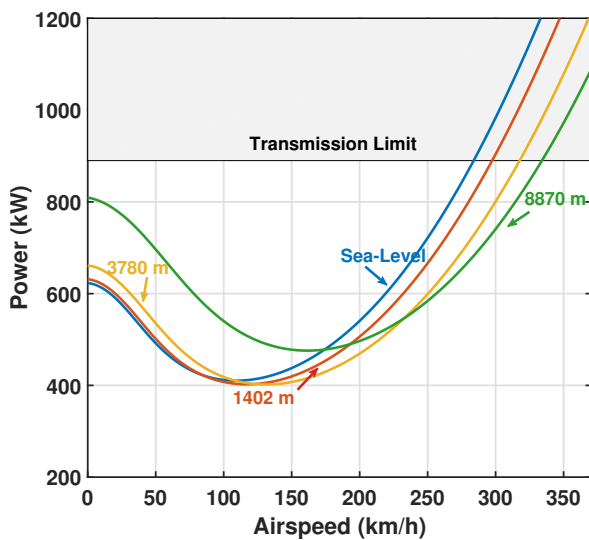


FIGURE 18.5: Power required vs. airspeed for different altitudes, ISA + 20°

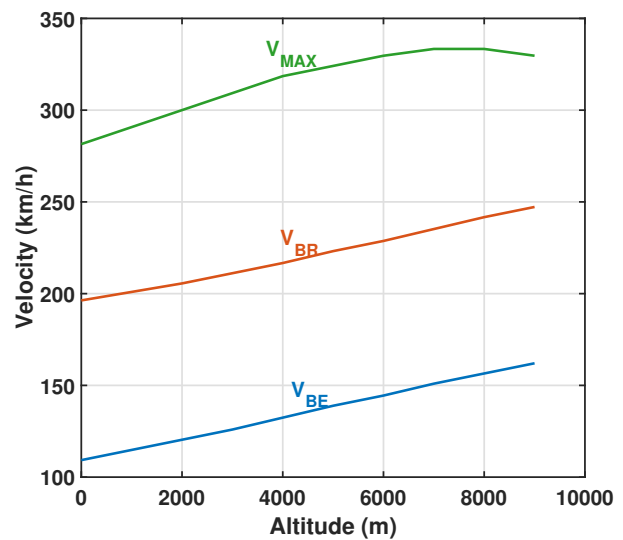


FIGURE 18.6: V_{BR} , V_{BE} , and V_{MAX} with altitude, ISA + 20°

Figure 18.7 shows the variation of maximum rate of climb with airspeed for different altitudes and ISA + 20° conditions. Rate of climb is determined by the excess power available at a given weight, flight speed, and altitude. The maximum rate of climb shown in Figure 18.7 therefore corresponds to the airspeed for minimum power or for best endurance speed, V_{BE} . Figure 18.8 shows the variation of maximum rate of climb plotted against altitude for different ambient temperatures. It is seen that with increase in altitude, the maximum rate of climb increases and later decreases for higher altitudes largely due to the variation of atmospheric density with altitude. Due to higher margin of transmission limit available at lower altitudes, a maximum inclined climb rate of around 14.3 m/s (2815 ft/min) is achieved for *Caladrius* at best endurance speed as shown in Figure 18.8.



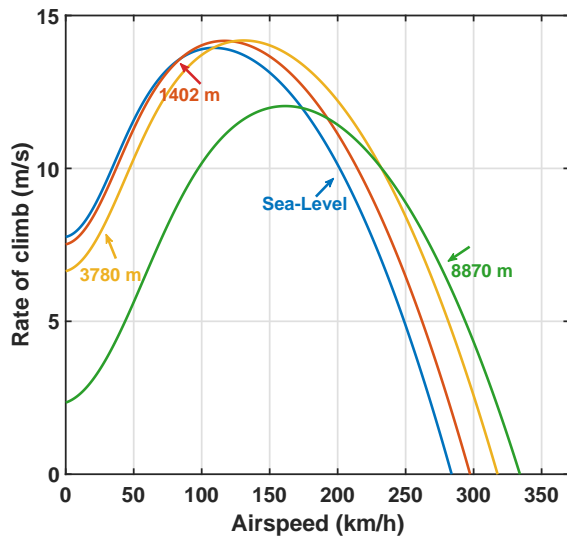


FIGURE 18.7: Rate of climb vs. airspeed for different altitudes, ISA + 20°

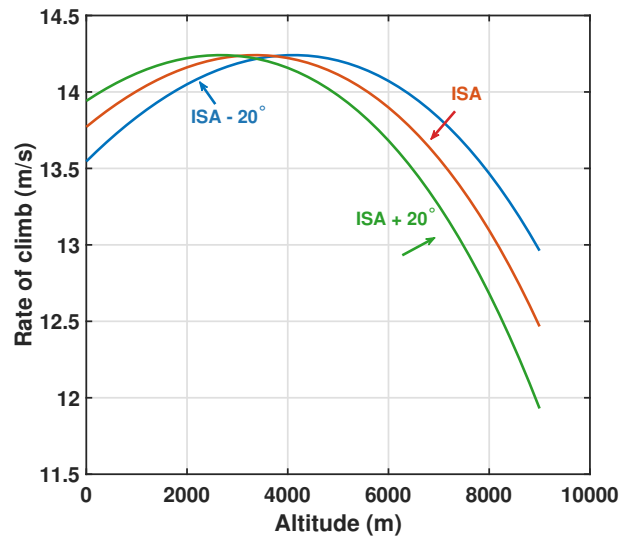
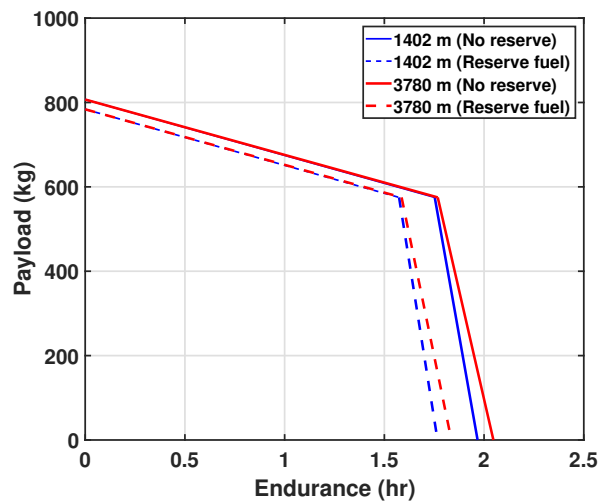
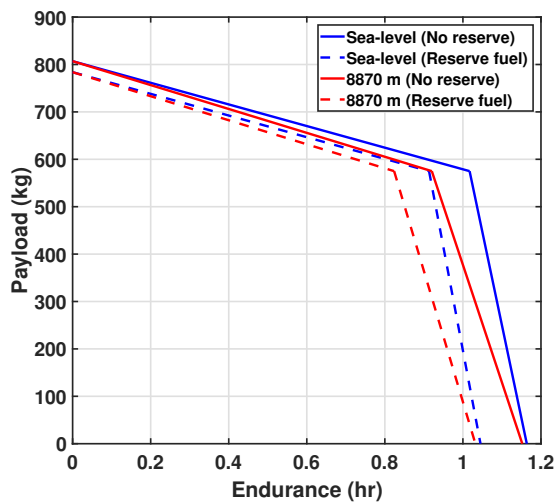


FIGURE 18.8: Maximum rate of climb vs. altitude

18.4 Range and Endurance

Payload-range and payload-endurance curves show the effects of vehicle range and endurance when trading off payload or fuel. Legs 1 and 3 of the mission primarily consist of cruise segments, while leg 2 consists of the hover segment at the high altitude. Based on the engine characteristics, the payload-range and payload-endurance diagrams were determined for hover and cruise segments.



(a) Payload vs. Endurance for hover at 3500 kg, ISA + 20° (b) Payload vs. Endurance for cruise at 3500 kg, ISA + 20°

FIGURE 18.9: Payload vs. Endurance at hover and cruise

The hover endurance for different payloads of *Caladrius* at both sea level and 8,870 m (29,100 ft) altitudes with and without 10% reserve fuel is shown in Figure 18.9(a). Because the vehicle is refuelled at the stopovers, the fuel tanks are sized based on the sizing leg, leg 2. A maximum hover endurance of slightly greater than one hour is achievable with *Caladrius*. With increase in altitude, the hover endurance decreases. However, this decrease is not significant because the

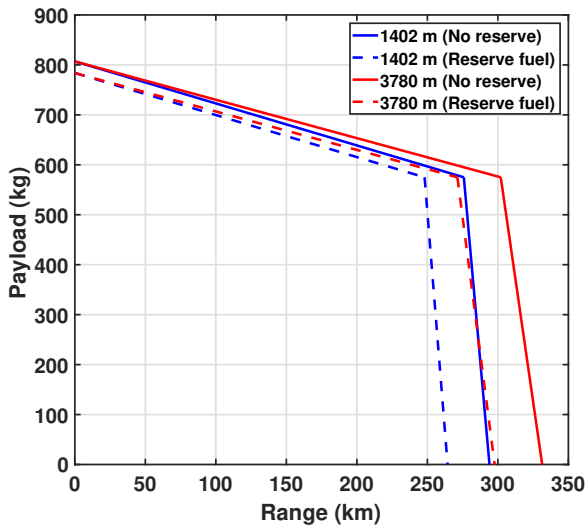


rotor is sized for high altitude; hence has in fact a lower Figure of Merit at lower altitudes. A similar payload-endurance figure for cruise segment is shown in Figure 18.9(b). A maximum cruise endurance of around 2 hours is achieved at an altitude of 3780 m (12,400 ft) for *Caladrius* with the corresponding best endurance speed. The maximum range of the aircraft is dependent on the best range speed, corresponding power, and fuel weight. Figure 18.10(a) shows the payload-range diagram for cruise segments of the mission at altitudes 1,402 m (4,600 ft) and 3,780 m (12,400 ft). A maximum cruise range of around 340 km (184 NM) is achievable with *Caladrius* at 3,780 m (12,400 ft), which is limited mainly due to small capacity of fuel tanks.

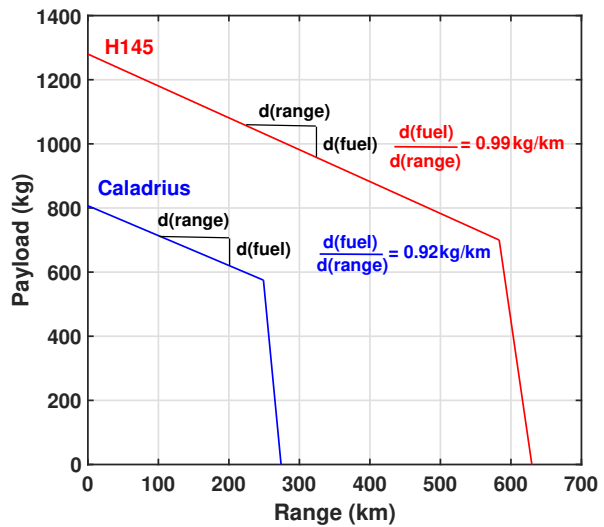
Figure 18.10(b) shows the payload-range diagram for *Caladrius* and Airbus H145 helicopter for a typical EMS mission [61]. This mission involves take-off at sea level, climb at best endurance speed to 1524 m (5000 ft), level cruise at best range speed, descent to sea level altitude and land at the destination. The slope of the curve shown in the figure represents the ratio of amount of fuel required to cover unit distance of range. This value is higher for H145; implying that a higher amount of fuel is required to cover the same amount of distance when compared to *Caladrius*, implying *Caladrius* is slightly more fuel efficient than H145. Equation 18.1 shows that inverse of the slope is proportional to lift to drag ratio of the vehicle when two vehicles of similar weight are compared.

$$L \frac{R}{W_F} = \frac{L \times V}{P \times SFC} \propto \frac{L}{D} \tag{18.1}$$

where, L is the Lift, R is Range, W_F is fuel capacity. Therefore, *Caladrius* appears to be more aerodynamically efficient than H145 by about 7%, but trades of endurance and range due to its lower fuel tank capacity.



(a) Payload vs. Range for cruise at 3500kg, ISA + 20°



(b) Payload vs. Range for H145 and Caladrius

FIGURE 18.10: Payload vs. Range diagrams

18.5 Rotor Capability

As mentioned earlier, *Caladrius* can lift a higher take-off weight than the design gross weight (3500 kg) obtained for the given mission based on the sizing leg. This is beneficial for performing missions at lower altitudes (< 8870 m). *Caladrius* can carry out different missions with a alternate design take-off weight of around 4500 kg at sea level (Figure 18.3(b)). Figure 18.11



shows the payload-range diagram for a typical cruise mission at sea level, ISA condition [61]. Since the capacity of fuel tanks is unchanged, the weight of fuel is kept same as earlier. The increase in take-off weight is represented by increase in the payload capacity. Therefore, *Caladrius* has a capability of carrying extra 1000 kg (2204 lb) of payload (possibly as external payload using the double hook system). This payload capacity is higher than that of H145. The range is however lower than H145 due to smaller fuel tanks.

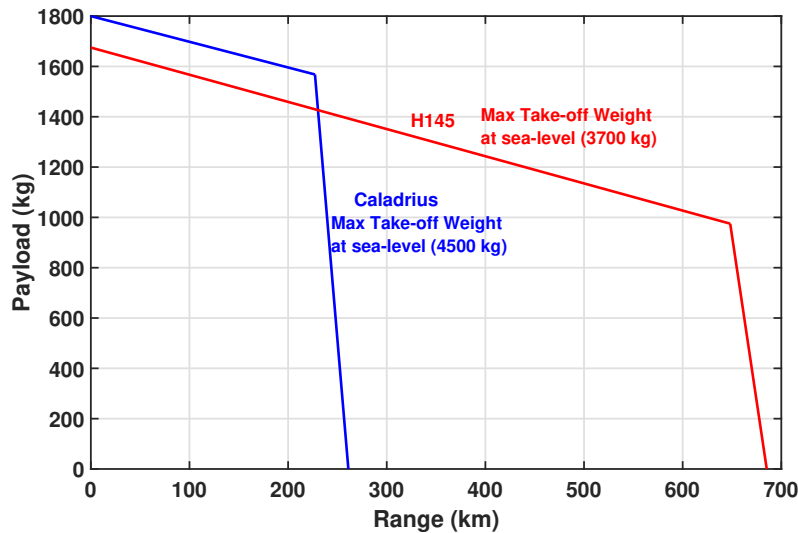


FIGURE 18.11: Payload vs. Range for H145 and Caladrius (4500 kg) at sea level, ISA

18.6 Autorotation Performance

All helicopters are required to demonstrate autorotation capability for certification. This depends upon several factors such as rotor disk loading, stored kinetic energy in the rotor system, and weight of the helicopter. This capability of a helicopter can be measured with the Autorotation Index (AI), which is a measure of its stored kinetic energy. Sikorsky AI, is defined as:

$$AI = \frac{I_R \Omega^2}{2WDL} \tag{18.2}$$

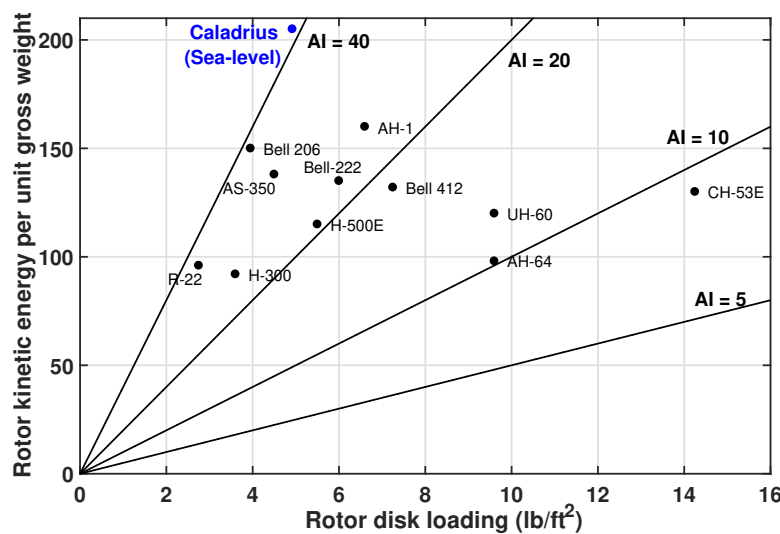


FIGURE 18.12: Comparison of autorotative index for various helicopters



where I_R is the flap moment of inertia of the rotor, Ω is the rotor speed, W is the weight of helicopter and DL is the disk loading. This index was used to compare the autorotational characteristics of *Caladrius* with existing helicopters. Figure 18.12 shows the autorotation indices of different helicopters [15]. It is seen that *Caladrius* has excellent autorotational capabilities with an AI of 41 at sea level. This high AI is a result of a large rotor and low downwash. Reference [15] provides the effect of altitude on the Autorotation Index,

$$AI = \frac{I_R \Omega^2}{2WDL} \frac{\rho}{\rho_0} \quad (18.3)$$

where, ρ and ρ_0 are the densities at the corresponding altitude and reference altitude (sea level). Even at the highest altitude, the AI of *Caladrius* is 15, which is more than many of the existing helicopters at sea level. Therefore, the rotors of *Caladrius* have sufficient kinetic energy for safe autorotation in the case of one engine failure. This brings extra safety for the critical mission of *Caladrius*.

TABLE 18.2: Performance summary and comparisons

Parameter	Units	Caladrius	H145	Bell 429
Design GTOW	kg	3500	3700	3400
	lb	7716	8158	7500
Payload (TOW: 4500kg, SL)	kg	1500	1000	1067
	lb	3311	2205	2353
Fuel Capacity	kg	232	723	822
	lb	512	1593	1813
Speed for Best Range (at High Altitude)	km/h	250	240	240
	knots	135	130	130
Speed for Best Endurance (at High Altitude)	km/h	160	130	111
	knots	87	70	60
Maximum Cruise Speed	km/h	315	259	280
	knots	170	140	151
Maximum Rate of Climb	m/s	14.3	7.62	14
	ft/min	2815	1500	2750
HOGE Ceiling (ISA + 0°)	m	9800	3825	2790
	ft	32152	12550	9150
Fuel Efficiency	kg/km	0.92	0.99	N/A
	lb/n.m	3.75	4.03	N/A
Maximum Range	km	360	651	761
	n.m	200	352	411
Maximum Endurance	hr	2 hr 10 min	3 hr 36 min	4 hr 30 min
Sound Pressure Level	dB	92	84.7	88.9
Autorotation Index	m ³ /kg	2.55	N/A	N/A
	ft ³ /lb	41		

Caladrius was explicitly designed for a search and rescue mission at the highest altitude on the Earth. It was designed to deliver excellent hover and cruise performance throughout the flight envelope. The performance analysis have shown that it has the highest hover ceiling



compared to the existing helicopters. In addition to hover performance, *Caladrius* offers excellent cruise performance and has a more efficient rotor (lower lift to drag ratio of the vehicle) than a comparable helicopter. Even though the design gross take-off weight for the mission is 3500 kg (7716 lb), *Caladrius* has the potential to hover or cruise with a higher take-off weight at lower altitudes. This is largely due to the availability of higher margin of transmission limit. The payload carrying (largely external) capacity of *Caladrius* was found to be superior than H145 at sea level, ISA conditions. It also has high rates of climb for a wide-range of altitudes.

Table 18.2 shows a comparison of different performance parameters of *Caladrius* with those of the Airbus H145 and Bell 429 helicopters [61]. H145 and Bell 429 are of the same weight class as of *Caladrius* and are popular choices for search and rescue missions conducted by Air Zermatt at Mattherhorn, Switzerland. As shown in the table, for most of the parameters, *Caladrius* has a better performance value than H145 and Bell 429.

19 Life-Cycle Cost Analysis

Caladrius's purchase, maintenance, and operating costs were calculated based on NDARC [13].

19.1 Purchase Price

The purchase price is estimated from a statistical relationship by Harris and Scully [62].

Purchase cost includes airframe cost, composite construction increment, mission equipment package (MEP), and flight control electronics (FCE). There are several factors for engine type, number of engines, landing gear, and number of rotors included. In addition, an overall technology factor is used. The model predicts purchase prices of 96% of 128 rotorcraft within 20%. One of the equations used is given below:

$$C_{AC} = \chi_{AF}(F_i c_{AF}) + C_{comp} + C_{MEP} + C_{FCE}$$

where C represents cost in dollars, χ is a technology factor and F_i accounts for the inflation.

Based on this model, *Caladrius*'s purchase price is **\$9,400,000** when $\chi = 1$ is used. As a comparison, the purchase price for Airbus EC145, which has a similar maximum take-off weight to *Caladrius* but much lower hover ceiling, is **\$9,700,000** [63].

19.2 Maintenance Cost

Maintenance cost includes labor, parts (airframe, engine, and avionics), engine overhaul, and major periodic maintenance costs. The equations are given by Harris [64] based on a 2011 civil database. The maintenance-man-hours per flight hour is estimated as:

$$M_{labor} W_E^{0.78}$$

where M_{labor} is a constant which is taken as 0.0017 for best practice. The maintenance cost per flight hour is calculated as follows:

$$C_{maint} = \chi F_i (c_{parts} + c_{engine} + c_{major}) + C_{labor}$$

Where C represents cost in dollars per hour, χ is a technology factor and F_i accounts for the



inflation. Based on these calculations, *Caladrius's* maintenance-man-hours per flight hour is **1.48** and the total maintenance cost per flight hour is **\$815/hr** when $\chi = 1$ is used.

19.3 Direct Operating Cost

Direct operating costs takes into account maintenance, fuel, crew, depreciation, insurance, and finance costs. The yearly operating cost is calculated as follows:

$$C_{OP} = T_F C_{maint} + C_{fuel} + C_{crew} + C_{dep} + C_{ins} + C_{fin}$$

Assuming *Caladrius* performs 30 missions per year, the operating cost is **\$505,930/yr**. Each mission costs about **\$16,864**.

Life-cycle cost is the sum of purchase and operating costs. Assuming *Caladrius* performs 30 missions per year over 20 years, it is calculated as **\$19,516,622**.

20 High Altitude Remarks

20.1 Vehicle Design

20.1.1 Sizing

The search and rescue mission for which *Caladrius* was designed has been successfully accomplished by many existing helicopters only at lower altitudes. The vital and challenging aspect of the mission is the extreme altitude. In order to understand the effect of high altitude on the mission, a vehicle was sized for a similar mission as given in RFP but at a lower altitude (maximum altitude 3048 m (10000 ft)). Table 20.1 shows the differences in the sizing parameters for the two vehicles. The effect of high altitude can be clearly seen from the differences in the size of the helicopter. A similar mission performed at lower altitudes results in a lower rotor diameter, lower GTOW and lower installed power.

TABLE 20.1: Comparison of vehicles for high and low altitude cases

Parameter	High Altitude Mission	Low-Altitude Mission
C_T/σ	0.12	0.12
N_b	5	3
AR	19	17
V_{tip}	231.6 m/s (760 ft/s)	204.2 m/s (670 ft/s)
Design GTOW	3500 kg (7716 lb)	2807 kg (6190 lb)
Rotor Diameter	13.76 m (45.14 ft)	12.20 m (40.02 ft)
Installed Power	2503 kW (3356 HP)	1167 kW (1565 HP)

20.1.2 Tail Rotor Design

Highly loaded tail rotor during high altitude rescue operation was optimized for low power and high cross winds. The key differences in blade geometric parameters compared to low altitude mission are large diameter and high solidity as shown in 20.2.



TABLE 20.2: Comparison of tail rotor design for high altitude and low altitude missions

Parameter	High Altitude Mission	Low-Altitude Mission
C_T/σ	0.10	0.10
Diameter	2.8 m (9.2 ft)	2.0 m (6.6 ft)
Number of blades	4	3
Solidity	0.239	0.171
Power in hover	65 kW (87 HP)	42 kW (56 HP)

To summarize, the main differences of the high altitude vehicle compared to low altitude one:

- Larger rotor diameter, greater installed power, and GTOW
- Higher power margin hence higher lifting capability at sea level
- Higher stall margin for main rotor
- Larger tail rotor and higher tail rotor solidity

20.2 Rotor Aerodynamics

Figure 20.1 shows the variation of Figure of Merit and hover power of *Caladrius's* rotor with altitude. Because the rotor is designed to be efficient at the peak of Mount Everest, its Figure of Merit drops with decrease in hover altitude. This is primarily because induced power in hover scales inversely with square root of density which means a decrease at lower altitudes, while profile power scales with density which means an increase. Because induced power is much higher than profile power in hover, the total power also decreases with decrease in hover altitude. Figure 20.2 shows the variation of aircraft L/D and power required for cruise at 296 km/h (160 knots). Due to lower profile and parasitic power at high altitude, the total required power for cruise is also lower.

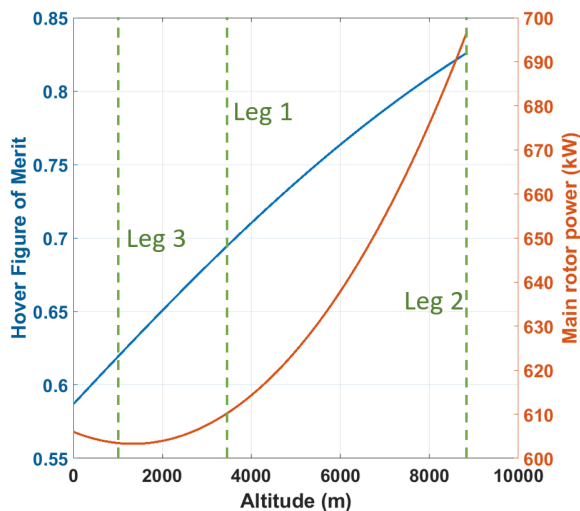


FIGURE 20.1: Hover power with altitude

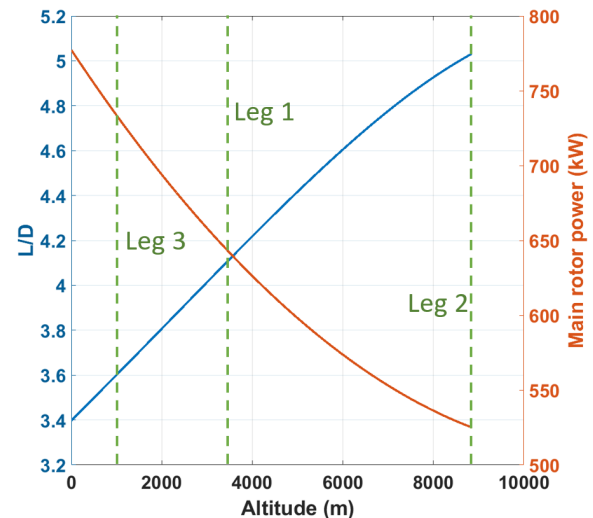


FIGURE 20.2: Cruise power with altitude

20.3 Cabin Pressurization

High altitude produces severe physiological detriments on human body, which are summarized below:



1. **Hypoxia:** Low partial pressure of oxygen (ppO_2) at high altitudes reduces consciousness time from about 15 minutes at 7620 m (25000 ft) to a few seconds at 12192 m (40000 ft).
2. **Decompression Sickness (DCS):** Tissues and fluids in human body contain dissolved nitrogen and other gases at sea level, which are released when the ambient pressure decreases at high altitude. Rapid decrease of pressure leads to bubbles of these gases being trapped in the body which may cause joint pain, neurological issues, swelling or itching of skin, and in severe cases death. Risk of DCS can be reduced by pre-breathing 100% oxygen 30 minutes before the flight and continuing it during the mission.
3. **Hypothermia:** Low temperatures at high altitudes can cause body to lose heat faster than it can produce, which severely impairs body functions and may cause death.

20.3.1 Solution Concepts

Pressurization at high altitude flights is not a requirement by FAA. However, as per FAR 91.211 “no person may operate a civil aircraft of U.S. registry at cabin pressure altitudes above 15,000 ft (MSL) unless each occupant of the aircraft is provided with supplemental oxygen”.

Hence, as a means of providing comfortable environment for crew, the following solution concepts were investigated for *Caladrius’s* operation at high altitudes:

1. Full cabin pressurization with an airlock system for high altitude operation
2. Cockpit only pressurization with an air-sealed wall separating the cockpit from the cabin
3. No pressurization

Vehicle sizing was carried out for these three concepts, and the results are summarized below:

	No Pressurization	Cockpit Only	Full Cabin Pressurization
GTOW	3428 kg (7558 lbs)	3533 kg (7833 lbs)	3663 kg (8075 lbs)
Power required	2462 kW (3302 HP)	2521 kW (3381 hp)	3065 kW (4111 hp)
Fuel mass	228 kg (503 lbs)	234 kg (516 lbs)	240 kg (529 lbs)

Compared with the baseline (no pressurization), full cabin pressurisation concept significantly increases the vehicle’s weight and power required during the mission. In addition, using an airlock unnecessarily adds complexity to the rescue mission. Cockpit only pressurisation is a good option as it provides the pilot a comfortable environment, so that he/she can completely focus on flying the vehicle, especially during rescue operation under high gust conditions of the mountain peak. However, based on the inputs from pilots Didier Delsalle and Samuel Summermatter, the rescue pilots and crews are trained for high altitude conditions and the extra weight, power consumption, complexity, and cost by cockpit pressurisation outweighs the benefit. Pressurisation as an optional feature would require 60kW when turned on. Since, our hover power loading is 5.036 kg/kW, this would mean 302.16 kg loss of



FIGURE 20.3: Mountain High EDS

payload, which basically means the mission cannot be completed. Hence *Caladrius* is not a pressurized helicopter. The occupants will be provided with oxygen tanks, full face masks and Electronic Pulse-Demand Oxygen Delivery System (EDS). EDS monitors the micro-pressures from inspiration efforts to deliver altitude calibrated pulses of oxygen. This conserves the oxygen usage at high altitudes and leads to lower tanks volume and weight. In addition, the crew of *Caladrius* are expected to wear insulation clothing and start using 100% pure oxygen at the end of leg 1 during refueling to combat decompression sickness.

21 Multi-Mission Capabilities

Caladrius is designed to have excellent hovering performance at extremely high altitudes with heavy gusts and an efficient high altitude cruise performance. The main features of the aircraft which makes it unique from existing helicopters of the same weight class are (i) extreme weather functionality [Ch 8], (ii) excellent high altitude performance [Ch 18], and (iii) heavy lifting capability, mainly external payload at lower altitudes [Ch 18]. In addition, a large modular cabin (like the presence of seat tracks) makes *Caladrius* well suited for a variety of missions. These missions are categorized into extreme search and rescue, heavy lifting, transportation and other unique missions. Each of these missions described in this section illustrate *Caladrius's* versatility.

21.1 Disaster Relief in Severe Weather

Natural disasters like tsunamis, earthquakes and avalanches result in a loss of many lives. With focused air support and transportation, these casualties can be kept from increasing over time. The earthquakes in Sichuan (2008) and Nepal (2015) and the floods in Kerala (2018) claimed the lives of over a hundred thousand people and uprooted the lives of millions. Since *Caladrius* is designed to withstand high gusts with a low downwash, it can be used to rescue people from extreme weather disaster affected areas. Due to its capability to carry higher payload, it can also be used to supply food and other necessities to remote areas. All the non-mission specific components like the turret camera, external hoist, EMS equipment etc. are removed from the aircraft. Figure 21.1 shows a typical mission profile with *Caladrius* used to supply necessities (payload) of around 770 kg to the remote areas. It can also be used to transport stranded people (up to 10 in a high dense cabin layout) to a safe location.

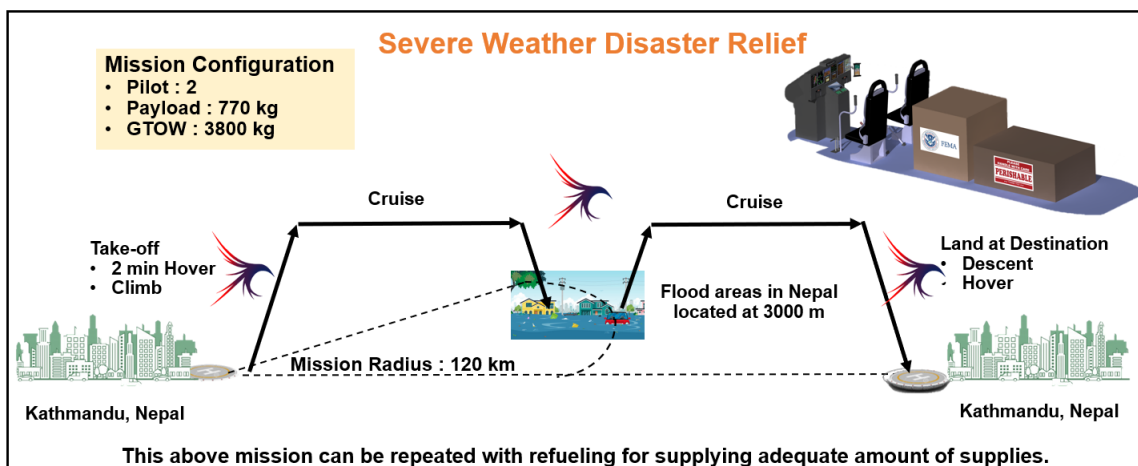


FIGURE 21.1: Mission profile for disaster relief missions

Multi - Mission Capabilities



Firefighting



Arctic Monitoring and Rescue



Offshore Transport



High Altitude Surveillance



Extreme Altitude Mountain Rescue



High Altitude EMS



Severe Weather Disaster Relief

21.2 Aerial Fire-fighting

A typical fire-fighting mission involves a back and forth cruise segments to the reservoir and the fire locations and then back to the starting point. A flexible bambi bucket can be suspended on a cable carried by *Caladrius* to deliver water for fire-fighting. This bucket can be filled on the ground or water can be siphoned from lakes, rivers etc.

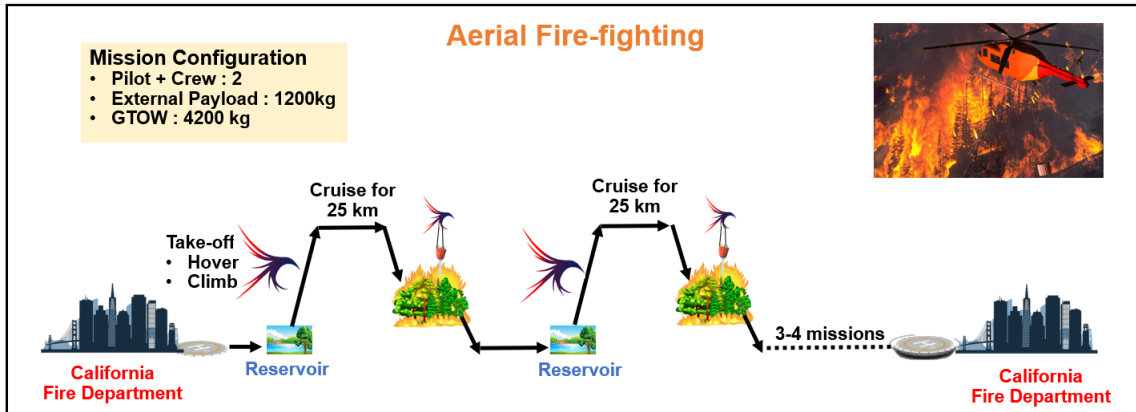


FIGURE 21.2: Mission profile for fire-fighting missions

All the non-mission specific equipments like cameras, hoist, stretchers etc. are excluded from the aircraft. The bambi attachments and the performance characteristics of *Caladrius* for a typical fire-fighting mission is shown in Figure 21.2. It is seen that *Caladrius* can be used to supply 1200 litres of water for 4 times before it runs out of fuel.

21.3 Rapid Air Medical Transport

Caladrius can be used for rapid air medical transportation especially in windy, high altitude locations. The typical EMS missions include fire accidents, swift medical response providing out-of-hospital treatment, etc. *Caladrius* can be an ideal choice for EMS at high altitude places like Peru and also at places which experience heavy winds like Scotland, Ireland etc. For this mission, heavy equipment such as the external hoist is removed to provide room for advanced emergency medical supplies and equipment. The interior layout is very similar to that for the high altitude rescue mission.

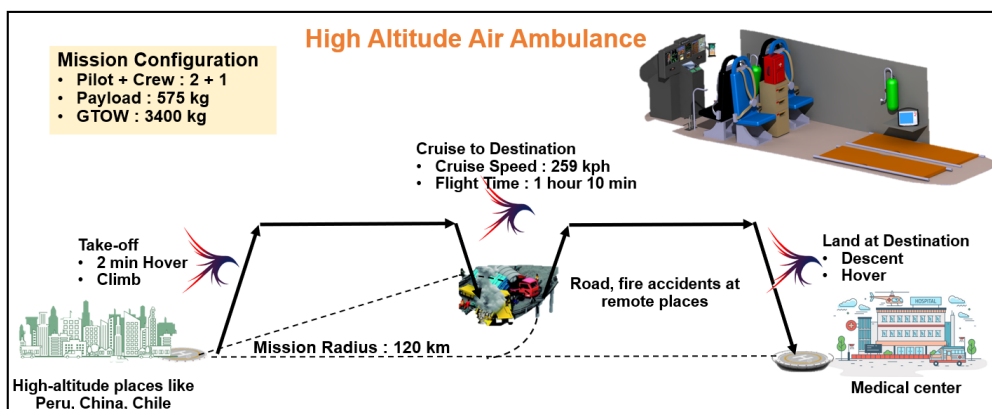


FIGURE 21.3: Mission profile for medical transportation at high altitude locations



Caladrius can also be a great choice for rescuing people from a building rooftop involved in a fire accident. Top of a burning building will have very unpredictable winds due to the rising heat and *Caladrius* has good gust rejection with low downwash. Figure 21.3 shows a typical mission profile for this type of mission. It is seen that *Caladrius* has a low radius of action, however, a higher cruise speed at high altitude locations still leverages *Caladrius's* capabilities.

21.4 Off-shore Oil-rigs and Wind Farms

Caladrius can be used to transport up to 6 passengers with a range of 250 km and is well-suited for offshore transportation. Since it is designed for a low pilot workload, it is an ideal choice for transportation from and to deep sea oil-rigs located in North Sea which experience winds up to 20-30 knots. The cabin layout for this mission is shown in Figure 21.4 with all the irrelevant components removed and passenger transportation furnishings added. *Caladrius* can be adopted for support flights to off-shore wind farms located in the coasts of Western Australia which are warmer but windy and also experience inclement weather conditions.

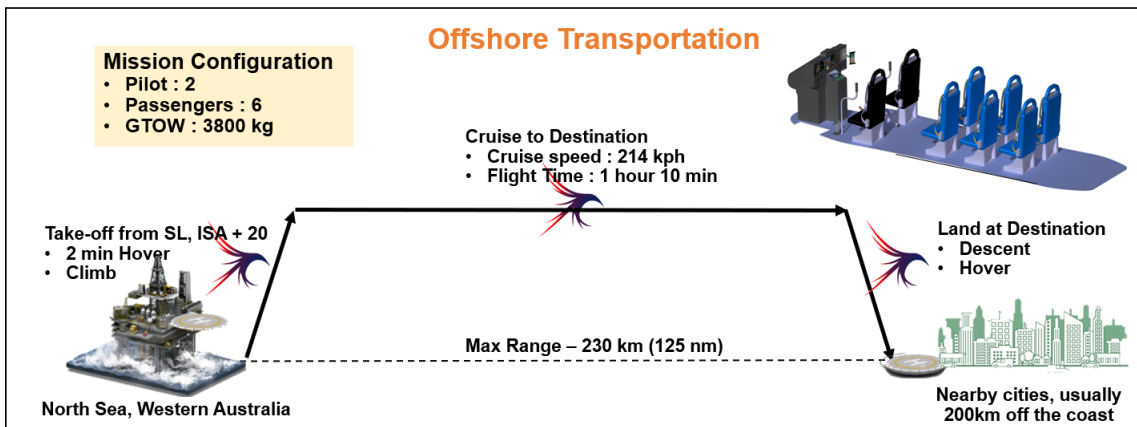


FIGURE 21.4: Mission profile for off-shore transportation

21.5 Maritime High-Seas Rescue

Caladrius can be used to carry out off-shore rescue missions. Since it is designed for extreme winds, it will be an ideal choice for these missions which experience high winds.

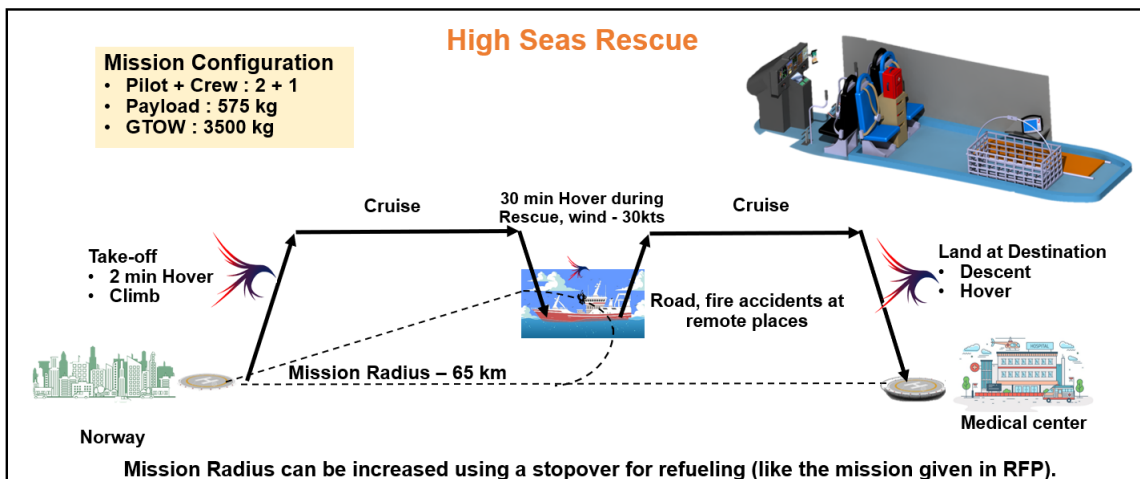


FIGURE 21.5: Mission profile for high-seas rescue



Most of the cabin layout and crew composition will remain the same as used for the standard high altitude rescue mission. Some additional components like the sea tray are added to the cabin to prevent water from seeping onto the helicopter cabin floor. The installation is designed specifically to meet the needs of SAR operators to avoid sea water contamination during hoisting operations. A typical high-seas rescue mission profile is shown in Figure 21.5. Since *Caladrius* has a lower fuel capacity, the radius of action is on the lower side. This can be increased either by refueling at intermediate stations or by increasing the fuel tank capacity.

21.6 Geophysical Surveys and High Altitude Surveillance

Climate change has exposed the once impossible sea route - the Northwest Passage - connecting Atlantic and Pacific through the Canadian archipelago. Extensive research is done to study the climate around arctic channels. Radars will be attached underneath the helicopter to record any changes to the glaciers. The weather conditions in these areas are no less than that of Mount Everest, thereby making it a challenging mission. Because *Caladrius* excels in cold and windy conditions, arctic surveys and mountain range surveys would be perfect missions for the helicopter.

Because *Caladrius* provides a good high altitude performance, it can be used for military reconnaissance. A typical mission like this involves the aircraft flying at low speeds at high altitudes around a region to capture pictures of the area using advanced cameras.

22 Summary

The University of Maryland Graduate Design Team designed *Caladrius* to meet all of the vehicle and operational requirements specified in the Request for Proposal for an Extreme Altitude Mountain Rescue Vehicle for the 2019 VFS Design Competition. *Caladrius* is a single main rotor helicopter that is not only designed for extreme altitude hover, but also high cruise speed to reach the rescuees expeditiously and bring them back to safety. Insights obtained from direct interaction with many pilots including Didier Delsalle and Samuel Summermatter were carefully incorporated into every aspect of the design that resulted in a “Pilot’s Helicopter”. The rotors were specifically designed for this demanding mission that no other rotorcraft today is capable of performing. The five-bladed bearingless main rotor consists of bilinear twist, planform taper, swept and anhedral tips, and achieves a high Figure of Merit and high lift to drag ratio for the aircraft. The four-bladed bearingless tail rotor with highly twisted blades allows for high cross-wind and stable anti-torque. High safety and low pilot workload were principal design objectives, which resulted in a twin engine design, light weight drive system with 50 minute dry running capability, an advanced flight control system, advanced avionics package, search and rescue equipment specifically chosen for the mission, and rotors with high gust tolerance from any direction including the updrafts and downdrafts observed at Mount Everest. A bearingless hub with a flap frequency of 1.06/rev achieves the balance between high control authority and high gust tolerance. A model following architecture used in the flight control system design ensures both high gust tolerance and high control power. High field of view for pilots were achieved with bubble windows and side windows. This efficient and capable rotorcraft design would enable rescue missions to world’s highest peak that were not possible before.



Bibliography

- [1] The Editors of Encyclopaedia Britannica, “Extreme Sports,” <https://www.britannica.com/sports/extreme-sports>, Online; accessed on 12 May 2019.
- [2] Arnette, A., *Everest by the Numbers: 2019 Edition*, 2019.
- [3] Sharma, B. and Ramzy, A., “Three More Die on Mount Everest During Crowded Climbing Season,” *The New York Times*, May 2019.
- [4] Airbus Helicopters’, *Landing on Everest: Didier Delsalle Recalls his Record Flight*, November 2, 2017.
- [5] Swopes, B. R., “21 June 1972,” <https://www.thisdayinaviation.com/21-june-1972/>, June 2018, Online; accessed on 10 February 2019.
- [6] Wikipedia contributors, “Mount Everest,” 2019.
- [7] Wikipedia contributors, “Golden Hour (medicine),” 2019.
- [8] Saaty, R., “The Analytic Hierarchy Process—What It is and How It is Used,” *Mathematical Modelling*, Vol. 9, No. 3 - 5, 1987, pp. 161 – 176.
- [9] Pugh, S., *Total Design: Integrated Methods for Successful Product Engineering*, Engineering technology and design, Addison-Wesley Publishing Company, 1991.
- [10] Preston, J. R. and Ferguson, S. W., “Rotorwash Operational Footprint Modeling,” *40th European Rotorcraft Forum*, September 2014.
- [11] Hrishikeshavan, V., *Experimental Investigation of a Shrouded Rotor Micro Air Vehicle in Hover and in Edgewise Gusts*, Ph.D. thesis, University of Maryland, 2011.
- [12] Bregger, R. E. and Dawson, S., “Side-by-Side Hover Performance Comparison of MDHC 500 NOTAR and Tail Rotor Anti-Torque Systems,” *48th American Helicopter Society Forum*, June 1992.
- [13] Johnson, W., “NDARC NASA Design and Analysis of Rotorcraft,” Tech. Rep. 2009-215402, NASA, December 2009.
- [14] Green, S., *Death Rate of Mount Everest Climbers*, 2018 (updated January 2, 2018).
- [15] Leishman, G. J., *Principles of Helicopter Aerodynamics*, Cambridge University Press, 2006.
- [16] Srinivasan, G. R. and Baeder, J. D., “TURNS: A Free-Wake Euler/Navier-Stokes Numerical Method for Helicopter Rotors.” *AIAA Journal*, Vol. 31, No. 5, 1993, pp. 959–962.
- [17] Medida, S. and Baeder, J. D., “Application of the Correlation-based Gamma-Re Theta t Transition Model to the Spalart-Allmaras Turbulence Model,” 20th AIAA Computational Fluid Dynamics Conference, June.
- [18] Johnson, W., *Rotorcraft Aeromechanics*, Cambridge University Press, 2013.



- [19] Desopper, A., Lafon, P., Philippe, J. J., and Prieur, J., “Effect of an Anhedral Sweptback Tip on the Performance of a Helicopter Rotor.” 13th European Rotorcraft Forum, 1987.
- [20] Brocklehurst, A. and Barakos, G. N., “A Review of Helicopter Rotor Blade Tip Shapes.” *Progress in Aerospace Sciences*, Vol. 56, 2013, pp. 35–74.
- [21] Jude, D., Sitaraman, J., Lakshminaraya, V. K., and Baeder, J. D., “An Overset Generalized Minimal Residual Method for CFD on Heterogeneous Compute Architectures.” AIAA Scitech 2019 Forum, January 2019.
- [22] Mishra, A., Jude, D., and Baeder, J. D., “ADGAR: A GPU Accelerated Adjoint Solver for Shape Optimization in Viscous Flows,” AIAA Scitech 2019 Forum, January 2019.
- [23] Walsh, J. L., “Performance Optimization of Helicopter Rotor Blades,” Tech. Rep. TM 1991-104054, April 1991.
- [24] Huber, H., “Will Rotor Hubs Lose Their Bearings? A Survey of Bearingless Main Rotor Development,” *Proceedings of the European Rotorcraft Forum, Avignon, France*, September 1992.
- [25] Falls, J., *Design and Performance Prediction of Swashplateless Helicopter Rotors with Trailing Edge Flaps and Tabs*, Ph.D. thesis, University of Maryland, College Park, University of Maryland Libraries, 2010.
- [26] Thomas, W., Hong, S., Yu, C.-J., and Rosenzweig, E. L., “Enhanced Erosion Protection for Rotor Blades,” *Proceedings of AHS 2009*, May 2009.
- [27] National Transport Safety Board, “Loss of Tail Rotor Effectiveness in Helicopters,” https://www.nts.gov/safety/safety-alerts/Documents/SA_062.pdf, March 2017.
- [28] Prouty, R. W., *Military Helicopter Design Technology*, Krieger Publishing Company, Malabar, Florida, 1998.
- [29] Young, J. E., *Helicopter Vertical Stabilizer Design Considerations*, Master’s thesis, Naval Postgraduate School, Monterey, California, June 1983.
- [30] Kim, D.-K. and Kim, S., “The Overview of KARI Bearingless Main Rotor Hub System,” *40th European Rotorcraft Forum*, 2014.
- [31] Prouty, R. W., *Helicopter Performance, Stability, and Control*, Krieger Publishing Company, Malabar, Florida, 1986.
- [32] Guo, C. G. and Xu, G. H., “Selected Aerodynamic Design Issues for the Single-Rotor Remotely Piloted Helicopter,” *Aircraft Engineering and Aerospace Technology*, Vol. 72, No. 3, 2000, pp. 241–246.
- [33] Horn, J. F. and Bridges, D. O., “A Model Following Controller Optimized for Gust Rejection During Shipboard Operations,” *63rd Annual Forum of American Helicopter Society*, May 2007.
- [34] Tischler, M. B., “Introduction to Autogyros, Helicopters, and Other V/STOL Aircraft,” Tech. Rep. AD-A182 197, National Aeronautics and Space Administration, 1987.



- [35] Frost, C. R. and Dryfoos, J. B., “Design and Testing of Flight Control Laws on the RASCAL Research Helicopter,” *AIAA Modeling and Simulation Technologies Conference and Exhibit*, August 2002.
- [36] AVSCOM, “Aeronautical Design Standard Performance Specification Handling Qualities Requirements for Military Rotorcraft (ADS-33E),” March 2000.
- [37] Lebacqz, J. V., “Survey of Helicopter Control/Display Investigations for Instrument Decelerating Approach,” Tech. Rep. NASA-TM-78565, National Aeronautics and Space Administration, 1979.
- [38] Department of Defense, USA, “Flying Qualities of Piloted Aircraft,” June 1995.
- [39] “Certification Specifications and Acceptable Means of Compliance for Large Rotorcraft (CS-29) - Amendment 6,” December 2018.
- [40] Sibilski, K., “A Study of the Flight Dynamics Helicopter Carrying an External Load Using Bifurcation Theory and Continuation Methods,” *Journal of Theoretical and Applied Mechanics*, Vol. 41, No. 4, 2003, pp. 823–852.
- [41] Sridharan, A., Celi, R., and Chopra, I., “On the Role of Aerodynamic Non-Linearities in Helicopter Sling Load Operations,” *67th Annual Forum of American Helicopter Society*, May 2011.
- [42] Bisgaard, M., la Cour-Harbo, A., and Bendtsen, J. D., “Adaptive Control System for Autonomous Helicopter Slung Load Operations,” *Control Engineering Practice*, Vol. 18, No. 7, 2010, pp. 800–811.
- [43] Nagaraj, V. T. and Chopra, I., “Preliminary Design of Rotorcraft,” .
- [44] ANSI/AGMA & 937-A12, “AGMA Information Sheet Aerospace Bevel Gears,” Tech. rep., AGMA, Alexandria, Virginia, Oct. 2012.
- [45] ANSI/AGMA & 2001-D04, “Fundamental Rating Factors and Calculation Methods for Involute Spur and Helical Gear Teeth,” Tech. rep., AGMA, Alexandria, Virginia, Dec. 2004.
- [46] Kern, C. P., Wright, J. A., Sebastian, J. T., Grabowski, J. L., Jordan, D. F., and Jones, T. M., “Manufacturing and Processing of a New Class of Vacuum-Carburized Gear Steels with Very High Hardenability,” Tech. rep., AGMA, Alexandria, Virginia, Oct. 2011.
- [47] Rameshkumar, M., Venkatesan, G., and Sivakumar, P., “Finite Element Analysis of High Contact Ratio Gear,” Tech. rep., AGMA, Alexandria, Virginia, Oct. 2010.
- [48] Gasparini, G., Motta, N., Gabrielli, A., and Colombo, D., “Gearbox Loss of Lubrication Performance: Myth, Art or Science?” *Proceedings of the 40th European Rotorcraft Forum, Amsterdam, Netherlands*, September 2014.
- [49] Hartmann, J. and Jonda, W., “Helicopter Manufacturers’ Requirements for Lubricating Oils,” *Journal of Synthetic Lubrication*, Vol. 4, No. 1, 1987, pp. 41–51.
- [50] Loewenthal, S. H., “Design of Power Transmitting Shafts,” Tech. rep., NASA, Lewis Research Center, Cleveland, Ohio, July 1984.



- [51] Sebastian, J. T., Wright, J. A., Kern, C. P., Kooy, R. J., and Hamann, E. W., “Advanced High Performance Ferrium® Steels for Lighter More Robust Rotorcraft,” *Proceedings of the 38th European Rotorcraft Forum, Amsterdam, Netherlands*, September 2012.
- [52] Willis, E. A. and Wintucky, W. T., “An Overview of NASA Intermittent Combustion Engine Research,” *20th Joint Propulsion Conference*, June 11-13, 1984.
- [53] Pratt & Whitney Canada, “PT6C Specs,” <https://www.pwc.ca/en/products-and-services/products/helicopter-engines/pt6c>, Online; accessed on 13 May 2019.
- [54] Varga, B., “Power Sources of Military Helicopters,” *Academic and Applied Research in Military Science*, Vol. 17, 2018, pp. 139–168.
- [55] Fink, A., “A Helicopter With a Fuselage and a Composite Tail Boom,” 01 2018.
- [56] Chernoff, M., “Analysis and Design of Skid Gears for Level Landing,” *Journal of the American Helicopter Society*, Vol. 7, No. 1, 1962, pp. 33–39.
- [57] Hiemenz, G. J., *Semi-Active Magnetorheological Seat Suspensions for Enhanced Crashworthiness and Vibration Isolation of Rotorcraft Seats*, Ph.D. thesis, University of Maryland, 2007.
- [58] Meggitt SA, “MEGGITT Vibro-Meter® Health and Usage Monitoring (HUMS),” <https://meggittsensing.com/aerospace/product/helicopter-hums-to-prevent-failures-increase-safety-and-reduce-costs/>, Online; accessed on 28 May 2019.
- [59] Ffowcs Williams, J. E., Hawkings, D. L., and James, L. M., “Sound Generation by Turbulence and Surfaces in Arbitrary Motion.” *Philosophical Transactions of the Royal Society of London. Series A, Mathematical and Physical Sciences*, Vol. 264, No. 1151, 1969, pp. 321–342.
- [60] Farassat, F., “Linear Acoustic Formulas for Calculation of Rotating Blade Noise.” *AIAA Journal*, Vol. 19, No. 9, 1981, pp. 1122–1130.
- [61] Airbus Helicopters, “H145 Technical Data,” 2018.
- [62] Harris, F. D. and Scully, M. P., “Rotorcraft Cost Too Much,” *Journal of the American Helicopter Society*, Vol. 43, No. 1, January 1998.
- [63] Traveler, B. J., “Airbus Helicopters H145,” <https://www.bjtonline.com/aircraft/airbus-helicopters-h145>, Online; accessed on 29 May 2019.
- [64] Harris, F. D., “Introduction to Autogyros, Helicopters, and Other V/STOL Aircraft,” Tech. Rep. NASA SP 2011-215959, National Aeronautics and Space Administration, 2012.

